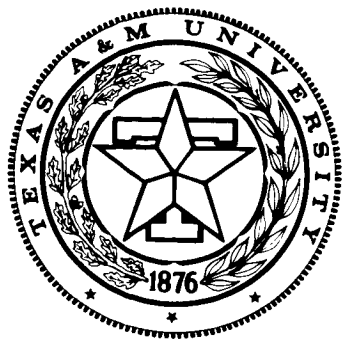

Mechanics and Materials Center
TEXAS A&M UNIVERSITY
College Station, Texas

Annual Progress Report
(April, 1986 - August, 1987)

for

NASA Research Grant NAG-1-659

entitled

MICROMECHANICS OF COMPRESSION FAILURES IN OPEN HOLE COMPOSITE LAMINATES

prepared by

E. Gail Guynn
Walter L. Bradley
Department of Mechanical Engineering
Texas A&M University
College Station, TX 77843
(409) 845-1259

September, 1987

Contract Monitor: John Whitcomb
Nasa Langley

MICROMECHANICS OF COMPRESSION FAILURES IN OPEN HOLE COMPOSITE LAMINATES

A Report

by

E. GAIL GUYNN

WALTER L. BRADLEY

TABLE OF CONTENTS

TABLE OF CONTENTS (Continued)

LIST OF TABLES

LIST OF FIGURES

NOMENCLATURE

a	Dugdale crack half length, cm
a_o	Whitney-Nuismer Average Stress Criterion characteristic distance, cm
b_k	Dimensions for partially loaded crack, cm, $k = 1, 2$
c	Half crack length, cm
DCB	Double Cantilever Beam
d	Half crack length plus compressive plastic zone width, cm
d_o	Whitney-Nuismer Point Stress Criterion characteristic distance, cm
E_k	Young's modulus: $k = 1, 2$ for lamina properties; $k = x, y$ for laminate properties; $k = cy$ for measured compression modulus
F_h^s	Boundary-correction factor for a circular hole subjected to remote uniform stress
F_h^σ	Boundary-correction factor for a circular hole in an infinite plate, partially loaded crack
F_w^s	Boundary-correction factor for two symmetric cracks emanating from a circular hole in a finite-width plate subjected to a uniform stress
F_w^σ	Boundary-correction factor for two symmetric cracks emanating from a circular hole in a finite width plate subjected to partial loading
G_c^*	Aronsson-Bäcklund apparent fracture energy, kJ/m^2
G_k	Shear modulus: $k = 12$ for lamina properties; $k = xy$ for laminate properties
G_{Ic}	Mode I critical strain energy release rate, J/m^2
K	Stress intensity factor, Pa-$\sqrt{\text{m}}$
L	Across the width sectioning specimen

L1,L2	Designation for longitudinal strain gages located just above the shear crippling zone
MTS	Material Test System
NDE	Nondestructive Examination
P	Dugdale wedge force per unit plate thickness, N/m
p	Internal tensile stress distributed over Dugdale crack, Pa
R	Through the thickness sectioning specimen
r	Hole radius, cm
S	Remotely applied compressive stress, MPa
SCF	Stress Concentration Factor
SEM	Scanning Electron Microscope
T1,T2	Designation for transverse strain gages located just above the shear crippling zone.
t	Specimen thickness, mm
v	Crack opening displacement, mm
w	Specimen half width, cm
X, Y, Z	Orthogonal reference coordinates
x	Integration variable in Dugdale analysis, cm
x_k	Section dimension for Y-Z plane, mm
z_k	Section dimension for X-Y plane, mm
α	Constraint factor in Newman's analysis: α=1 for plane stress; α=3 for plane strain
ϵ	Applied strain
ρ	Length of plastic zone ahead of crack tip in metals, or length of compressive crush zone in composites, cm

σ Applied tensile stress in Dugdale analysis, MPa

σ_o Unnotched tensile strength, Pa

σ_{oc} Compressive stress supported in crush zone, Pa

σ_{ot} Constant tensile flow stress in Dugdale plastic zone, Pa

σ_{ys} Material yield strength, Pa

ν_k Poisson's ratio: $k = 12$ for lamina properties; $k = xy$ for laminate properties; $k = cxy$ for compression loading

CHAPTER I

INTRODUCTION

The high strength-to-weight ratio of composite materials is ideally suited for aerospace applications where they already are used in commercial and military aircraft secondary structures and will soon be used for heavily loaded primary structures. One area impeding the widespread application of composites is their inherent weakness in compressive strength when compared to the tensile properties of the same material. Furthermore, these airframe designs typically contain many bolted or riveted joints, as well as electrical and hydraulic control lines. These applications produce areas of stress concentration, and thus, further complicate the compression failure problem. This investigation addresses open hole compression failures which represent a typical failure mode for composite materials.

Compression failures in composite laminates containing circular holes are often preceded by the development of a damage zone which grows with increasing compressive load. This damage zone, which appears similar to a flat, tension fatigue crack in metals, initiates at the edges of the hole and propagates across the width of the laminates leading to final failure. The damage zone, also referred to as the crush zone throughout this thesis, is initiated by local fiber buckling and/or shear crippling in the edges of the hole. The length or size of the crush zone increases with increasing compressive load, and then it propatates until the shear crippling zone completely traverses the specimen. Immediately, a catastrophic failure follows giving brooming and/or delamination. Figure 1 (from preliminary testing at NASA Langley Research Center with Dr. Wolf Elber) shows the initiation and propagation of this damage zone across the specimen width. However, this type of damage has been observed

Fig. 1 Initiation and propagation of damage zone prior to compressive failure in an AS4/PEEK specimen. Hole diameter is 0.16 cm. Damage zone lengths are
a) 0.05cm.
b) 0.08 cm.
c) 0.13 cm and 0.30 cm.
d) 0.36 cm and 0.36 cm.

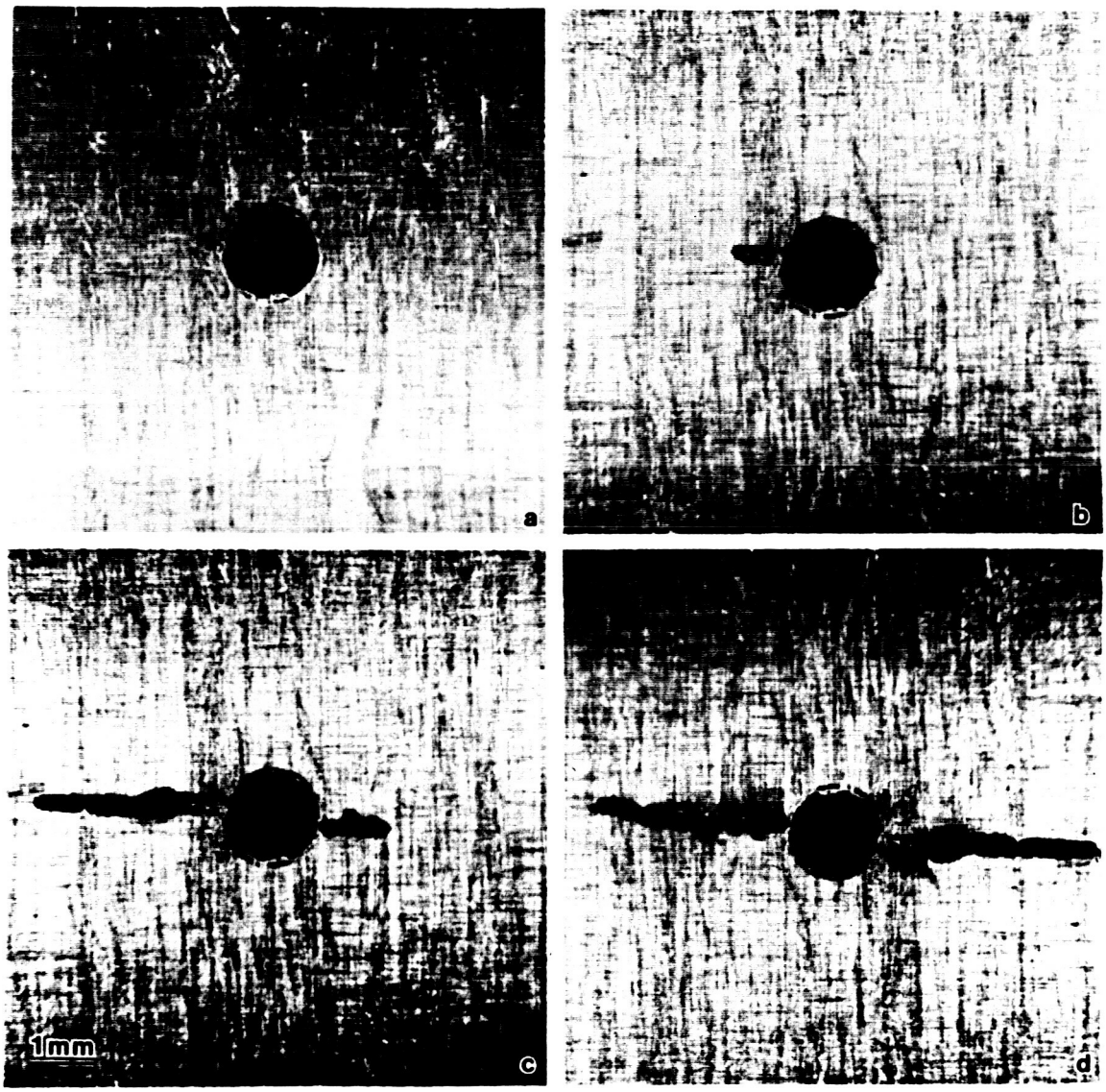

only in composite laminates composed of ductile resin systems. It was observed by Guynn and Elber during this preliminary investigation that stable growth of the shear crippling zone in brittle systems is very short and cannot be visually detected prior to catastrophic failure. It may be that failure in such systems is initiation rather than propagation controlled, meaning that failure occurs immediately upon initiation of a local shear crippled or fiber buckled region adjacent to the hole. Although many researchers have studied the compressive failure modes, the details of damage progression and development prior to failure still remain unclear.

Review of Literature

Compression Investigations

The mechanisms of longitudinal compressive failure in unidirectional fiber reinforced composites have been the subject of study for more than two decades. Early theoretical treatments were based on the hypothesis that failure resulted from fiber instability within an essentially elastic matrix.[1-4] However, agreement between theoretical predictions based on fiber instability and experimental results were poor. An important alternative mechanism was suggested in 1974 by Ewins and Ham.[5] They suggested that fiber strength in compression in many systems would precipitate compressive failure at stress levels much lower than those predicted for fiber instability. These failures typically are described as a response to the shear stress acting across both fibers and matrix on the plane of maximum shear stress. Ewins and Potter[6] showed the differences between the shear and fiber instability failure modes and discussed the structural design implications. Additionally, a third type of compressive failure in unidirectional or multiaxial lay-up composites is associated with a combination of fiber buckling and kinking called shear crippling.

Macroscopically, shear crippling looks like a shear failure on a plane at an angle to the direction of loading. However, microscopic inspection reveals the formation of a kink band.

Open hole and post-impact compressive strengths of composite laminates have been the subject of numerous investigations.[7–16] Byers[7] reported moiré fringe contours indicating that surface delamination can precede specimen failure, and he recorded large transverse (through the thickness) tensile strains on the inside surface of the hole. Furthermore, his experiments indicate that strength reduction in circular hole specimens is not directly related to net area reduction, and that these specimens of various material systems have different failure modes. Mikulas[12] has shown that limiting values for failure may be bounded by simple criteria based on notch sensitivity. If the material is notch insensitive the failure strains are directly proportional to the reduction in cross-sectional area (shown not to be the case in Ref. 7), while if the material is notch sensitive then it is postulated that the material fails when the strain concentration at the hole edge equals the failure strain of the material. However, these failure criteria provide only the upper bound for the data; the latter assumption is nonconservative. This situation indicates the possibility that the strain concentration effect alone cannot possibly account for the failure process, and a localized failure mechanism may be present. Based on this premise, Starnes et al[9] completed a detailed investigation on the open hole strength of strength-critical composite laminates, and they reported a shear crippling type of failure to be prevalent in the vicinity of the hole prior to catastrophic failure. This conclusion was based on post-mortem examination of damaged specimens. Two investigations[15,16] which also consider environmental effects are important to this review because they too have reported a shear crippling type failure adjacent to

the hole prior to catastrophic failure. Potter[15] observed the important contribution on the in-plane shear stresses that lead to instability in the 0° (parallel to the compressive load direction) fibers. He also reported that delamination does not play a significant role in the final fracture process, and it probably occurs after the collapse of the load-bearing 0° plies.

Apparently, the compressive failure mode observed depends strongly on the lateral support provided to the fiber during loading. In the absence of strong lateral support, all fibers would fail by buckling. However, as matrix stiffness increases, buckling is suppressed and the fibers then fail in shear. Zero degree plies surrounded by ±45° plies also seem to be more resistant to fiber microbuckling, probably due to the transverse support provided by such plies which are themselves not likely to give fiber buckling. The available data in the literature strongly suggest that shear crippling involving fiber kinking is the most common failure mode in composite laminates for strength-critical applications.[9,13–16] These failures initiate with the kinking of a few fibers; these kinked fibers in turn unstabilize adjacent fibers so that these also fail in a kinking mode. The damage propagates until the laminate is completely failed. As indicated by previous studies,[11,13] a somewhat more gradual failure is observed where there is a gradient (e.g., near a hole) in the stress field.

In these studies[7–16] and other similar investigations, no attempt has been made to follow the progression of damage prior to catastrophic failure. The progressive nature of failure, in many cases, is a characteristic property of laminated composites, depending on both resin properties and stacking sequence. Several different failure processes are prevalent when these laminates are stressed, and the key aspects of failure must be identified. Motivated from such an understanding, Waas and Babcock[14] recently completed a detailed experimental investigation to understand

the initiation and propagation of failure in laminates in the presence of a stress raiser. They studied damage initiation and propagation throughout the entire load history via real time holographic interferometry and photomicrography of the hole surface. Post failure examination of the damaged specimen was accomplished using ultrasonic inspection and an optical microscope. From this study, they concluded that the damage is found to initiate by a combination of fiber microbuckling and kinking, and delamination buckling was determined to be the mechanism by which the damage propagates to catastrophic failure. However, the process leading to the formation of the kink band remains unknown, and a mechanics model describing this zone is still nonexistent.

Existing Models

Waddoups et al[17] assumed that intense energy regions exist at the edges of the hole. They modeled these regions as cracks emanating from a circular hole, and then applied linear elastic fracture mechanics (LEFM); this model has been referred to as the Inherent Flaw Model (IFM). Similarly, other applications[18-22] of LEFM to composite laminates exist. Whitney and Nuismer[23] developed two stress fracture criteria for tensile loaded composite laminates containing stress concentrations (circular holes and straight center cracks). These criteria[23] are based on two parameters (unnotched tensile strength, σ_o and a characteristic dimension), but do not require LEFM. One criterion assumes that failure occurs when the stress at a characteristic distance, d_o, from the discontinuity reaches the tensile strength σ_o of the unnotched material, while the other criterion assumes that failure occurs when the average stress over some characteristic distance, a_o, reaches the unnotched tensile strength. These criteria were subjected to further experimental scrutiny by Nuismer and Whitney.[24] However, due to large scatter in the data, no conclusive statement

concerning the accuracy of the models was presented. Although Whitney and Nuismer assumed the characteristic distances to be a material property independent of laminate geometry and stress distribution, it should be noted that these distances are geometry and notch size dependent. Furthermore, these adjustable parameters have not yet been related to microstructural features and do not result from a mechanics analysis. In 1979, Nuismer[25] extended the average stress failure criterion to compression applications for countersunk fastener holes (both loaded and unloaded), with acceptable agreement between experimental data and theoretical predictions. However, again, no conclusive statements about the accuracy of the models were made. Recently, Aronsson and Bäcklund[26,27] applied Hillerborg's Damage Zone Model (DZM) which is very similar to the Dugdale/Barenblatt Model,[28] to predict the static fracture of notched (e.g. cracks, holes) composite laminates loaded in tension. In this model, the physical damage zone (includes delamination, fiber and matrix fracture, matrix yielding, and fiber debonding) is represented by an equivalent crack containing cohesive stresses and treated by a Dugdale/Barenblatt[28] type analysis. The cohesive stresses are assumed to act on the crack surfaces. Increased damage corresponds to an increased crack tip opening displacement v and a reduction of the cohesive stresses, σ. An assumed linear relationship between σ and v has shown good results for the cases tested thus far. A finite element program known as FRACOM and used in Refs. 26 and 27 is the numerical technique used to model the nucleation, stable growth, and unstable growth of the crack. It is important to note that the area under the σ-v curve is defined to be the apparent fracture energy G_c^* and that the maximum allowed cohesive stress is σ_o, the unnotched tensile strength of the laminate. The crack is assumed to form when the cohesive stress reaches σ_o. G_c^* represents the sum of the energies dissipated in the various microscopic failure

processes. The value of G_c^* which gives the same fracture load as the experimental average is taken as the adequate G_c^* for each material system. The laminate is assumed to be a linear elastic material, and the damage zone is represented along the crack surfaces by the cohesive zone. The model has yielded accurate strength predictions for composites with through the thickness cracks, circular holes of various radii, and oval and rectangular holes of various sizes. Additionally, it should be noted that G_c^* does not appear to be geometry or crack length dependent.

Method of Investigation

The primary objectives of this proposed thesis have been (1) to evaluate the accuracy with which the growth of damage that precedes final compressive failure may be predicted by an existing model; (2) to propose, if necessary, a new model to predict compressive failure in composite laminates; (3)to determine the extent and nature of subsurface damage in the shear crippling zone using systematec sectioning techniques; and (4) to develop a three-dimensional schematic of the shear crippling zone through the thickness of the laminate.

In this thesis research, specimens containing circular, center holes were loaded in compression to failure at a relatively slow rate to provide more stable growth of the shear crippled zone. During loading, the surface damage development was monitored prior to catastrophic failure. Because the crack-like appearance of the damage progression in composite laminates is very similar to the Dugdale/Barenblatt[28] analysis, Newman's Dugdale type analysis[29] has been studied to evaluate its capability to predict the response of open hole composite laminates loaded in compression. This analysis predicts the size of the damage zone as a function of load or nominal stress, with the stress supported by the shear crippling zone being an adjustable

parameter similar to the yield strength in a Dugdale analysis. The initial efforts in this program were to study the accuracy with which one can predict the load vs. damage zone size relationship for specimens with different hole sizes after determining the "effective yield strength" in the shear crippled zone for specimens with the same hole size.

Several coupon compression tests were interrupted prior to catastrophic failure to allow for a more careful examination of fiber shear crippling and/or fiber microbuckling. These observations were accomplished using nondestructive examination (NDE) techniques, ultrasonic C-scan and dye penetrant enhanced X-radiography, and scanning electron microscopy. Direct observation of the specimen reveals the surface size of the shear crippling zone. To determine the extent of this zone through the laminate thickness, systematic sectioning techniques were developed and employed. Sectioning investigations were conducted through the thickness of three specimens; each section was examined in the scanning electron microscope (SEM). From these sectioning studies, the extent and mode of failure were determined, and a three-dimensional schematic of the shear crippling zone was developed.

CHAPTER II

DUGDALE TYPE ANALYSIS

Derivation of the Dugdale Model

In this section, a concise review of the derivation of the Dugdale model is presented.[29,30,31] An analytical solution for the Dugdale model is obtained for a through crack in a wide plate. The assumptions of the model are as follows:

1. The material is elastic-perfectly plastic, i.e., no strain hardening, as shown in Fig. 2.

2. The stress state is plane stress, requiring the plate to be relatively thin.

3. The geometry is a through crack in a wide plate.

4. The plastic zone is a long narrow strip ahead of the crack tip. This shape is defined as a Dugdale type zone, and is more likely to be found in polymeric materials because of the variation in yield strength with hydrostatic tension.

Dugdale assumed an effective crack length which is longer than the physical crack, as shown in Fig. 3. The assumption was that an actual center crack of length $2a$ could be modeled as a crack of length $2(a + \rho)$, where ρ is the length of the plastic zone ahead of the crack tip. Furthermore, this plastic zone could be modeled as a crack with compressive surface tractions equal to the yield stress, σ_{ys}, of the material. The size of ρ is selected so that the stress intensity associated with the compressive loading exactly cancels the stress singularity associated with the applied tensile stress, guaranteeing finite stress everywhere in the coupon. This condition of finite stresses is expressed as follows:

$$K_\sigma = -K_\rho \quad \text{or} \quad K_\sigma + K_\rho = 0 \tag{1}$$

Fig. 2 Stress-strain relationship for elastic-perfectly plastic material.

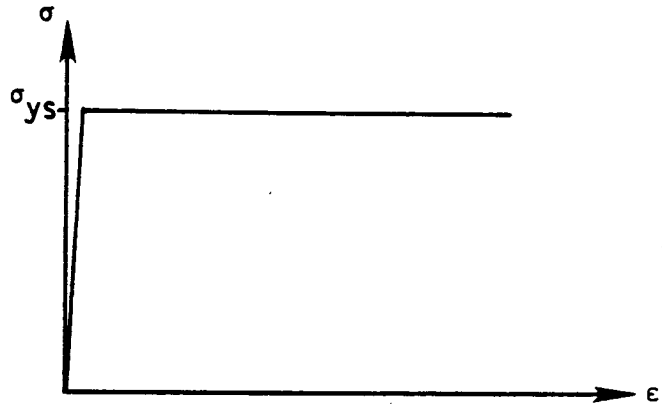
σ
σys
ε

Fig. 3 Dugdale crack.

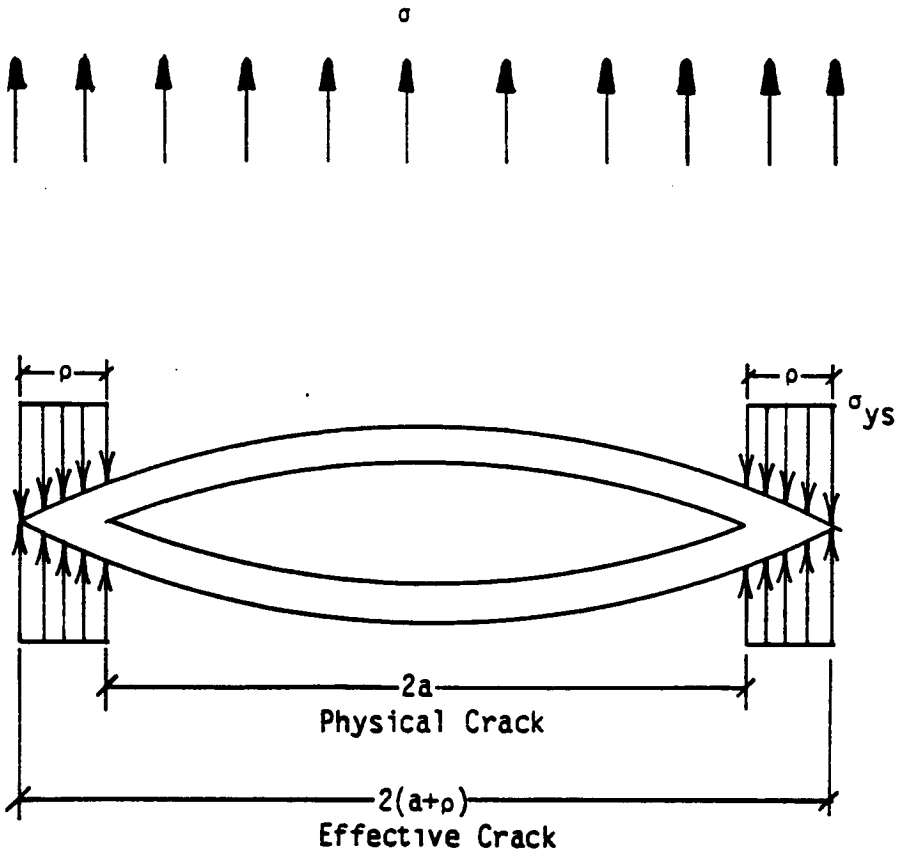
σ
ρ
ρ
σys
2a
Physical Crack
2(a+ρ)
Effective Crack

and is illustrated in Fig. 4.

A crack with an internal tensile stress p distributed across its length has a stress intensity factor equal to

$$K_I = p\sqrt{\pi a}. \tag{2}$$

The Dugdale approach is modeled as a crack with internal wedge pressure. This pressure acts as a series of evenly distributed wedge forces, P (force per unit plate thickness), as illustrated in Fig. 5. The general solution for an eccentrical point force may be described by Green's function and is given by

$$K_{IA} = \frac{P}{\sqrt{\pi a}}\sqrt{\frac{a+x}{a-x}} \text{ and } K_{IB} = \frac{P}{\sqrt{\pi a}}\sqrt{\frac{a-x}{a+x}} \tag{3}$$

where K_{IA} and K_{IB} are the stress intensity factors for crack tips A and B respectively.

For a uniformly applied internal pressure, one may assume that the pressure p acts as a series of evenly distributed crack opening forces from s to the crack tip (as in the Dugdale case). Then, K may be determined from the following integration over the crack surface:

$$K = \int_s^a (K_{IA} + K_{IB})\, dx = \int_s^a \frac{P}{\sqrt{\pi a}}\left(\sqrt{\frac{a+x}{a-x}} + \sqrt{\frac{a-x}{a+x}}\right) dx \tag{4}$$

$$K = 2P\sqrt{\frac{a}{\pi}}\frac{dx}{\sqrt{a^2 - x^2}}. \tag{5}$$

The integration is carried out by a change of variables, $x = a\cos\phi$, and the solution is

$$K = 2P\sqrt{\frac{a}{\pi}}\cos^{-1}\left(\frac{x}{a}\right)\Bigg|_s^a = p\sqrt{\pi a} \tag{6}$$

which is the same as eq. (2). Applying eq. (6) to the Dugdale crack of Fig. 3, the integral must be taken from $s = a$ to $s = (a + \rho)$. Thus, a must be substituted for

Fig. 4 Crack tip stress intensity.
a) Stress singularity at crack tip of tensile loaded coupon.
b) Compressive stress intensity at crack tip attributed to compressive surface stresses over the plastic zone.
c) Finite stress distribution in tensile loaded coupon.

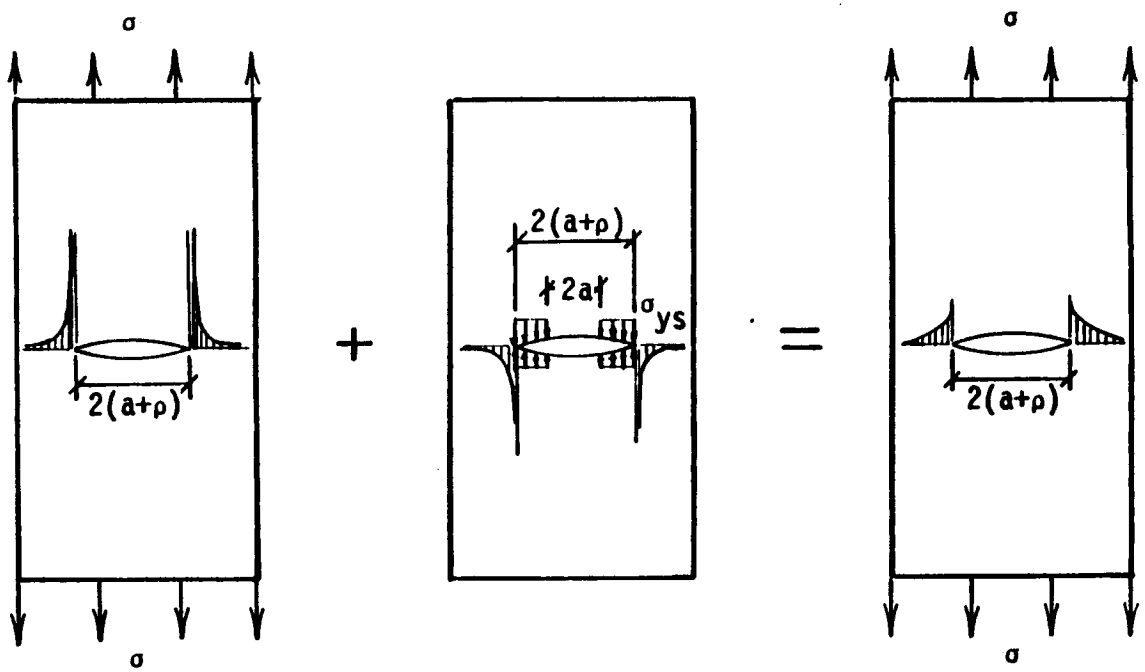

(a) (b) (c)

Fig. 5 Crack with applied wedge forces where P=force per unit plate thickness.

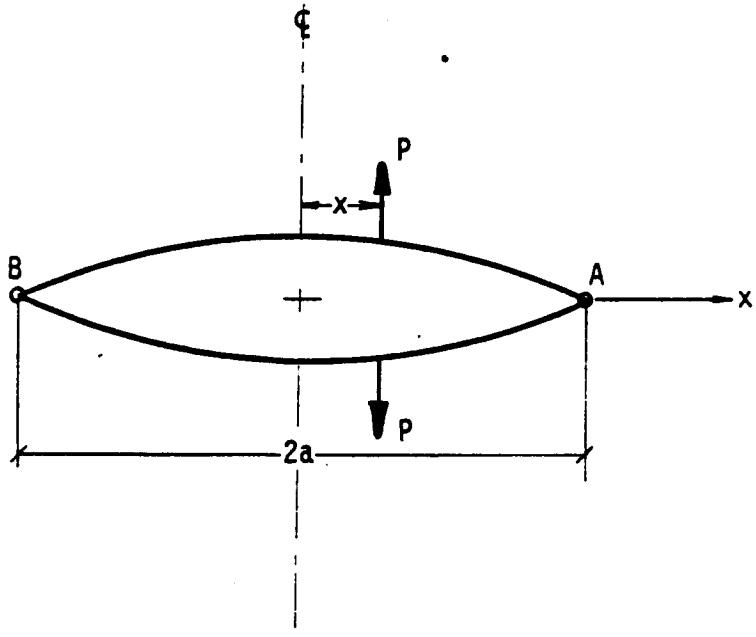
℄
P
x
B
A
x
P
2a

s, $(a+\rho)$ for a, and $-\sigma_{ys}$ for P. Therefore,

$$K_\rho = -2\sigma_{ys}\sqrt{\frac{a+\rho}{\pi}}\cos^{-1}\left(\frac{a}{a+\rho}\right). \tag{7}$$

From Fig. 4c,

$$K_\sigma = \sigma\sqrt{\pi(a+\rho)}. \tag{8}$$

According to eq. (1), $K_\sigma = -K_\rho$ and thus,

$$\sigma\sqrt{\pi(a+\rho)} = 2\sigma_{ys}\sqrt{\frac{a+\rho}{\pi}}\cos^{-1}\left(\frac{a}{a+\rho}\right) \tag{9}$$

which reduces to

$$\frac{a}{a+\rho} = \cos\left(\frac{\pi\sigma}{2\sigma_{ys}}\right). \tag{10}$$

Neglecting higher order terms of the infinite series for cosine, one may further reduce eq. (10) to

$$\rho = \frac{\pi^2\sigma^2 a}{8\sigma_{ys}^2} = \frac{\pi K^2}{8\sigma_{ys}^2}. \tag{11}$$

Application of Dugdale Model

The Dugdale model, which works best for plastics but surprisingly well for metals, has been applied to ductile open hole composite laminates loaded in compression. This model was selected because composites containing open holes have compressive failures that are preceded by the development of a damage zone that resembles a flat, tension fatigue crack in a metal except that the stress directions are reversed. An example of this composite damage zone was shown in Fig. 1. The shear crippling zone at each edge of the hole has been compared to the plastic zone in metals. We have assumed that although the fibers are broken, the debris in the crush zone continues to carry load. Thus, one could assume that

as the crush zone grew across the specimen width, a constant crushing pressure σ_{oc} would exist over the length of the crush zone, ρ. The crush pressure, σ_{oc}, is completely analagous to the constant tensile flow stress, σ_{ot}, assumed to be present in the Dugdale plastic zone of a specimen containing a crack and loaded in tension.

Newman[29] applied the Dugdale approach to homogeneous, isotropic materials containing a crack in a finite plate and also to cracks emanating from a circular hole in a finite plate. His result, which is derived in detail in Ref. 29, for cracks emanating from a circular hole in a finite width specimen (see Fig. 6) is as follows:

$$SF_h^s F_w^s - \alpha\sigma_{ot}\left[1 - \frac{2}{\pi}\sin^{-1}\left(\frac{c}{d}\right)\right] F_h^\sigma F_w^\sigma = 0. \tag{12}$$

For a given S, w, r, c, α, and σ_{ot}, eq. (12) is solved for d using an iterative technique. However, $\rho = d - c$, and thus, the plastic zone size ρ is determined.

This work has followed Newman's analysis for cracks emanating from a circular hole in a finite width specimen, but the open hole composite laminates were modeled with $c = r$ and $\sigma_{ot} = \sigma_{oc}$. However, instead of using an iterative solution, curves of S vs. ρ have been generated with σ_{oc} as a variable parameter for the various hole sizes. This rearranged solution for eq. (12) follows:

$$S = \frac{\alpha\sigma_{oc}\left[1 - (2/\pi)\sin^{-1}(c/d)\right] F_h^\sigma F_w^\sigma}{F_h^s F_w^s} \tag{13}$$

where

$$\rho = d - c. \tag{14}$$

The specimen configuration for this solution is shown in Fig. 7. Appendix A contains the listing of the computer program (altered from Newman's iterative solution) that generates the theoretical S-ρ curves. The generated curves will be presented later with the experimental data in the Results chapter of this thesis.

Fig. 6 Geometry for Newman's analysis.

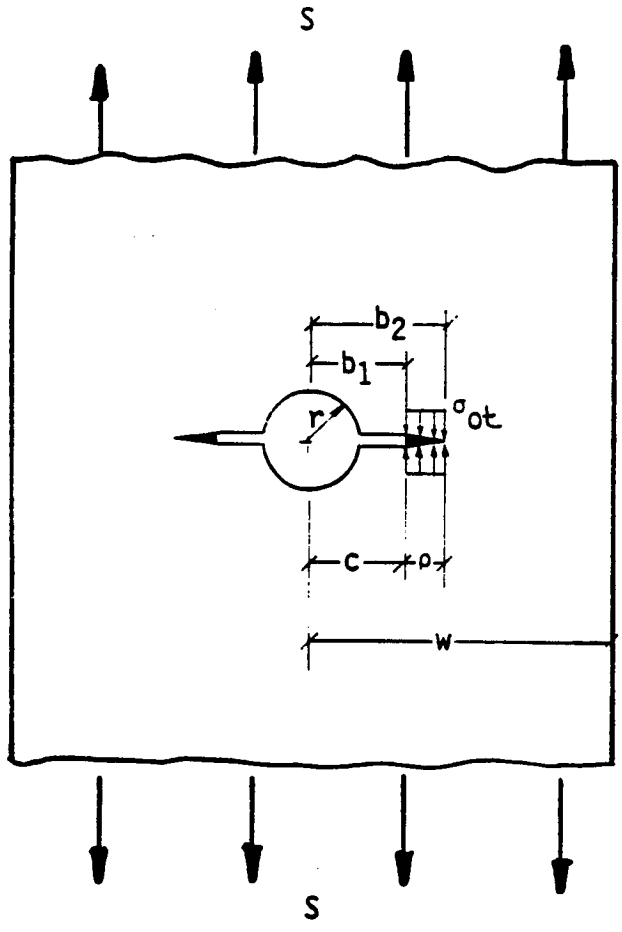
S
b_2
b_1
r
σ_{ot}
c
ρ
w
S

Fig. 7 Specimen configuration for the Dugdale model applied to open hole composite laminates loaded in compression.

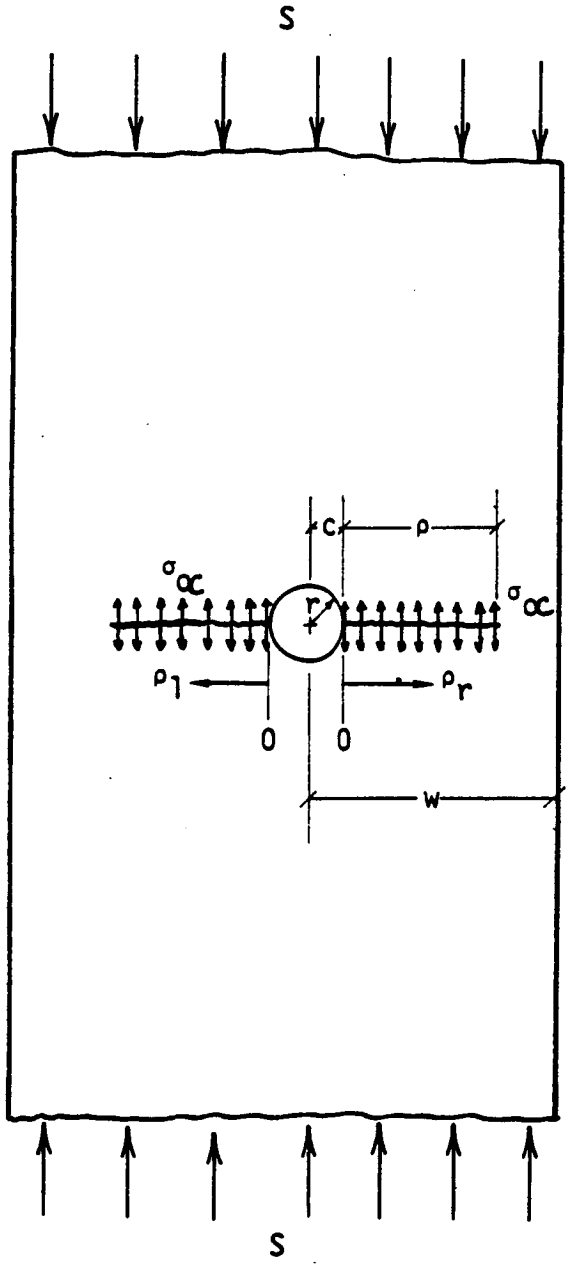
S
c
ρ
σ_∞
r
σ_∞
ρ_l
ρ_r
0
0
w
S

Additionally, it should be noted at this time that the Dugdale type analysis for the crush zone in compression loaded composite laminates satisfies all geometry requirements of Newman's analysis and that plane stress ($\alpha = 1$) conditions are assumed to exist at the hole.

CHAPTER III

EXPERIMENTAL PROCEDURES

Materials

Three composite material systems were tested in this investigation: (1) AS4/PEEK, a thermoplastic, (2) T2C145/F155, an epoxy, and (3) IM6/HST-7, an interleaf material.

AS4/PEEK consists of high strain carbon fibers (AS4) embedded in a semi-crystalline thermoplastic matrix known as polyetheretherketone (PEEK). PEEK is an aromatic polyether resin which is primarily useful because of its exceptional toughness as well as chemical resistance. PEEK is sold under the trade name "Victrex" PEEK by Imperial Chemical Industries, Limited (ICI), United Kingdom, and became available in 1981.[32] A 48-ply orthotropic composite laminate of AS4/PEEK with a stacking sequence of $[\pm 45/0_2/\pm 45/0_2/\pm 45/0/90]_{2s}$ was investigated. This stacking sequence was selected because it is typically tested and used in strength-critical applications, such as aircraft structural components.[9] This material was supplied by the grant sponsor, NASA Langley Research Center, Hampton, Virginia, who obtained the laminate from ICI.

The T2C145/F155[33–35] prepreg was purchased from Hexcel Corporation and consists of intermediate modulus and intermediate strength carbon fibers, CELION 12000,[33,34] embedded in a medium cross-linked density, medium toughness epoxy with 6%, by weight, elastomer (4% liquid and 2% solid rubber particles) addition[34,35] to the prepreg. This laminate was fabricated at Texas A&M University following the procedure specified by Hexcel.[35]

IM6/HST-7 is a composite material for structural components requiring ex-

tremely high toughness and impact properties. The resin, CYCOM HST- 7,[36] achieves its very high toughness through the engineered combination of two discrete layers. A high modulus resin is used on the graphite fibers to give the resin system its structural properties and environmental resistance. A separate high strain resin layer is applied to one side of the graphite prepreg to add toughness to the system. This separate neat resin layer, the interleaf, is designed to remain a discrete layer through the cure cycle and to provide strain isolation between the plies of the cured laminate. The prepreg manufacturer for this material is American Cyanamid, but the composite panel was supplied by Bell Helicopter, Fort Worth, Texas. The quasi-isotropic F155 and HST-7 panels consisted of 32 plies with a stacking sequence of $[(0/\pm 45/90)_s]_4$. The 0° fibers were placed in the surface plies to provide opportunity to directly observe the shear crippling process.

For quick reference, each laminate's stacking sequence, average panel thickness t, and resin classification is listed in Table I. Lamina material properties (E_1, E_2, G_{12}, and ν_{12},) for each system were obtained through private communications. These lamina properties, along with their source, are summarized in Table II. Note that standard convention is followed for these properties. The 1-direction is parallel to the fiber direction while the 2-direction is perpendicular to the fibers.

Precision compression specimens were made of 4140 steel for machine alignment verification studies. The Rockwell C hardness for this material was 33, and the ultimate tensile strength was 1027 MPa.

Methods

Material Property Characterization

Each material system was characterized by its laminate engineering constants,

TABLE I. COMPOSITE LAMINATE MATERIAL SYSTEMS.

MATERIAL	STACKING SEQUENCE	NO. OF PLIES	t, mm	RESIN CLASSIFICATION
AS4/PEEK	$[\pm 45/0_2/\pm 45/0_2/\pm 45/0/90]_{2S}$	48	6.24	SEMI-CRYSTALLINE THERMOPLASTIC
T2C145/F155	$[(0/\pm 45/90)_S]_4$	32	4.91	RUBBER-TOUGHENED EPOXY
IM6/HST-7	$[(0/\pm 45/90)_S]_4$	32	6.63	HIGH MODULUS EPOXY W/HIGH STRAIN INTERLEAF

TABLE II. LAMINA MATERIAL PROPERTIES.

MATERIAL	t/PLY, mm	E_1, GPa	E_2, GPa	G_{12}, GPa	ν_{12}
AS4/PEEK[37]	0.137	123	9.38	2.96	0.310
T2C145/FISS[34]	0.142	126	8.96	4.14	0.200
IM6/HST-7[38]	0.201	141	8.48	3.93	0.331

elastic modulus, delamination fracture toughness, and representative material cross-section. The laminate engineering constants, E_x, E_y, G_{xy}, and ν_{yx}, for each material system were computed using a basic laminate theory program. Since all laminates tested did not have quasi-isotropic stacking sequences, these normal stress distributions and the stress concentration factors (SCF) adjacent to the circular hole were determined for each material system using the approximate, extended isotropic solution developed by Konish and Whitney.[39] The SCF is defined as the ratio of the maximum normal stress tangent to the hole perimeter to the remote tensile stress on the plate. This analysis assumes that the plate is large compared to the diameter of the hole, homogenous, elastic, and anisotropic within its plate. This solution is an extended isotropic solution which agrees, at least in form, to the binomial series expansion of the exact solution. Konish and Whitney compared results from the exact orthotropic solution, scaled isotropic solution, and the extended isotropic solution. They concluded that the extended isotropic solution was superior to the scaled isotropic solution because of the good agreement between the extended isotropic and exact orthotropic solutions for a number of test cases.

Compression modulus tests were conducted on specimens identical to the open hole specimens (2.54 cm wide, 12.70 cm long, with a 5.08 cm gage length) except without the hole. These specimens were strain-gaged front and back with 0/90 strain gages were subsequently loaded in displacement control at the relatively slow rate of 0.0127 cm/min. They were later failed in compression to determine the ultimate compressive strength of the materials. To supplement these modulus measurements, one standard three- point bend test was run for each material system, and the stiffness was computed. These specimens were cut from the end of the undamaged open hole specimens. It should be noted that the author realizes the unsupported

length in these tests is too short to be true modulus and ultimate compression tests. Bogetti et al[40] evaluated the IITRI Compression Test Method including the required aspect ratio (gage length normalized by specimen thickness) to eliminate end loading effects in the gage section. Their results indicate an aspect ratio between 4 and 8 is adequate, which these tests satisfy. However, the purpose of these tests was to simply characterize each panel of material to determine comparative, if not absolute values of strength and modulus.

The fracture toughness, or the resistance to fracture in the presence of a crack, is normally expressed in terms of the critical strain energy release rate, G_c. G_c for mode I loading (G_{Ic}) was determined using double cantilever beam (DCB) specimens from the HST-7 and F155 panels of material. The PEEK panel of material provided for this study did not contain a teflon strip, which would have allowed DCB specimens to be prepared from it. Thus, delamination fracture toughness values from the literature were used for this system. The DCB specimens were 2.54 cm wide, 25.4 cm long, containing a teflon insert at the midplane of one end of the specimen to provide a delamination starter crack. This insert was 2.54 cm square and approximately 0.03 mm thick. The edges of the specimens were painted silver so that the crack length could be easily detected and measured. Magnification of the crack tip also aided this measurement.

The experimental set-up for mode I loading of composite DCB specimens is shown in Fig. 8. This set-up includes a 445N load cell and a special fixture, similar to that described by Keary et al,[42] for load application. Test control and crack length measurement were performed by the author. The DCB specimens were loaded at a relatively slow rate of 1.27 mm/min. Six unload compliances were taken for each specimen. Load-displacement data was recorded on an X-Y recorder

Fig. 8 Experimental set-up for Mode I loading of composite DCB specimens.

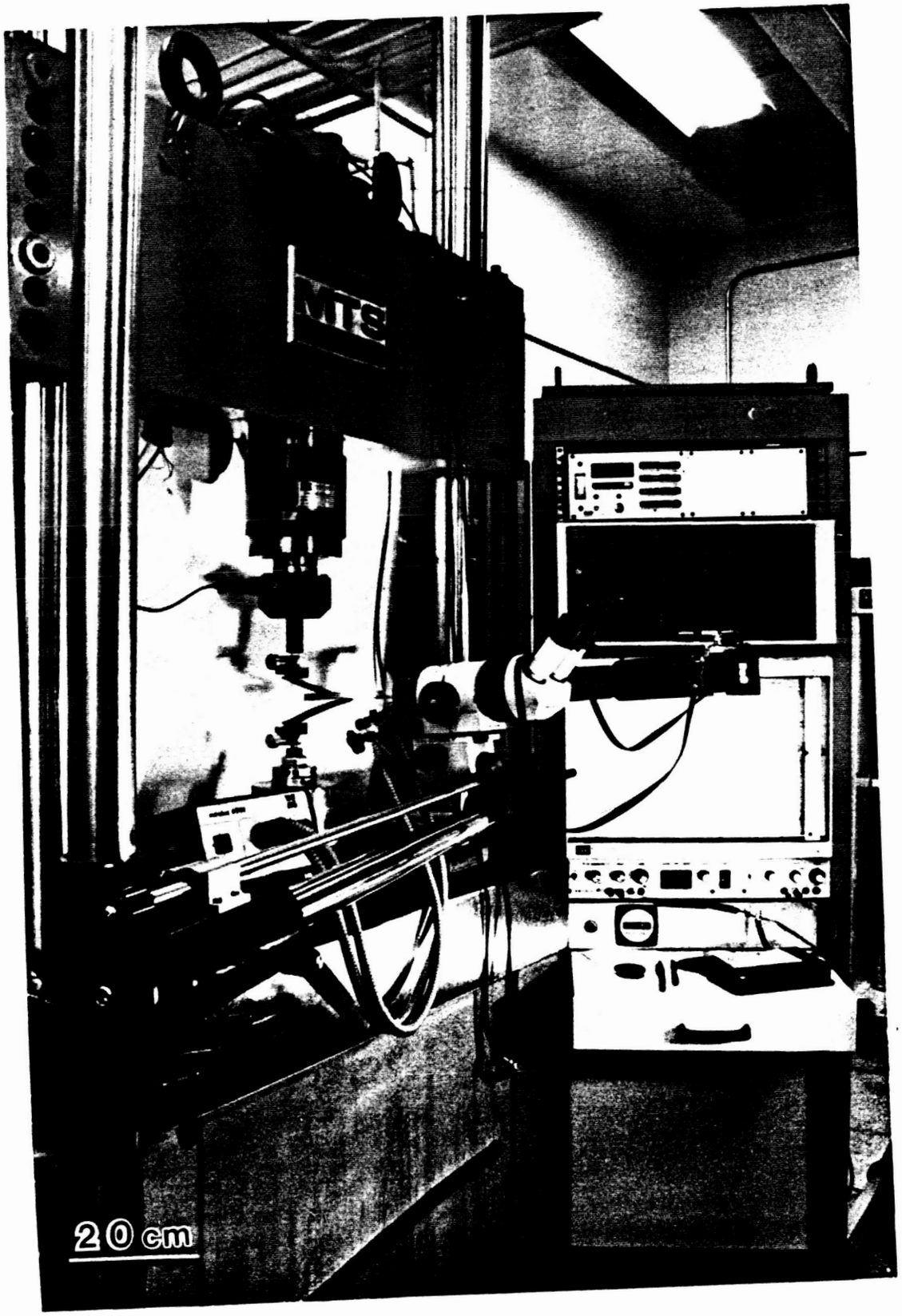

ORIGINAL PAGE IS
OF POOR QUALITY

to provide real-time observation of the load-displacement record. Additionally, data was transformed through a Hewlett-Packard Data Acquisition Unit (model HP 3497A) and recorded by a Hewlett-Packard computer (model HP 9816). G_{Ic} for each material system was computed by integrating to obtain the area under the load-displacement curve. For comparison, G_{Ic} was also computed using the approximate area, linear beam theory, and unload compliance methods described and compared in more detail by Hibbs.[42]

A representative cross-section (perpendicular to the 0° fibers) was cut from each material system. These cross-sections were polished and then examined in the SEM to provide a representative microstructure for each material system.

Compression Specimens

Open hole compression specimens were 2.54 cm wide by 12.70 cm long, with a 5.08 cm gage length (unsupported length), each containing a center hole, as shown in Fig. 9a. All of the specimens were machined at NASA Langley Research Center. The ends of the specimens were ground flat and parallel to maintain uniform loading during the end loading the specimens. The center holes were induced into the specimens using an ultrasonic drill press, Branson Sonic Power Drill. The ultrasonic drill press uses a diamond-impregnated core bit which is water cooled through the core. The holes were actually bored using an ultrasonic up/down motion, rather than the traditional rotational drilling methods. Hole diameters were 0.16 cm, 0.32 cm, and 0.64 cm. These diameters were selected to provide different notch stress distributions. The stress field decay is the same for all holes when normalized by the hole diameter. However, when looking at the absolute stress field, the decay is more rapid for smaller hole diameters and plates of finite size, and thus, the notch stress distributions are different.

Fig. 9 Open hole compression test specimen.
a) Compression test specimen.
b) Strain gage specimen configuration.

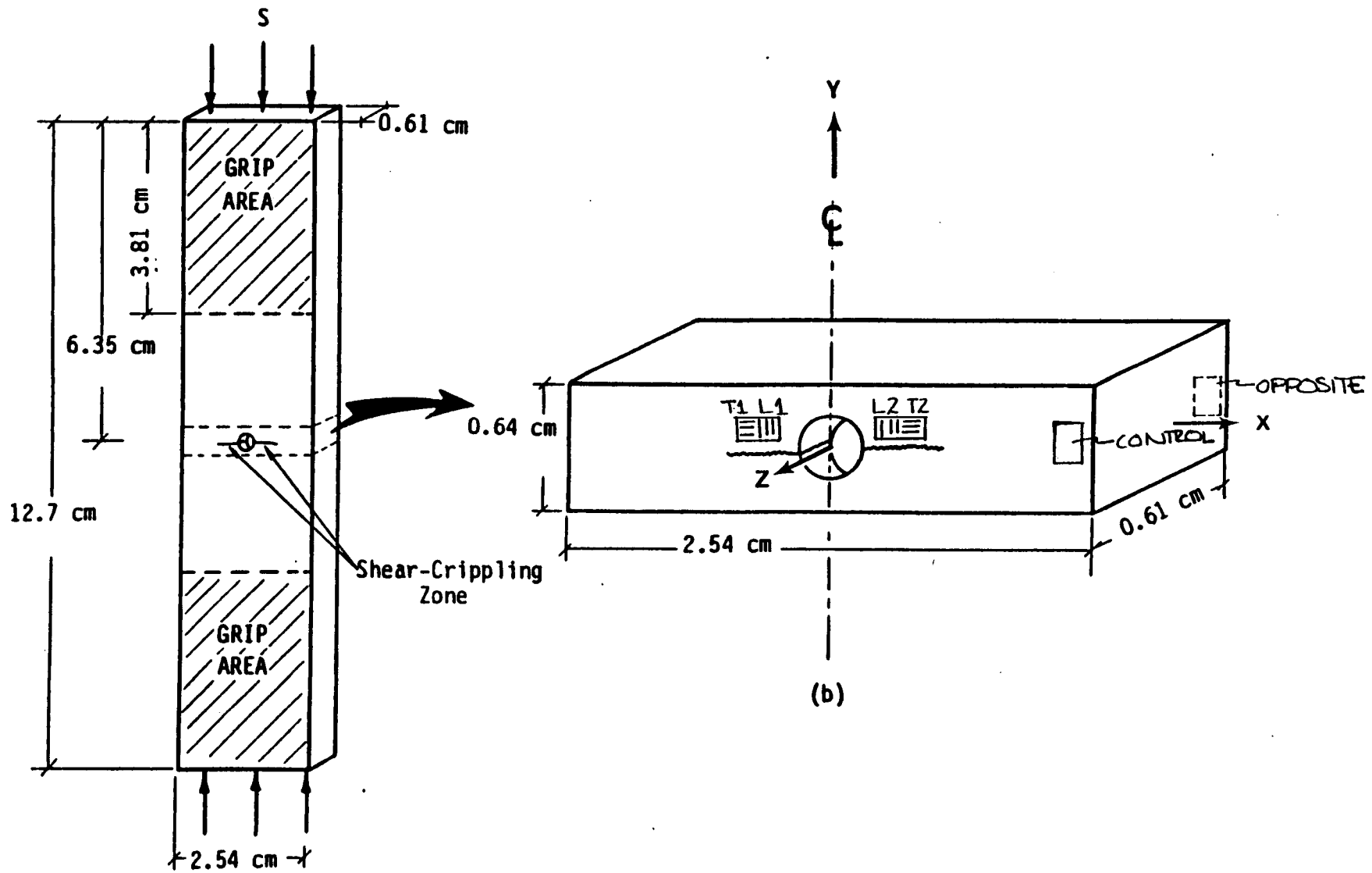
S
0.61 cm
GRIP AREA
3.81 cm
6.35 cm
12.7 cm
Shear-Crippling Zone
GRIP AREA
2.54 cm
(a)
Y
C
L
T1 L1
L2 T2
Z
CONTROL
OPPOSITE
X
0.64 cm
2.54 cm
0.61 cm
(b)

For strain gage control testing, longitudinal strain gages (designated control and opposite) were placed on each specimen front and back, on the horizontal centerline at the edge of the specimen, as shown in Fig. 9b. To determine the load carried by the shear crippling zone, additional 0/90 strain gages (L1, T1, L2, T2) were located on the specimen approximately $2r$ from the hole center and 25° above the horizontal centerline, also shown in Fig. 9b. Strain gage L3 (longitudinal only) was used to compare the strains over the shear crippling zone and in the control gage with the measured strain at a remote location. The location of these gages was predetermined from stress contour plots provided by Dr. Paul Tan of Analytical Services & Materials, Inc., Hampton, Virginia.

For machine alignment verification studies, two precision compression specimens were made of 4140 steel. These specimens were also 2.54 cm wide and 12.70 cm long with a 5.08 cm gage length, but without a center hole. Additionally, these specimens were machined with ends, surfaces, and edges ground flat and parallel to produce the most "nearly perfect" compression test. These specimens were strain gaged front and back with longitudinal strain gages.

Compression Test Methods

Compression tests were conducted in a specially designed high axial alignment Material Test System (MTS) machine in the Materials and Structures Laboratory of Texas A&M University. Figure 10a shows this test apparatus. Figure 10b is a close-up of the specimen configuration in the machine grips with the stereomicroscope in the background. The specimens tested were loaded in compression to failure in the servo-controlled hydraulic test stand at a relatively slow rate in strain gage control to provide more stable growth of the shear crippling zone. The initial strain rate was approximately $1000\mu\epsilon$/min to approximately 80% of the expected

Fig. 10 Compression test facilities.
a) Compression test set-up with stereomicroscope and video attachments.
b) Specimen configuration in the hydraulic grips with the stereomicroscope in the background.

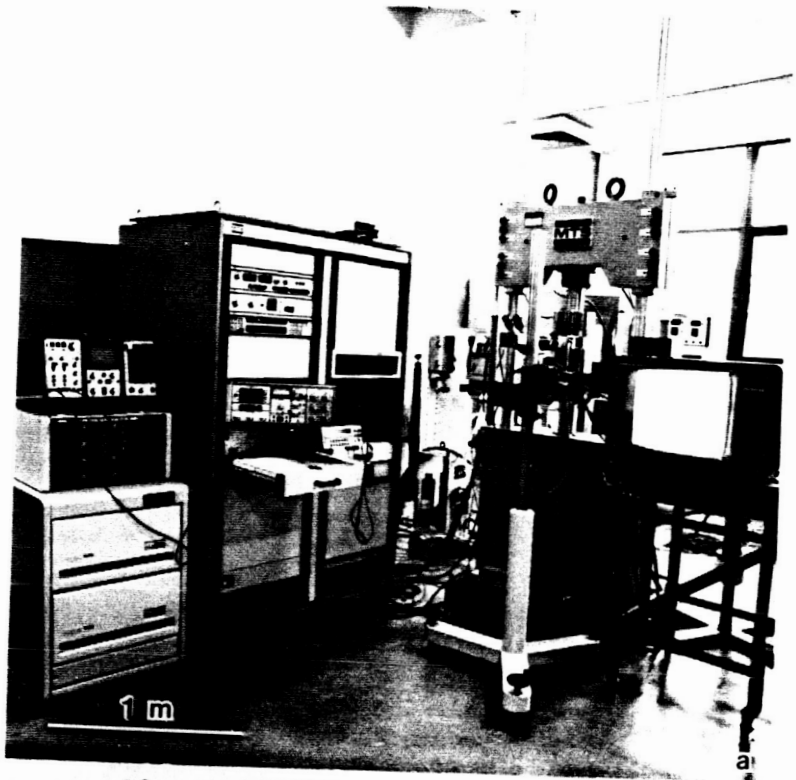

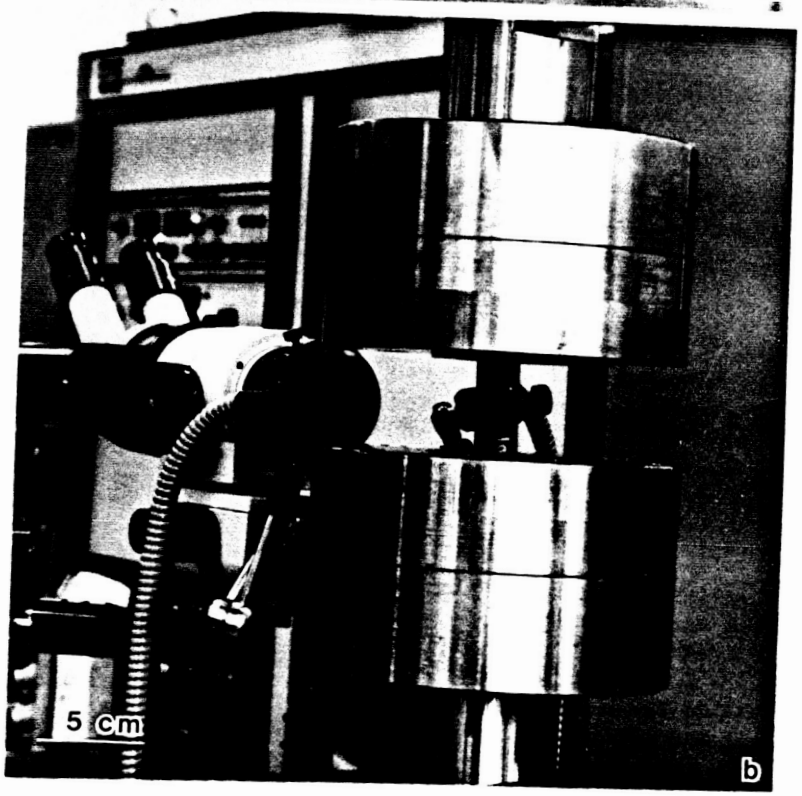

load for visible initiation of the shear crippling zone. The strain rate was then changed to $100\mu\epsilon$/min for the next 10% of loading and then changed to $10\mu\epsilon$/min for the duration of the test. If any damage was detected prior to these designated load levels, the strain rate was immediately changed to $10\mu\epsilon$/min. This procedure guaranteed some stable growth of the shear crippling zone prior to catastrophic failure. The surface damage development adjacent to the center hole which precedes failure was monitored and recorded using a Wild M8 Zoom Stereomicroscope (shown in Figs. 10a and 10b) equipped with a video system for real-time recording. Prior to catastrophic failure, some tests were interrupted to provide specimens with significant damage for determination of load carrying capacity, nondestructive examination, and sectioning studies of the shear crippling zone.

The specially designed compression MTS is noted for its precision load frame. This frame contains a stiffened actuator to limit the lateral (out of plane) motion of the lower grip. Additionally, the design includes allowances at the cross-head/upper grip joint so that the alignment may be corrected more easily than in the standard load frame. This MTS contains standard hydraulic wedge-action grips rather than the more alignment-guaranteed precision grips. The alignment procedure includes setting the cross-head in the proper location and then aligning the two grips concentric to each other. Two tests were designed to verify the machine alignment. First, the grip alignment checking apparatus, shown in Fig. 11, is used to verify the alignment of the upper and lower grips with each other. The grip alignment checking apparatus, designed by Toby Selcer of the Materials and Structures Laboratory, consists of two pieces: (1) a steel cylinder for reference measurements and (2) a 20.32 cm diameter steel disk turn table. Two 5.08 cm diameter cylinders were made: one is 7.62 cm long for shorter gage length tests

Fig. 11 Grip alignment checking apparatus.

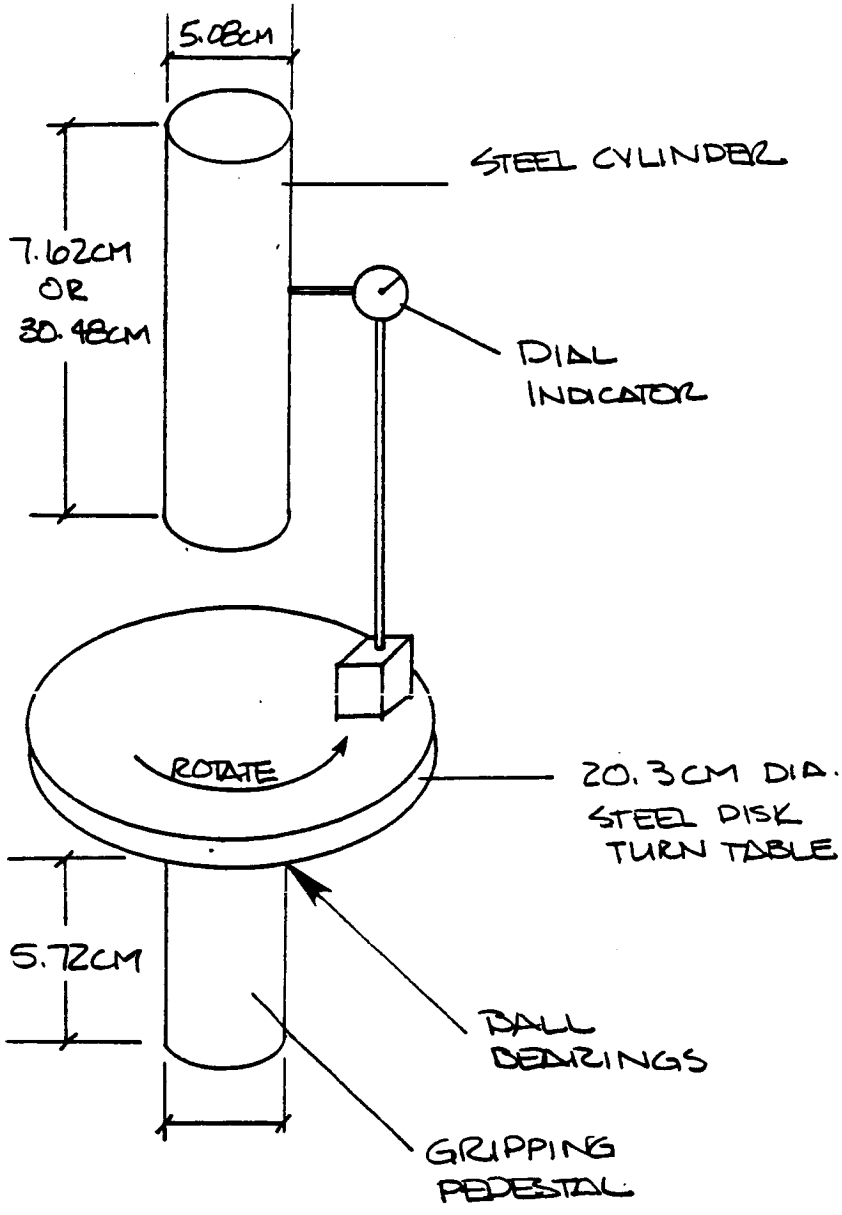

and the other one is 30.48 cm long for longer gage length tests. The turntable is connected to a gripping pedestal through ball bearings to allow rotation of the turntable. A spring-loaded dial indicator connected to a magnetic base is "clamped" to the turntable. In this case, the shorter cylinder is gripped by one grip while the pedestal and turntable is gripped in the other grip. The turntable is rotated and the dial indicator measures the accuracy of the alignment as it traverses the circumference of the cylinder. Then the pedestal and cylinder are interchanged and the same process is followed. If the alignment is not good enough, it is corrected, and then the grip alignment checking apparatus is used again. This sequence was followed until the alignment repeated itself to ±0.025 mm. Second, one of the strain-gaged, precision compression specimens was loaded in compression to full machine capacity (88.96 kN), unloaded, turned around, and then reloaded. The stress-strain curves for the front and back gages of each specimen were compared to verify the axial alignment. These two alignment tests (grip alignment checking apparatus and precision specimens) were performed prior to each session of compression tests in this MTS.

Load Transmission Through the Damage Zone

The load transmitted through the shear crippling zone was measured using 0/90 strain gages (L1, T1, L2, T2) located just above the shear crippling zone as shown in Fig. 9b. Examples of these strain gaged specimens are shown in Figs 12a (PEEK) and 12b (HST-7). The damage zones in each of these figures are indicated with arrows. These specimens were loaded in strain gage control as previously described in the compression test methods. The specimens were gaged prior to testing and then loaded until a shear crippling zone formed. If the damage zone initiated and/or propagated underneath the measuring gages (L1, T1, L2, T2), the

Fig. 12 Shear crippling zones (indicated by arrows) and surrounding strain gages.
a) AS4/PEEK specimen.
b) IM6/HST-7 specimen.
c) IM6/HST-7 specimen (shown in b) after removal of damage zone.

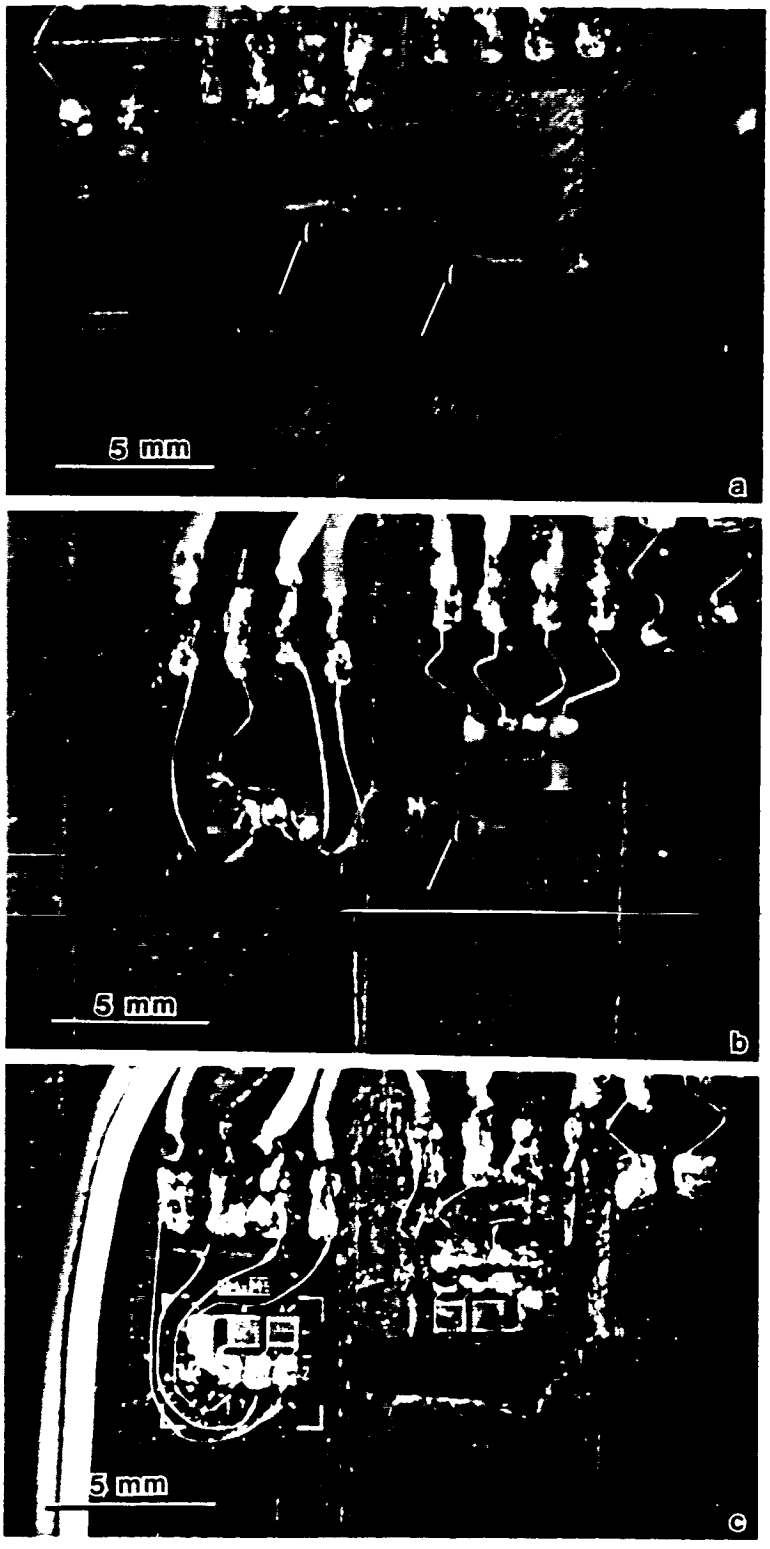

gages were removed and new gages placed just above the damage zone as close to $2r$ (shown in Fig. 9b) as possible. The strain gaged specimens were then reloaded and unloaded to provide a comparison of the strain measured just above the damage zone to the strain measured at a remote location.

In one HST-7 specimen (Fig. 12b), the shear crippling zone was removed to determine the local stress that could occur just above the crush zone if there were no material. The shear crippling zone was cut from the specimen using a Lastec diamond wire saw (0.20 mm diameter diamond inpregnated wire). This specimen, containing a 7.6 mm long slot and the necessary strain gages, is shown in Fig. 12c.

Nondestructive Examination

Nondestructive examination (NDE) of the shear crippling zone (prior to catastrophic failure) was accomplished using ultrasonic C-scans and dye-penetrant enhanced X-radiography. To act as an enhancing agent, a zinc iodide solution was applied to the surface damage to infiltrate to the connected interior damage. The zinc iodide solution consists of 60 grams of zinc iodide, 10 ml of water, 10 ml of isopropyl alcohol, and 10 ml of Kodak "Photo-Flo 600" to act as a wetting agent.

Scanning Electron Microscopy

Most nonconductive specimens examined in the scanning electron microscope (SEM) need to be coated with a thin film of conducting material. This coating is necessary to eliminate or reduce the electric charge which builds up rapidly in a nonconducting specimen when scanned by a beam of high-energy electrons. Because of the high conductivity of the carbon fibers and low conductivity of the resin and plastic cold-mount, charging was anticipated as a problem for the uncoated specimen. Therefore, each specimen surface for SEM examination was sputter-

coated with a thin film of gold palladium approximately 100Å thick, and then it was examined in a JEOL 25 SEM. Delamination fracture surfaces and unpolished shear crippling zones were examined at a relatively long working distance (48 mm) to provide a greater depth of field, and thus, facilitate the observation of the topography of the fracture surfaces. Polished specimen surfaces, specimen cross-sections and sectioning surfaces, were examined at a shorter working distance (10 mm) to increase the resolution and contrast highlights of the damage. Additionally, a low accelerating voltage of 5 kV was used to further increase the contrast of the specimen surfaces.

Sectioning Studies

Sectioning was performed on specimens that had been loaded in compression until a shear crippling zone formed. Figure 13 shows a detailed schematic of this specimen configuration. In order to section through the damage zone, the center 0.61 cm of length, containing the center hole and adjacent damage, (Fig. 13b) was cut from the specimens using a Struers Accutum Precision Saw (diamond blade). This center section was then cut along its vertical centerline (the Y axis) into two halves, designated L and R. For handling purposes, each of these halves was then mounted in plastic, cold-mount specimen stubs. The left half (L) was sectioned across the width of the specimen from the edge of the hole toward the edge of the specimen, examining the Y-Z plane at each section, while the right half (R) was sectioned through the thickness of the laminate, examining the X-Z plane at each section. For specimen L, the amount of material removed by sectioning has been designated x_k and is referenced across the width of the specimen from the edge of the hole, as shown in Fig. 14a. For specimen R, the material removed by the sectioning techniques has been designated z_k and is measured from the surface of

Fig. 13 Specimen configuration.
a) Compression test specimen.
b) Specimen for sectioning investigation.

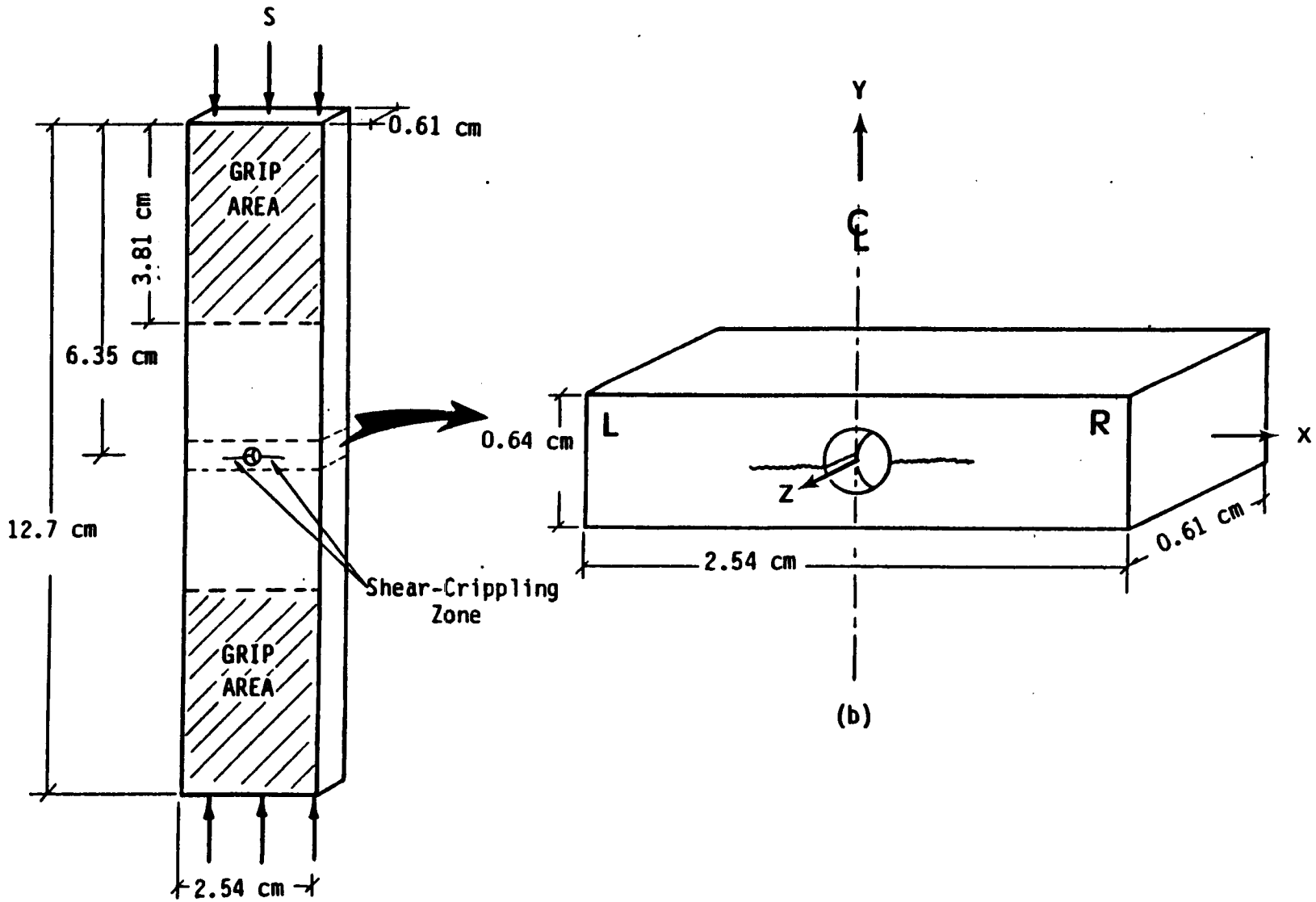
S
0.61 cm
GRIP
AREA
3.81 cm
6.35 cm
12.7 cm
Shear-Crippling
Zone
GRIP
AREA
2.54 cm
(a)
Y
L
0.64 cm
L
R
X
Z
0.61 cm
2.54 cm
(b)

the laminate, as shown in Fig. 14b. It should be noted that for simplicity, the Z-axis has been omitted from the drawings in Fig. 14. The Struers Precision Saw was utilized for the major sectioning cuts, while the thinner cuts and final polishing (preparation for microscopy) was accomplished using a microprocessor controlled grinding and polishing machine also manufactured by Struers (Abramin Automated Polishing Unit). Each sectioned surface of specimens L and R was examined in a JEOL 25 Scanning Electron Microscope (SEM).

Fig. 14 Sectioning configuration
a) Specimen L, examining the Y-Z plane at each section.
b) Specimen R, examining the X-Z plane at each section.

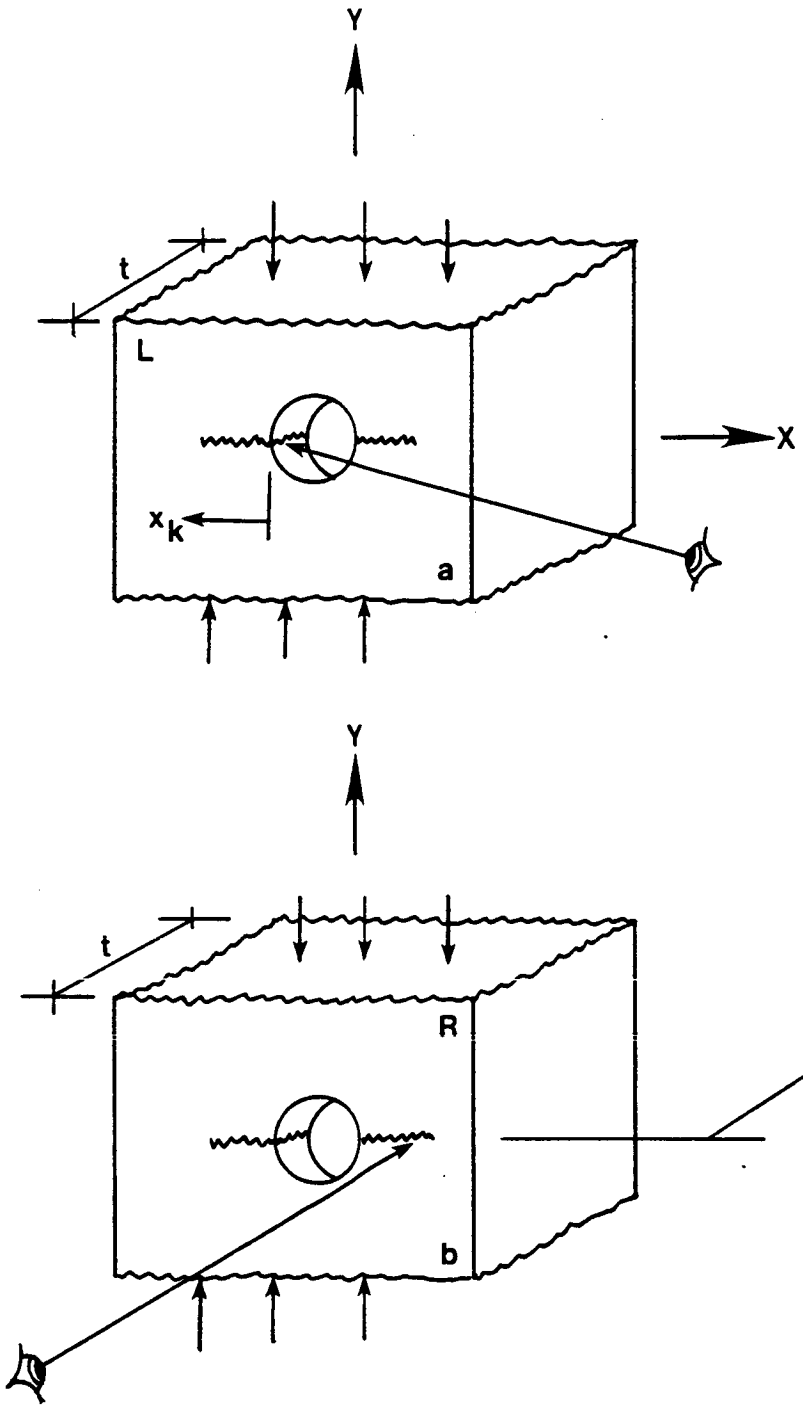
Y
t
L
X
x_k
a
Y
t
R
z_k
b

CHAPTER IV

RESULTS

Material Property Characterization

The laminate engineering constants, E_x, E_y, G_{xy}, and ν_{xy}, computed from a basic laminate theory program are summarized in Table III. Note that the Y-direction is parallel to the compressive loading axis to remain consistent with the Dugdale analysis. Using the extended isotropic solution developed by Konish and Whitney,[39] the stress concentration factors (SCF) were computed for each laminate, and they are also included in Table III. As expected, the SCF for the quasi-isotropic laminates of HST-7 and F155 was 3, while it was slightly higher (3.335) for the orthotropic PEEK laminate.

The average compression modulus measured for each material system is listed in Table IV. The PEEK and HST-7 compressive moduli are the average of 2 tests while the F155 modulus is the average of 3 tests. Typical stress-strain data for each material system is plotted in Figs. 15, 16, and 17. The compressive modulus for each system was computed using the average from the two gages in the initial linear portion of the curve. Because of the obvious bending in these specimens at higher loads, the ultimate compression strength was not calculated. The bending observed in these preliminary tests indicated the need for the MTS to be axially aligned during each set-up for compression tests. Part of the bending was attributed to initial warp within the specimens prior to loading. Additionally, close observation of Fig. 17 shows an unloading portion (indicated by arrows) of the stress-strain curves in an HST-7 specimen. This phenomenon was observed in both HST-7 modulus tests. These specimens did not break within the unsupported gage length.

TABLE III. LAMINATE ENGINEERING CONSTANTS.

MATERIAL	E_x, GPa	E_y, GPa	G_{xy}, GPa	ν_{xy}	SCF
AS4/PEEK	29.0	62.3	17.4	0.244	3.335
T2C145/F155	47.8	47.7	18.3	0.304	3.000
IM6/HST-7	53.0	53.0	20.1	0.321	3.000

TABLE IV. LAMINATE MATERIAL PROPERTIES.

MATERIAL	E_{cy}, GPa†	E_{cy}, GPa††	G_{Ic}, J/m²	ν_{cxy}
AS4/PEEK	30.1	43.8	2663	0.257
T2C145/FIS5	36.5	35.2	468	0.311
IM6/HST-7	47.9	---	397	0.312

† COMPRESSION TEST

†† BENDING TEST.

Fig. 15 Typical stress-strain modulus data for an unnotched PEEK specimen.

AS4/PEEK

Moclulus Data

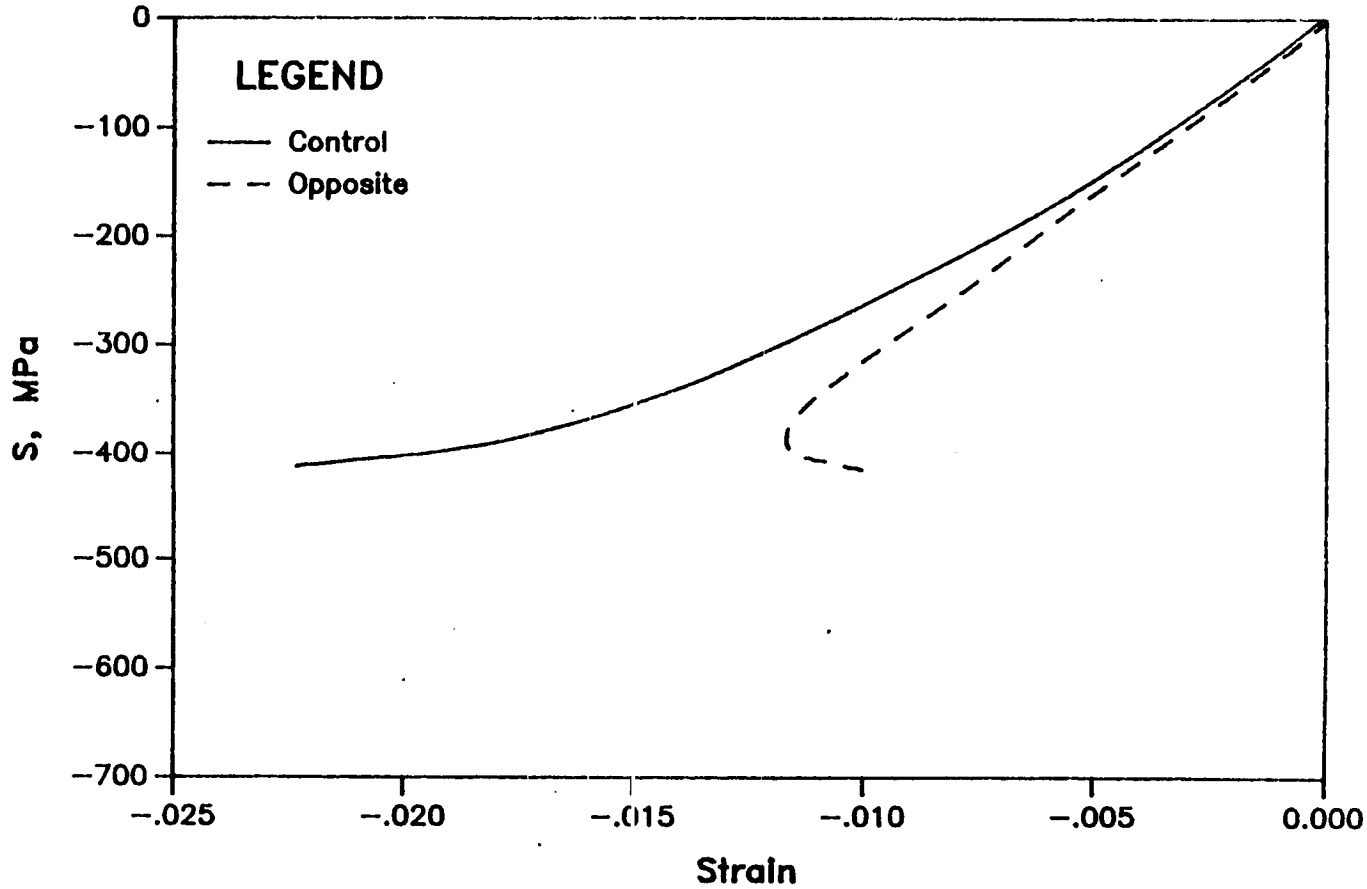

Fig. 16 Typical stress-strain modulus data for an unnotched F155 specimen.

T2C145/F155

Modulus Data

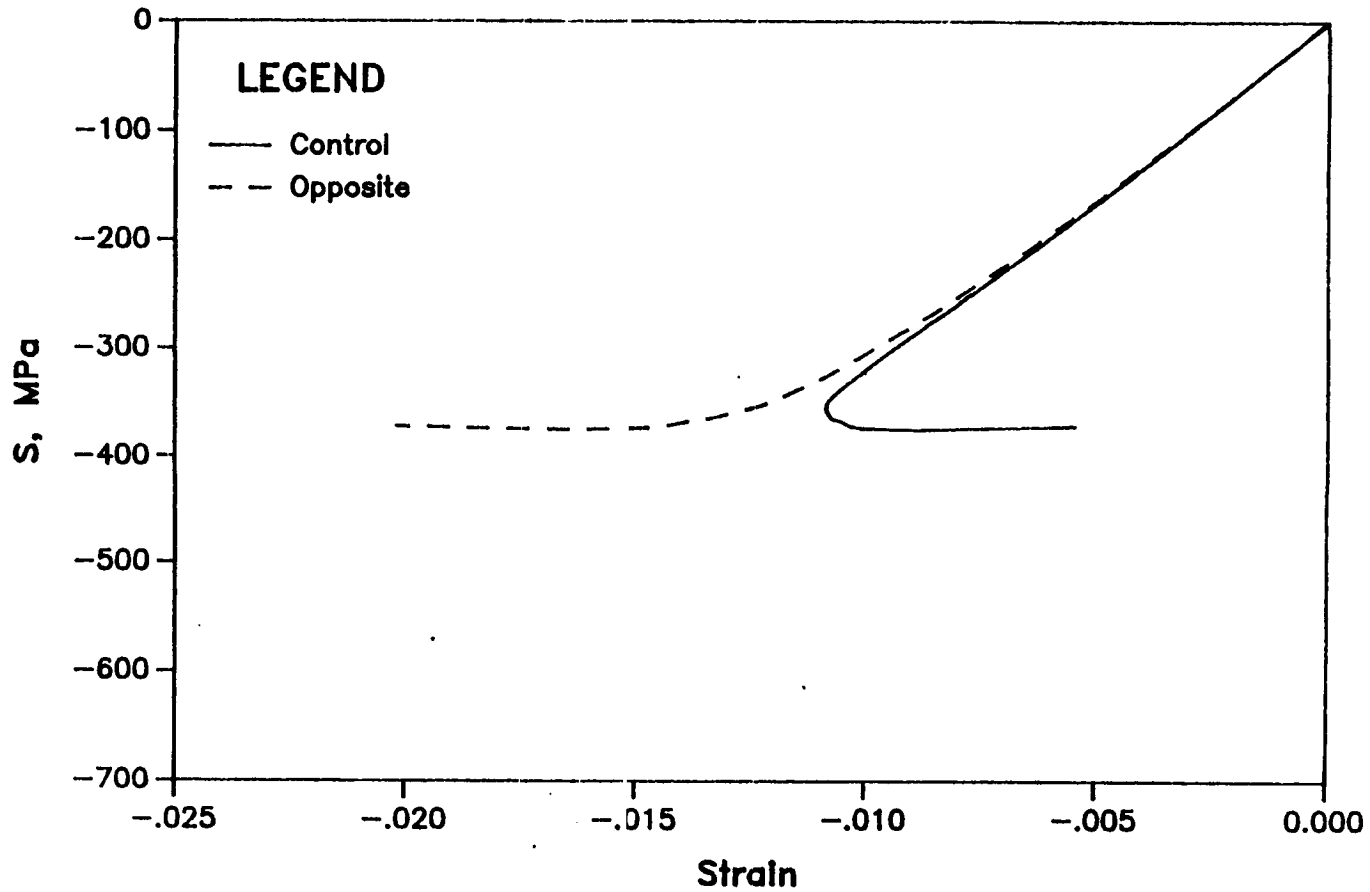

Fig. 17 Typical stress-strain modulus data for an unnotched HST-7 specimen.

IM6/HST-7

Modulus Data

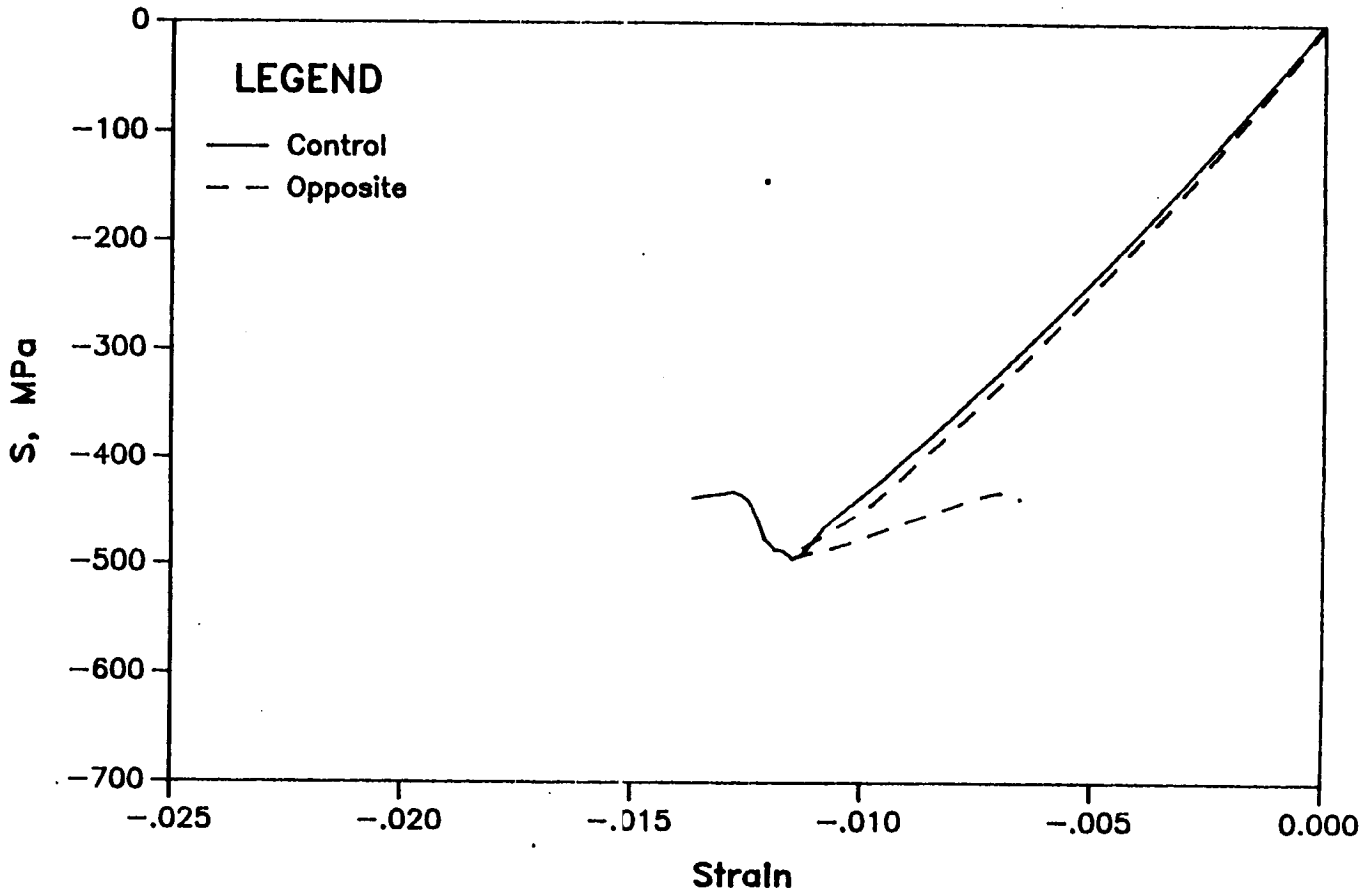

Post-mortem examination of this specimen showed that the unloading was due to a shear crippling failure within the lower grip.

Figure 18 shows the shear crippling zone in SEM micrographs from a longitudinal section cut from the gripped end of one of the HST-7 modulus tests. Figure 18a shows the shear crippling zone in the 0° and +45°, respectively labeled on the figure, plies (9^{th} and 10^{th} plies from the surface). Notice the rotating of the fibers in many directions, regardless of the support provided by the grip. The box in Fig. 18a is enlarged in Fig. 18b to show the rotated and broken (tensile type breaks) 0° fibers within the shear crippling zone.

The stiffness was also computed from the three-point bend test. These stiffnesses are also reported in Table IV. For the PEEK and F155 material systems, these stiffnesses agree quite well with those measured from the compression tests. A stiffness is not reported for the HST-7 system because the loading pins damaged the specimen, and thus, the test did not provide an accurate measurement of the stiffness.

Comparison of the measured longitudinal compressive modulus, E_{cy}, with the predicted tensile modulus, E_y, indicates that the PEEK and F155 panels may not have been of the quality one would expect. It is not unreasonable to expect the compressive modulus to be lower than the tensile moduli because of factors such as fiber waviness and possible specimen warpage. Recall that some of the bending evident in the stress-strain data in Fig. 15 was attributed to specimen warp. The F155 measured compressive modulus was within 24% of the predicted tensile modulus which seems fairly reasonable; the HST-7 compressive modulus was within 10% of the predicted tensile modulus which is certainly good agreement. The measured ν_{cxy} was within 5% of the predicted ν_{xy} for each material system, a very

Fig. 18 Shear crippling zone within gripped end of an HST-7 specimen
a) Overview of damage zone in 0° and +45° plies.
b) Magnified shear crippling damage in 0° fibers.

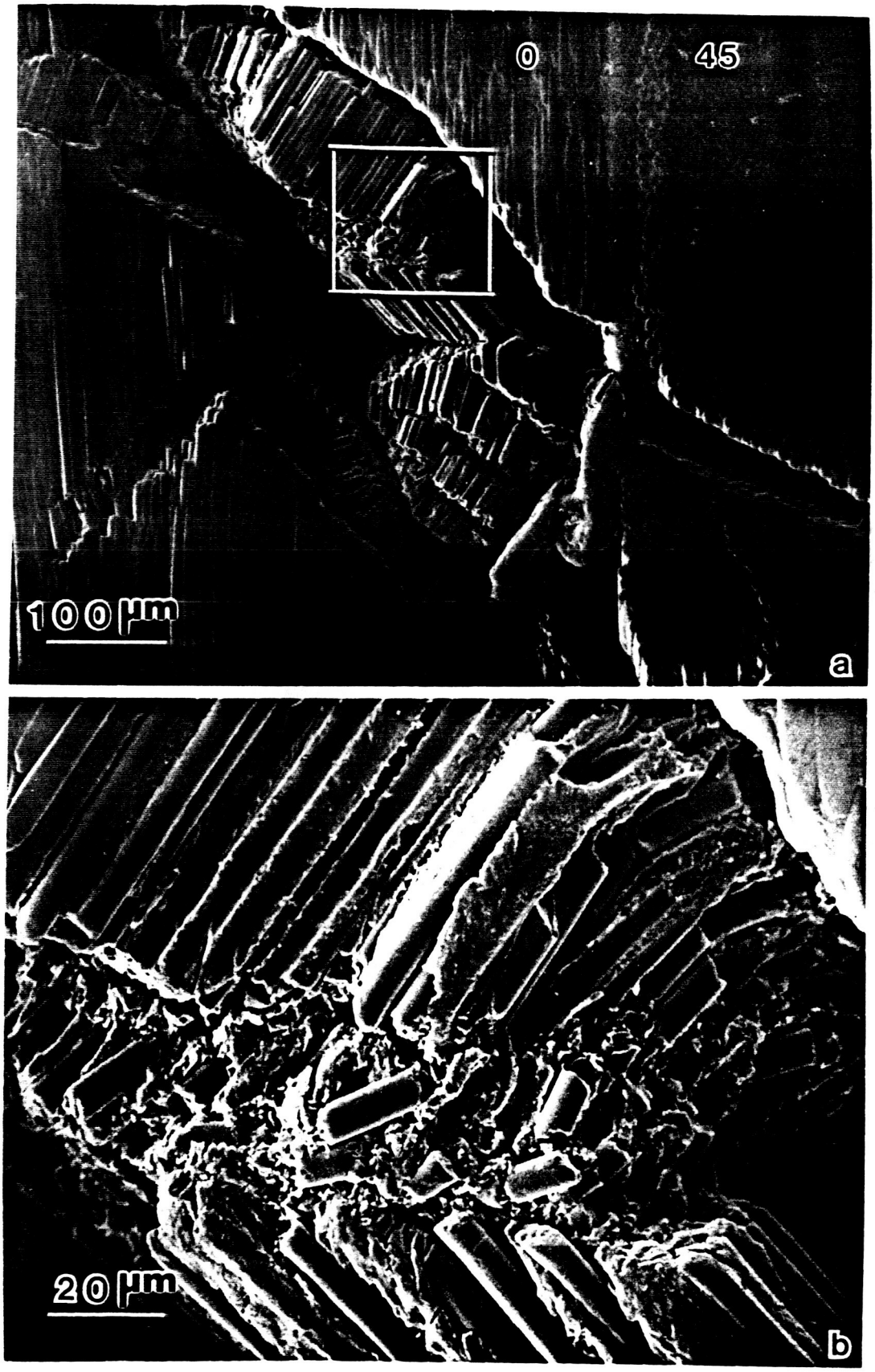

good correlation.

Typical load-displacement curves for the F155 and HST-7 mode I DCB tests are presented in Figs. 19 and 20, respectively. These two plots indicate that both materials behaved linearly-elastic and exhibited stable delamination crack growth. G_{Ic} was computed for each specimen using the 4 methods described in Chapter III of this thesis. Although all methods computed G_{Ic} within 15% of each other. Table IV includes only G_{Ic} from the most accurate of these methods, the area method. As is common, the unload compliance method generated the lowest numbers. Excluding the unload compliance method from the percent difference calculations, the G_{Ic}'s computed were within 5% of each other. G_{Ic} (468 J/m^2) for the F155 system was computed from the average of 2 tests, and G_{Ic} (397 J/m^2) for the HST-7 system was computed from the average of 3 tests. Micrographs of the Mode I DCB fracture surfaces corresponding to the load-displacement data in Figs. 19 and 20 are shown in Figs. 21 (F155 system) and 22 (HST-7 system), respectively. In each of these figures the direction of crack propagation is from the top of the page to the bottom of the page. The severely deformed region on the left side of Fig. 22a (marked with an arrow) is the deformed interleaf. The lack of deformed interleaf over the entire fracture surface indicates that the delamination grew principally at the prepreg/interleaf interface. Similar results for a number of interleafed materials were presented by Masters.[43] Figures 21b and 22b show the bare fibers (obvious fiber sizing grooves) and fibers covered in matrix; both cases appear to be random across the surface as is typical of most Mode I DCB fracture surfaces. G_{Ic} (2663 J/m^2) for a similar PEEK system was obtained from other Mode I testing by Elizabeth Chakachery (Dissertation research) at Texas A&M University. However, these DCB specimens were 40-ply unidirectionals with $\pm 5^\circ$ plies at the midplane to deter fiber

Fig. 19 Typical load-displacement data for an F155 composite DCB specimen.

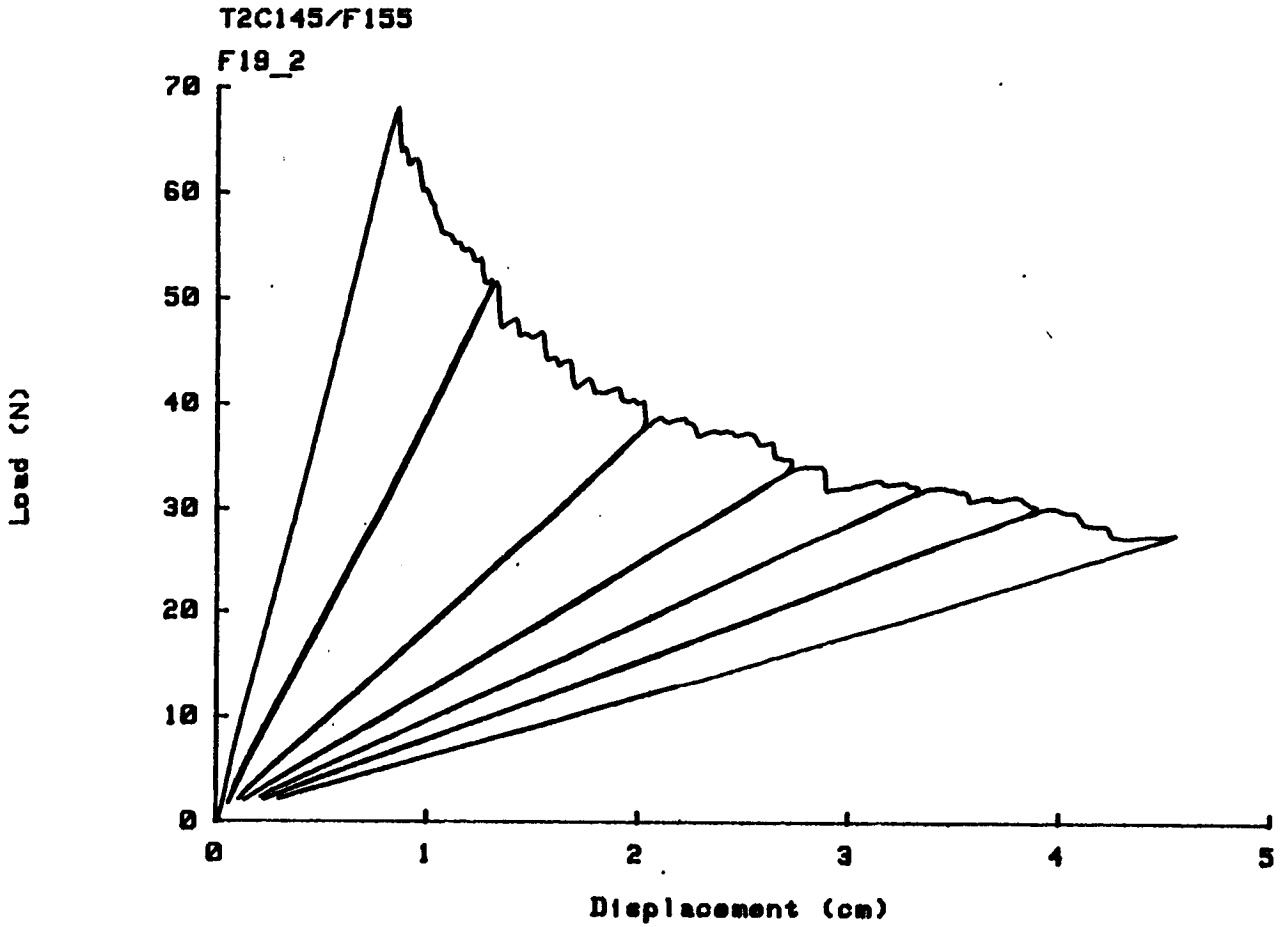
T2C145/F155
F19_2
70
60
50
40
30
20
10
0
Load (N)
0
1
2
3
4
5
Displacement (cm)

Fig. 20 Typical load-displacement data for an HST-7 composite DCB specimen.

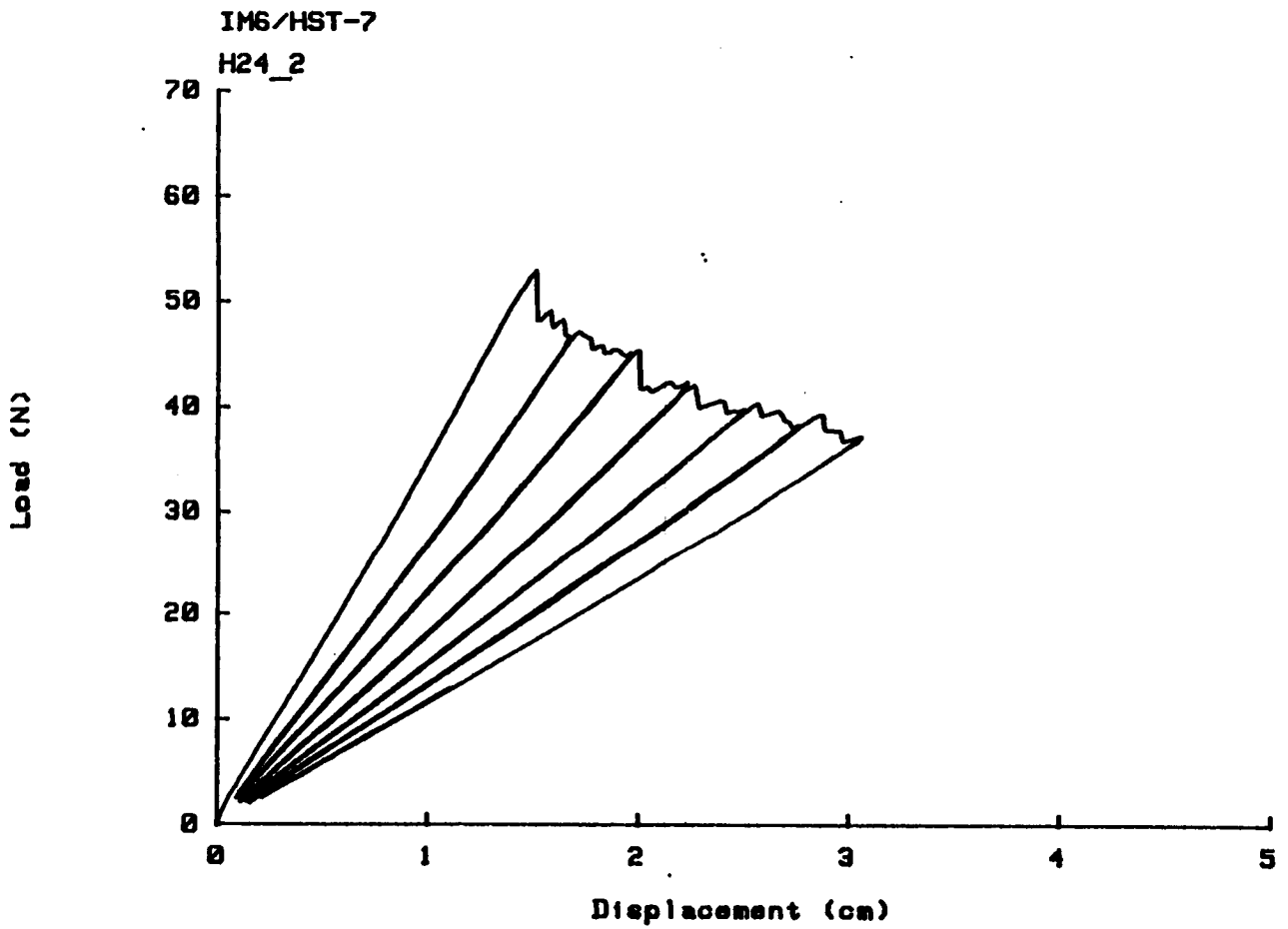
IM6/HST-7
H24_2
70
60
50
40
30
20
10
0
Load (N)
0
1
2
3
4
5
Displacement (cm)

Fig. 21 Micrographs of F155 Mode I DCB fracture surfaces.
a) Overview of fracture surface.
b) Fiber/matrix interface.

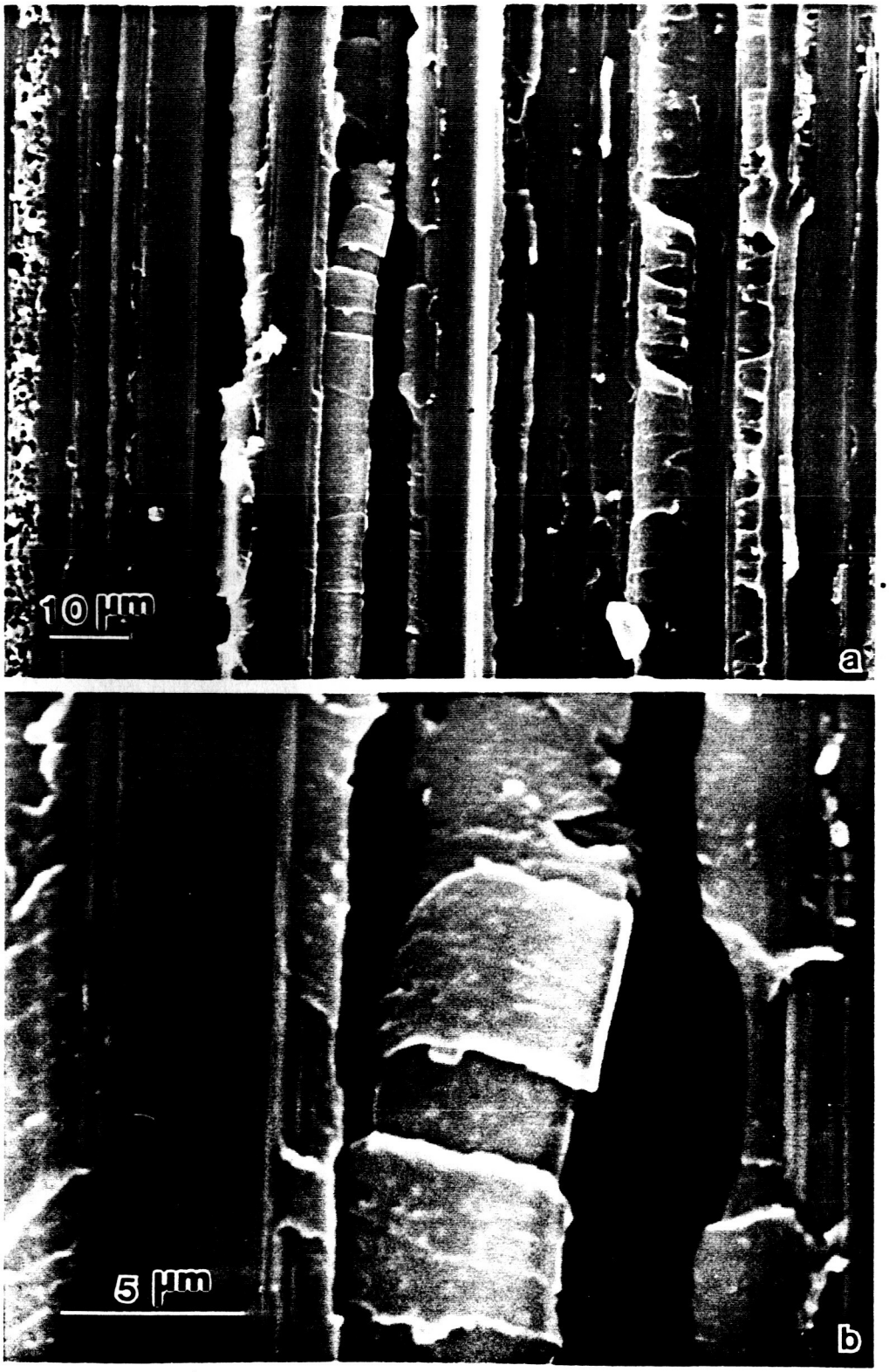

Fig. 22 Micrographs of HST-7 Mode I DCB fracture surfaces.
a) Overview of fracture surface.
b) Fiber/matrix interface.

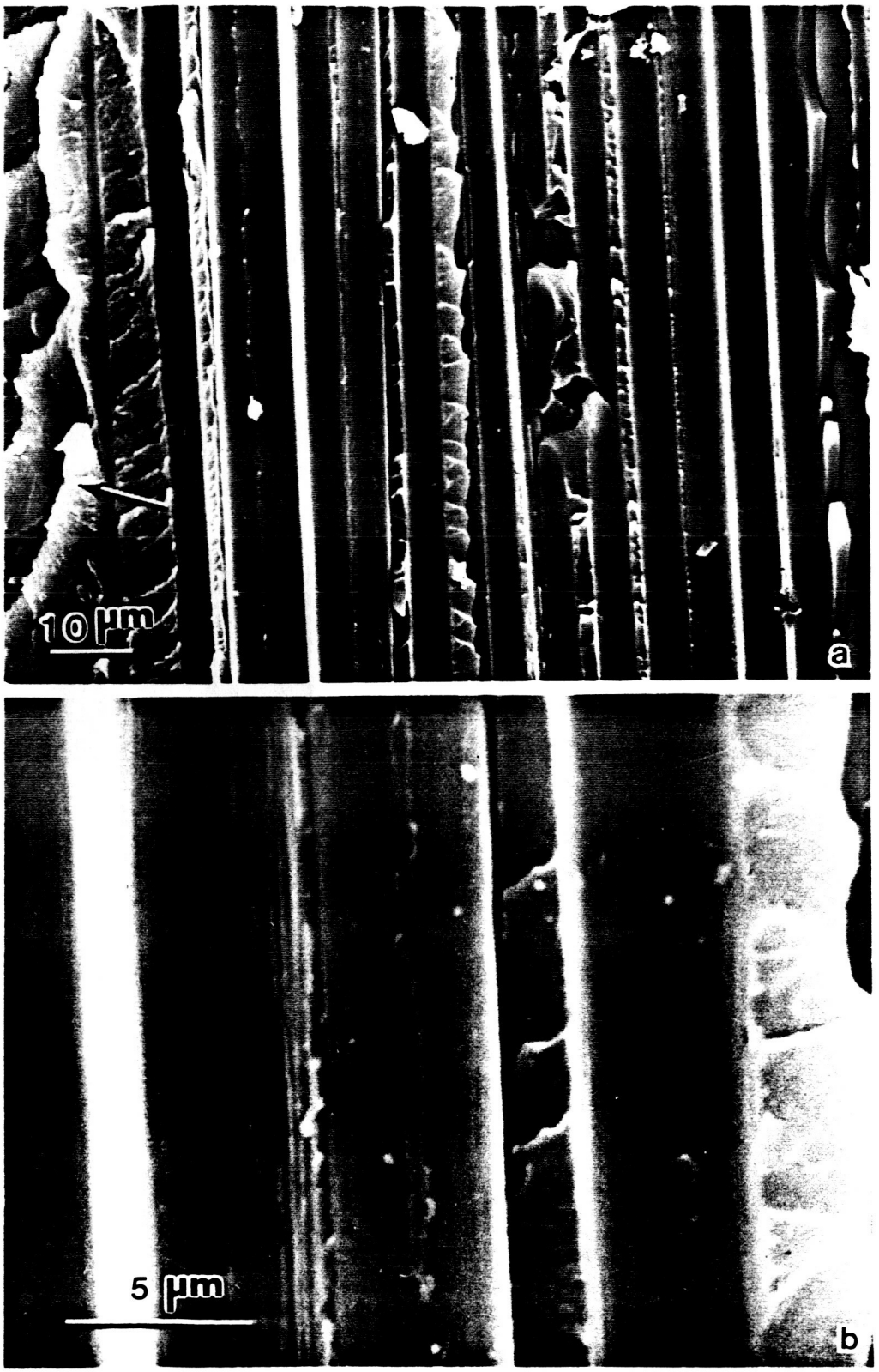

bridging and a teflon starter crack.

The representative microstructures (perpendicular to the 0° fiber direction) are shown in Figs. 23, 24, and 25 for the PEEK, F155, and HST-7 systems respectively. Figures 23a, 24a, and 25a each show two 0° plies between two other plies, including resin rich regions at the ply interfaces and the particularly thick ply interface of the interleafed HST-7 material in Fig. 25a. The ply directions are marked at the left edge of each figure. Figures 23b, 24b, and 25b show the relative fiber volume fraction within the 0° ply of each material system. The fiber volume fraction within the 0° ply shown for each system is approximately the same for the PEEK and F155 systems while the HST-7 fiber volume fraction is slightly higher. However, the fiber volume fraction averaged over the resin rich region between plies (including the interleaf material) is somewhat lower than the other systems. Notice that the HST-7 fiber diameter is approximately 25% smaller than the 0° fibers in the PEEK and F155 systems.

Compression Test Methods

Initially, the open hole composite specimens were loaded in compression under displacement control at a relatively slow rate of 0.0025 cm/min to provide more stable growth of the shear crippling zone. However, in the majority of these tests, the shear crippling zone did not grow as stably as similar specimens observed by Guynn and Elber in preliminary testing (previously described in Chapter I). The major difference between these two series of tests is that the NASA specimens were loaded in load control and the thesis specimens were loaded in displacement control. During load control testing, load is induced into the specimen at a constant load rate, and thus, the energy in the system is always increasing. However, in displacement

Fig. 23 Representative microstructure of PEEK material system.
a) Ply cross-section (perpendicular to 0° fiber direction).
b) Fiber volume fraction within 0° ply.

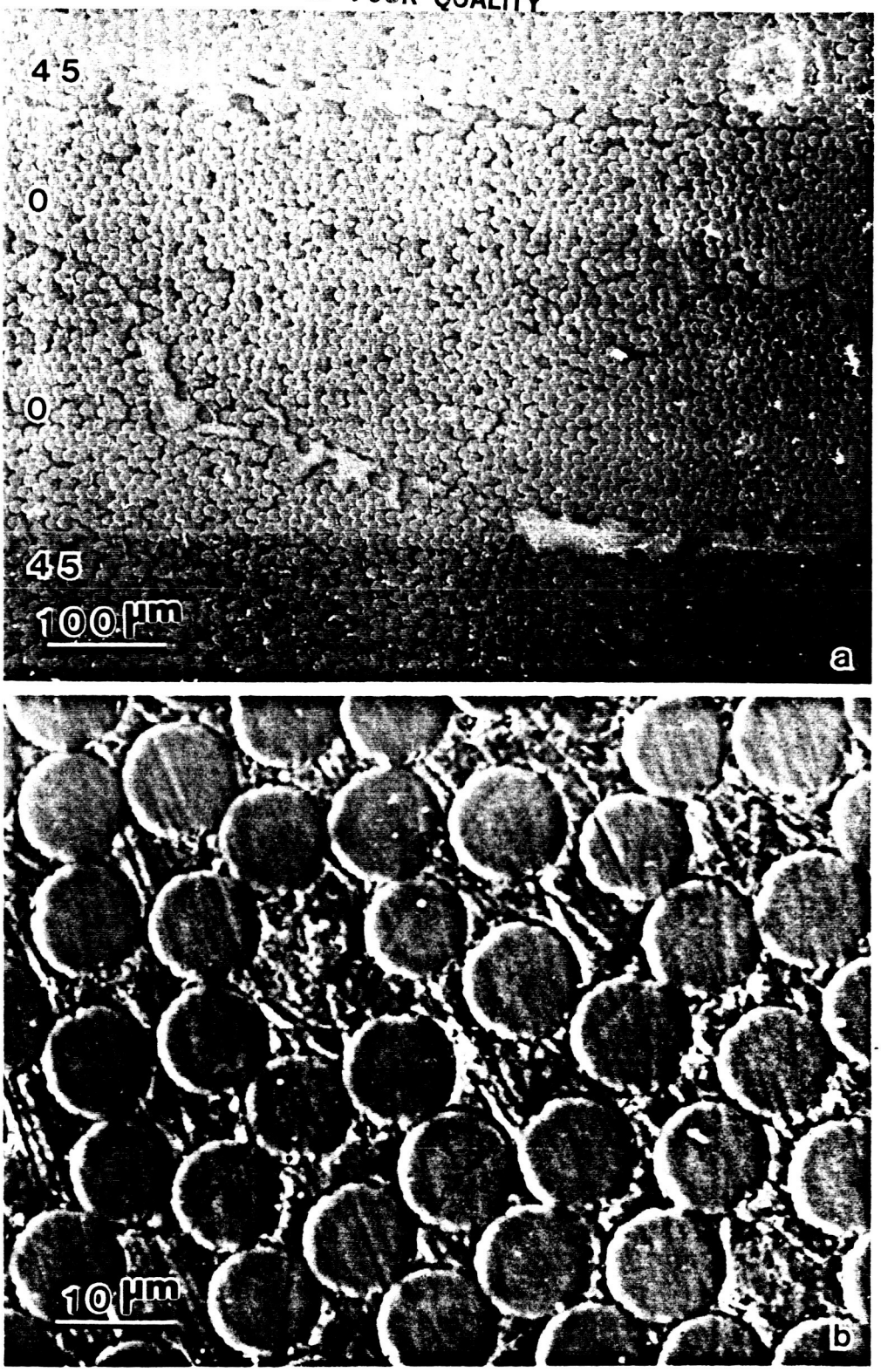

Fig. 24 Representative microstructure of F155 material system.
a) Ply cross-section (perpendicular to 0° fiber direction).
b) Fiber volume fraction within 0° ply.

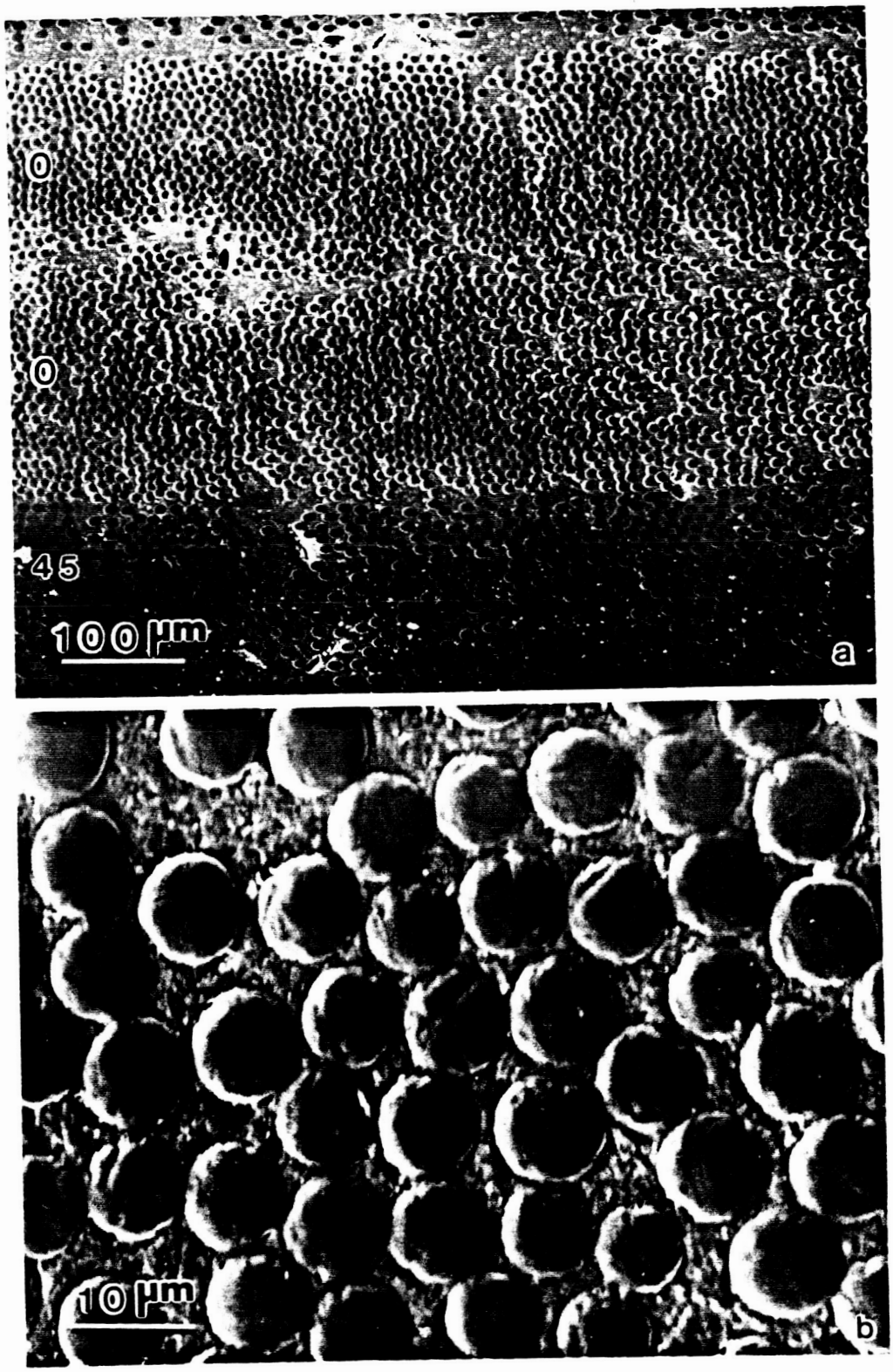

Fig. 25 Representative microstructure of HST-7 material system.
a) Ply cross-section (perpendicular to 0° fiber direction).
b) Fiber volume fraction within 0° ply.

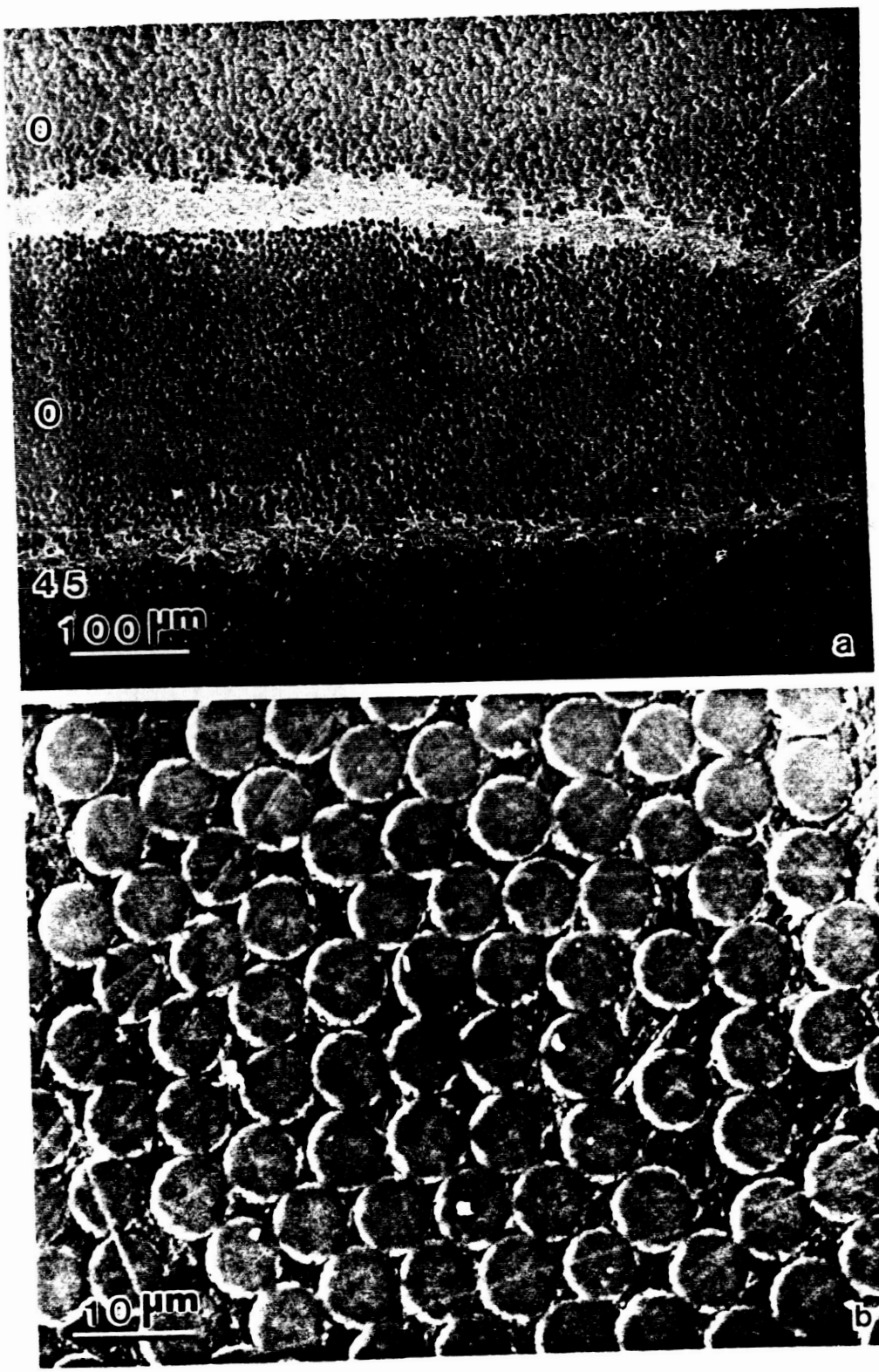

control, the induced load is a response to a known applied displacement. The energy in a displacement controlled system increases until the crack (shear crippling zone in this case) grows. Crack growth absorbs energy from the system, and thus, the load on the system is reduced. Based on these premises, it is obvious that displacement control is inherently more stable than load control testing. After a number of investigations of the MTS and its controllers, it was determined that the load input per function generator step in displacement control was approximately 50 times the load input per function generator step in load control. Additionally, it was determined that the load input per function generator step in strain gage control would be on the order of the same size load step as in load control. Consequently, strain gage control was chosen for these tests. Strain gage control has the added advantage that the controlling gage was placed on the more compressive surface (determined by preloading) of the specimen.

Because of the obvious bending observed in the compression modulus tests (reported previously in Figs. 15–17), the axial alignment of the system was verified prior to each session of compression tests in the MTS. Typical stress-strain data for the two longitudinal strain gages from one of the precision steel specimens are plotted in Fig. 26. The fact that these two curves are almost perfectly superposed over each other indicates that the MTS aligment is excellent and certainly adequate.

Macroscopic Compression Behavior

The average open hole compression strengths measured for the two materials and three hole sizes tested are listed in Table V. It should be noted that only one data point was available for the F155 specimens containing 0.64 cm holes. Figure 27 shows a typical load-displacement curve for these open hole compression loaded

Fig. 26 Typical stress-strain data for a precision steel specimen in the MTS alignment verification studies.

4140 STEEL

Alignment Tests

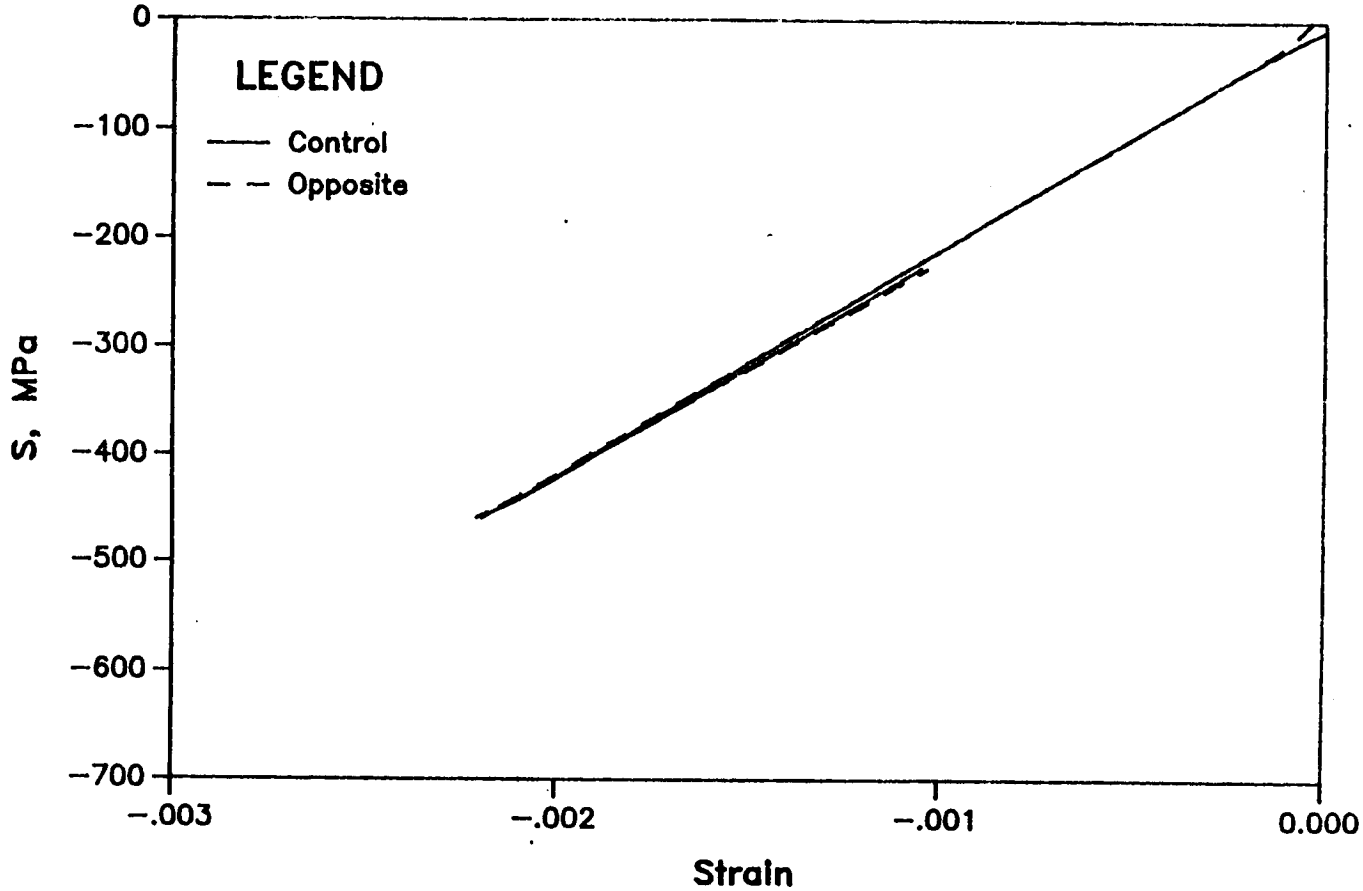

TABLE V. OPEN HOLE COMPRESSION STRENGTHS FOR THREE HOLE DIAMETERS.

	Compression Strength, MPa		
	0.64 cm	0.32 cm	0.16 cm
AS4/PEEK	355.7	422.6	495.0
TC145/F155	297.1*	311.6	387.4
IM6/HST-7	-----	321.3	332.3*

*Indicates only one data point available.

Fig. 27 Typical load-displacement data for open hole, compression loaded composites, loaded until damage zone formation. This data is from an AS4/PEEK specimen containing a 0.16 cm diameter hole.

AS4/PEEK

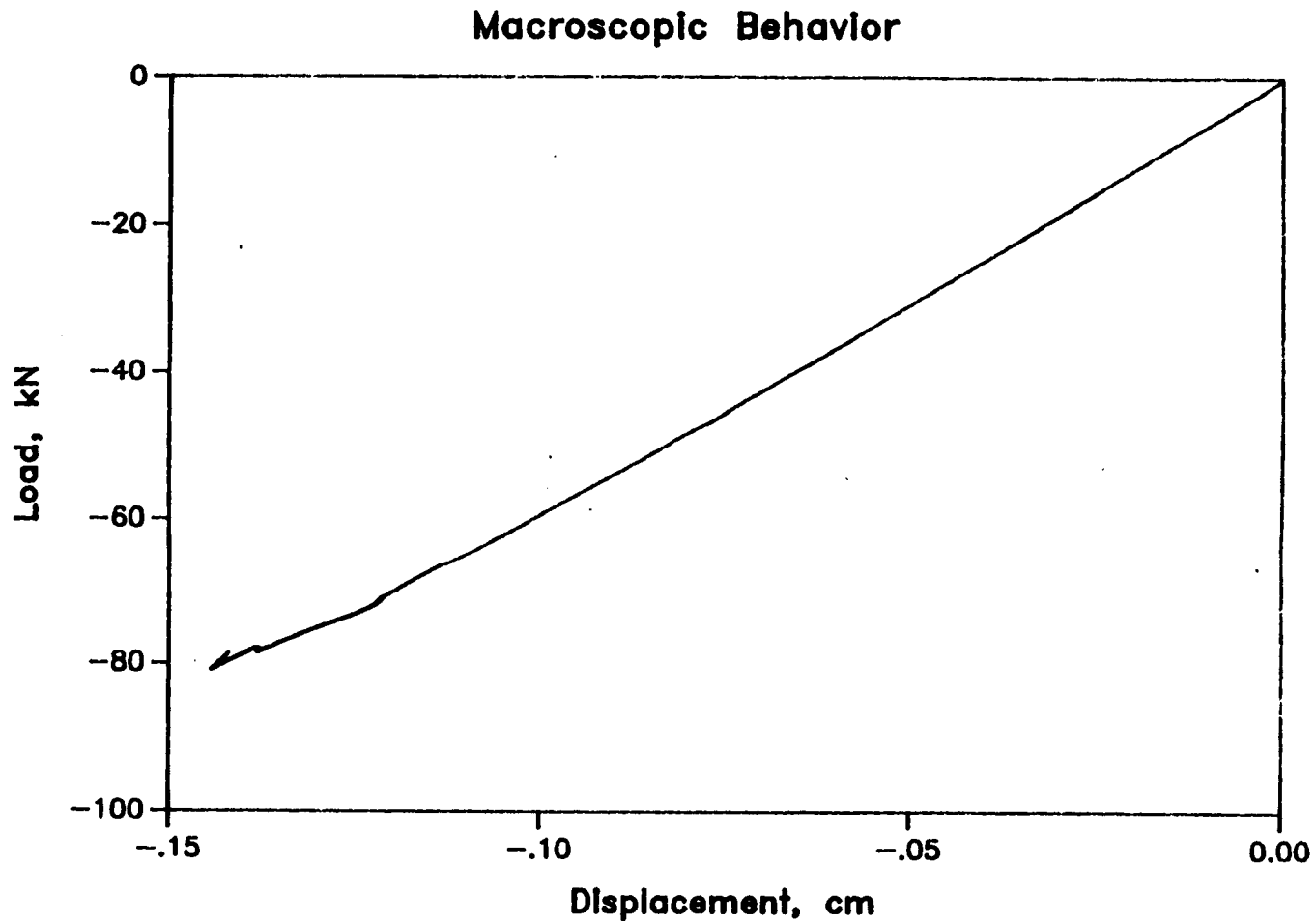
Macroscopic Behavior
0
-20
-40
-60
-80
-100
Load, kN
-.15
-.10
-.05
0.00
Displacement, cm

specimens. This particular curve is for a PEEK specimen containing a 0.16 cm hole, one of the specimens chosen for the sectioning study. Specifically, the nonlinearity of this load-displacement curve should be noted. Figure 28 shows an enlarged view of the more nonlinear and unloading portion of the curve. This part of the curve is associated with visible damage initiation (labeled "pop-in" on Fig. 28) and unloads due to stable damage zone development. This specimen was unloaded prior to catastrophic failure for additional studies of the shear crippling zone. The shear crippling zone for this specimen is shown in Fig. 12a.

Comparison of Analytical and Experimental Results

Using eq. 13 and as a parameter, arbitrarily assigning values to σ_{oc} for crush zone stress, theoretical curves of S vs. ρ were generated, as shown in Figs. 29 and 30. Experimental data (S vs. ρ) from 2 tests (one from each of the PEEK and F155 material systems) have been plotted along with analytical curves in Figs. 29 and 30. Fig. 31 shows the progressive growth of the crush zone from initiation to failure in each of these tests. Both samples contain a 0.32 cm diameter hole. It should be noted that the observed S vs. ρ relationship is much flatter than the predicted relationships, independent of the chosen crush zone stress, σ_{oc}, used in the analysis. Because of the obvious lack of agreement between the theoretical curves and the experimental data, shown in Figs. 29 and 30, this data was not plotted for the HST-7 specimens.

Nondestructive Examination

Figure 32a shows the visible surface damage in a F155 specimen containing a 0.16 cm diameter hole. This specimen was loaded to 84% of the average open

Fig. 28 Enlarged view of nonlinear portion of load-displacement data presented in Fig. 27.

AS4/PEEK

Damage Zone Formation

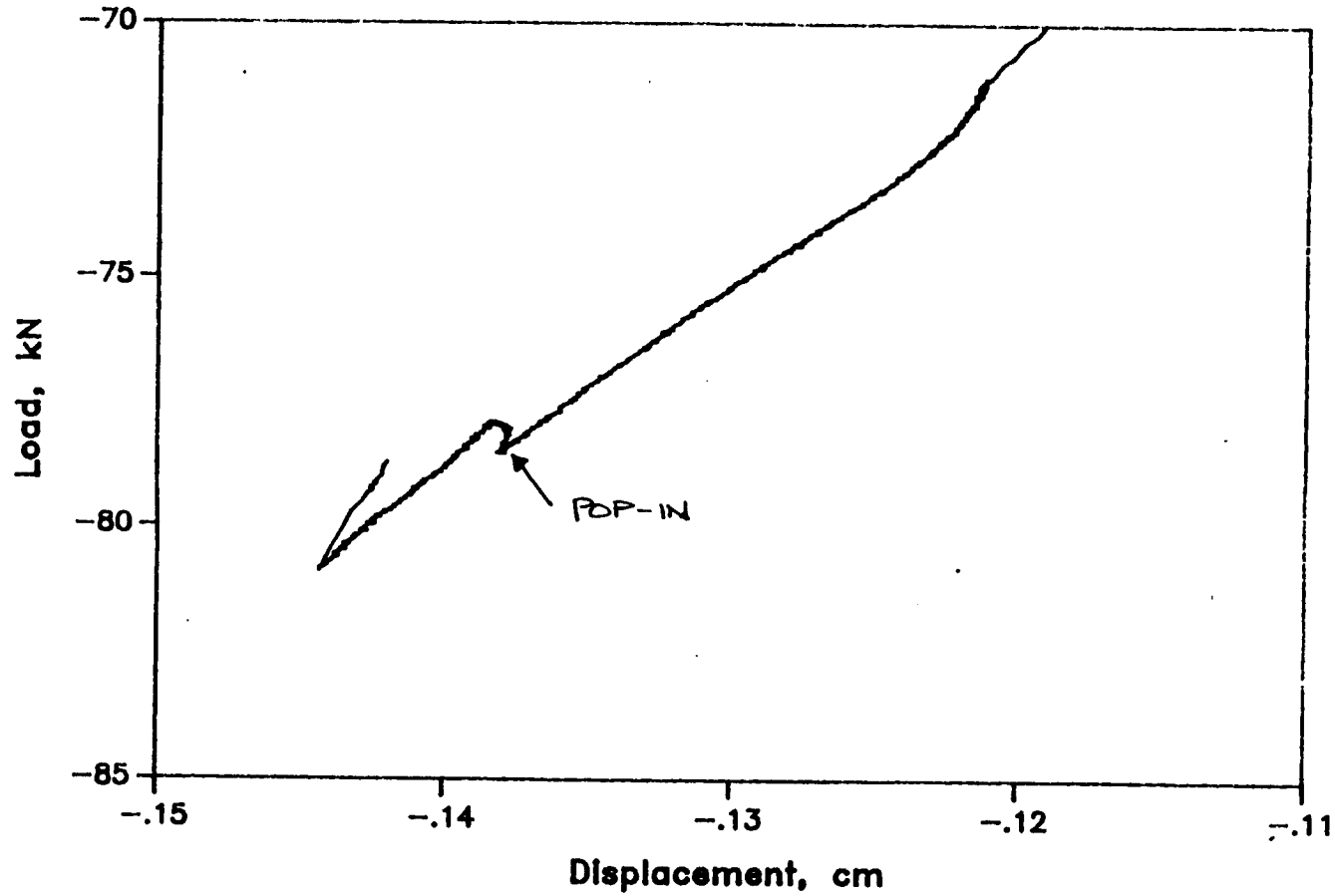

Fig. 29 Applied compressive stress vs. crush zone size for 0.32 cm diameter hole in a PEEK specimen.

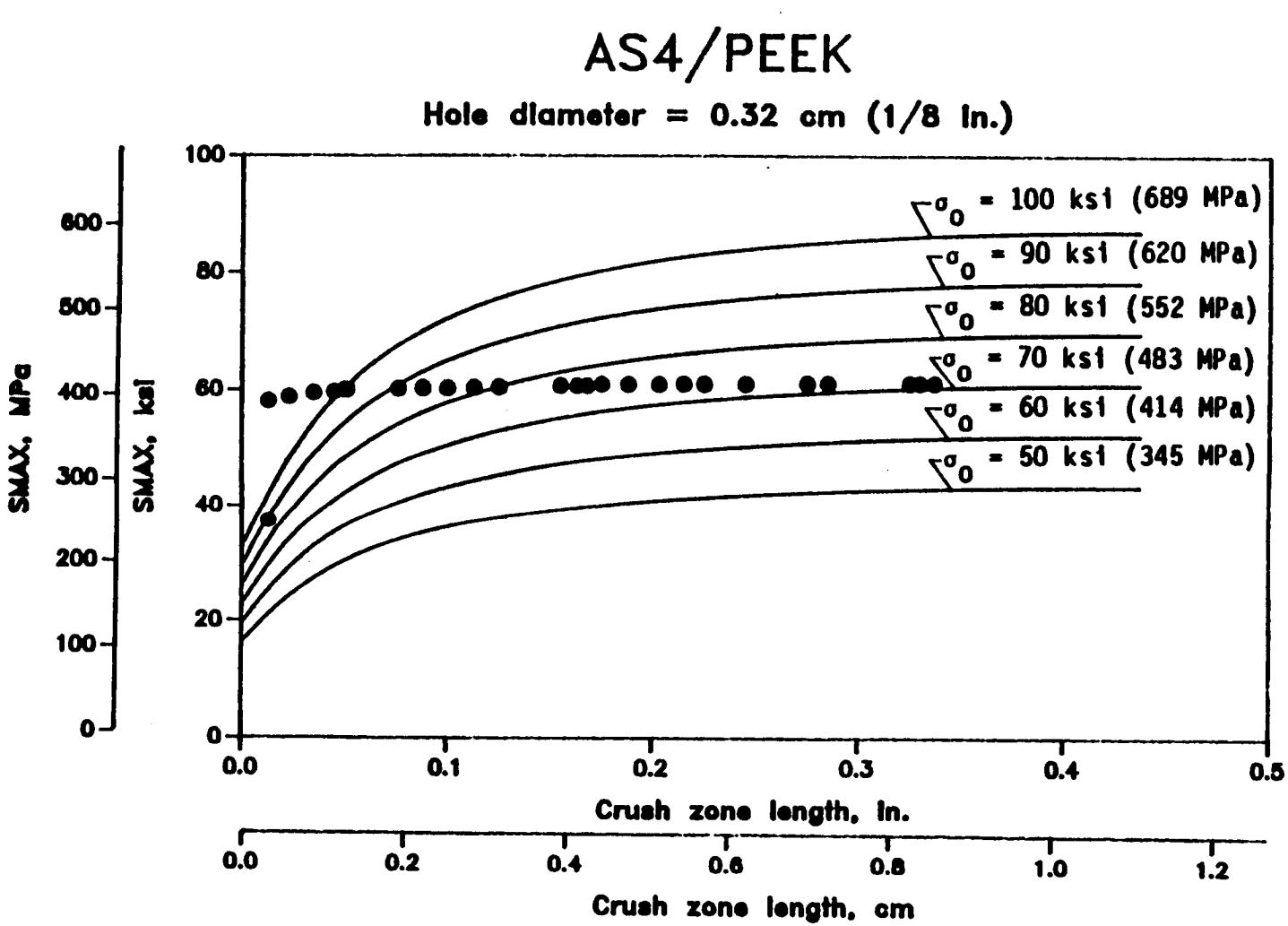
AS4/PEEK
Hole diameter = 0.32 cm (1/8 in.)
SMAX, MPa
SMAX, ksi
σ_0 = 100 ksi (689 MPa)
σ_0 = 90 ksi (620 MPa)
σ_0 = 80 ksi (552 MPa)
σ_0 = 70 ksi (483 MPa)
σ_0 = 60 ksi (414 MPa)
σ_0 = 50 ksi (345 MPa)
Crush zone length, in.
Crush zone length, cm

Fig. 30 Applied compressive stress vs. crush zone size for 0.32 cm diameter hole in an F155 specimen.

T2C145/F155

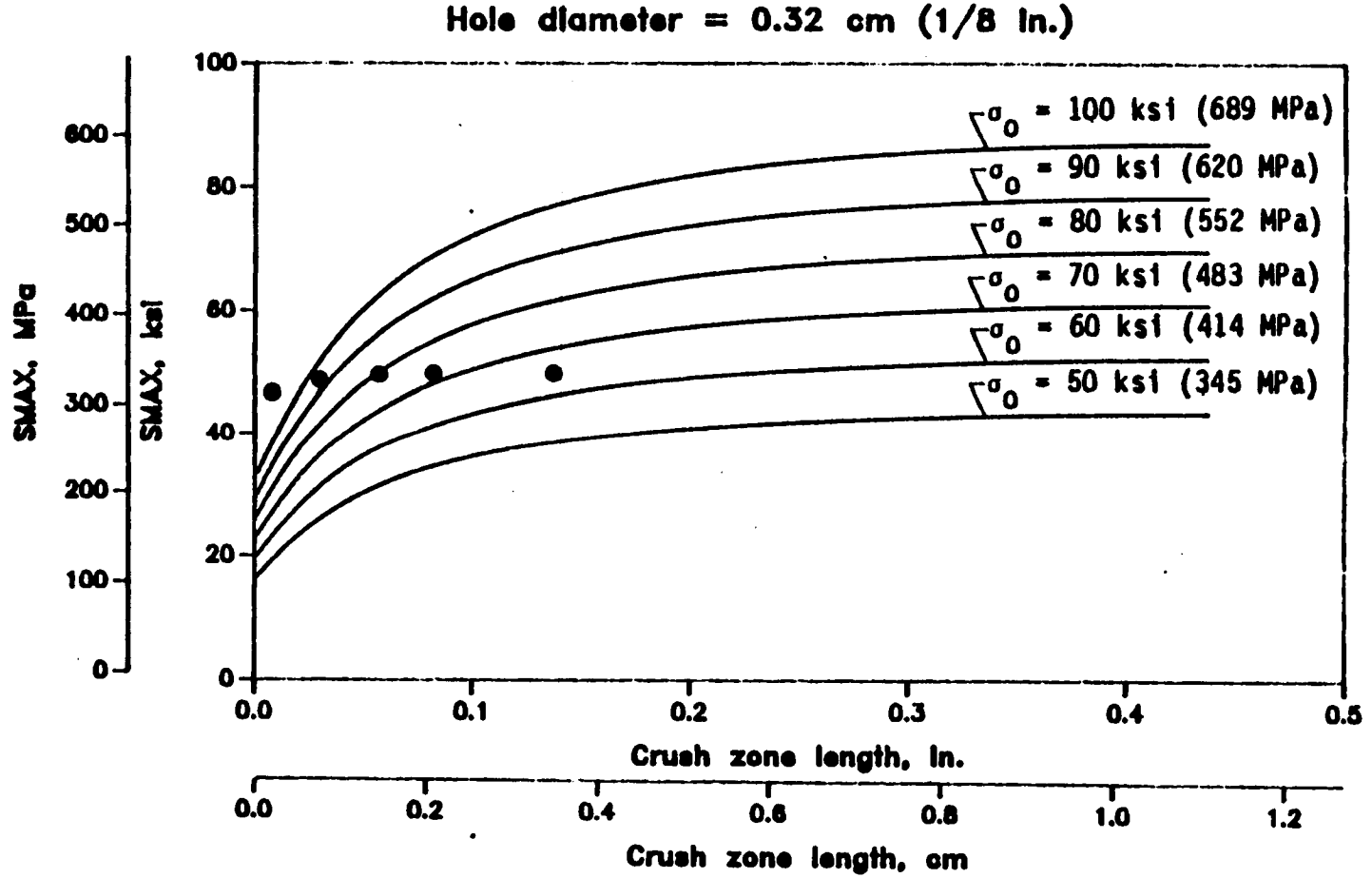
Hole diameter = 0.32 cm (1/8 in.)
SMAX, MPa
SMAX, ksi
600
500
400
300
200
100
0
100
80
60
40
20
0
σ_0 = 100 ksi (689 MPa)
σ_0 = 90 ksi (620 MPa)
σ_0 = 80 ksi (552 MPa)
σ_0 = 70 ksi (483 MPa)
σ_0 = 60 ksi (414 MPa)
σ_0 = 50 ksi (345 MPa)
0.0
0.1
0.2
0.3
0.4
0.5
Crush zone length, in.
0.0
0.2
0.4
0.6
0.8
1.0
1.2
Crush zone length, cm

Fig. 31 Initiation and propagation of the damage zone prior to catastrophic failure.
a) AS4/PEEK specimen.
b) T2C145/F155 specimen.

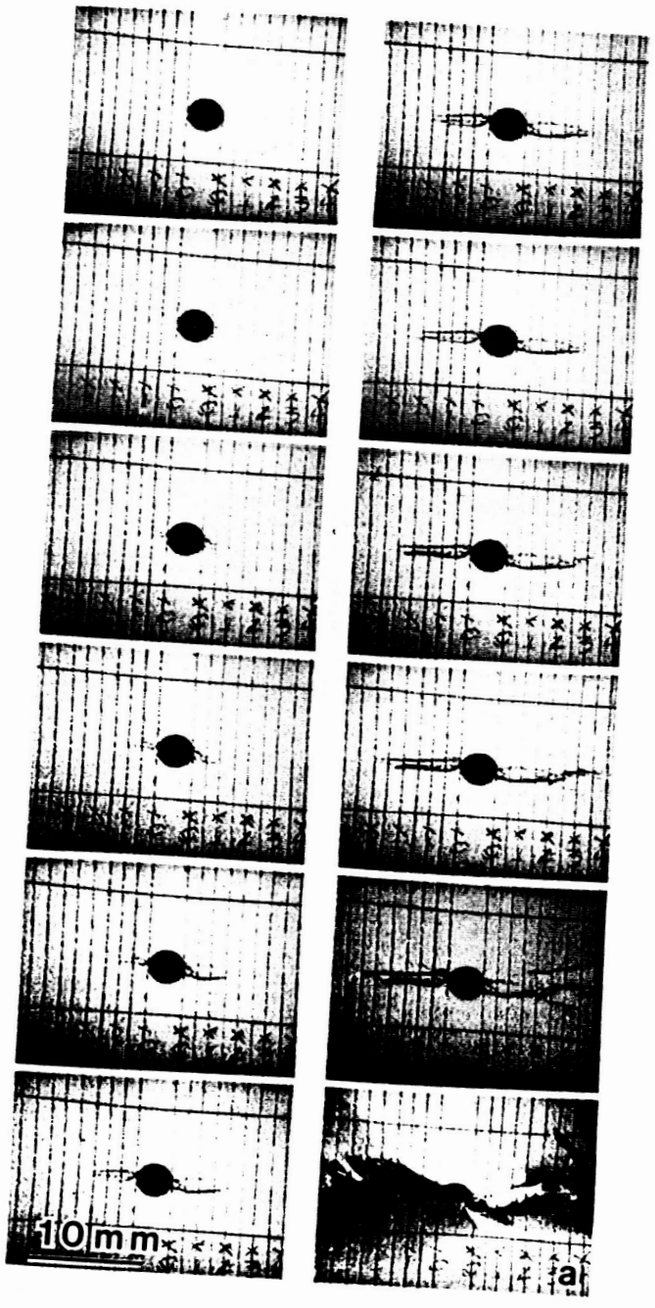

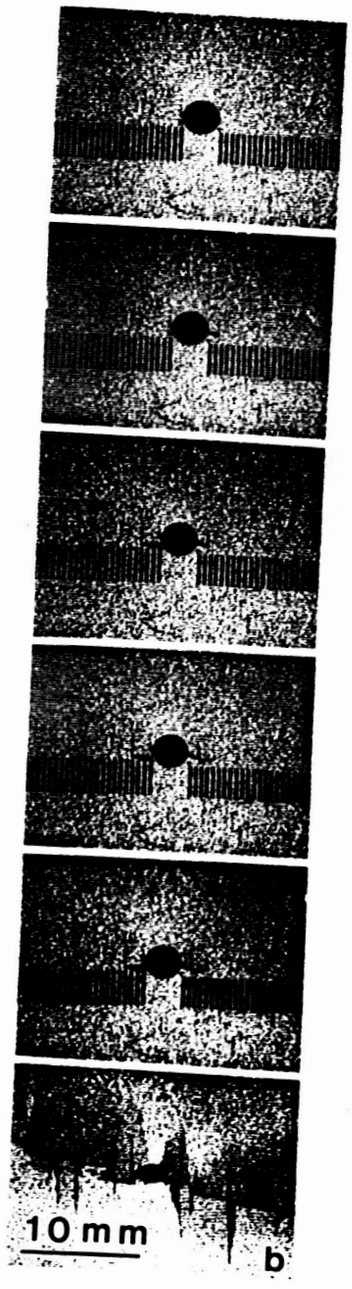

Fig. 32 NDE of a damage zone in a T2C145/F155 specimen containing a 0.16 cm diameter hole.
a) Photograph.
b) Ultrasonic C-scan.
c) Enhanced X-ray.

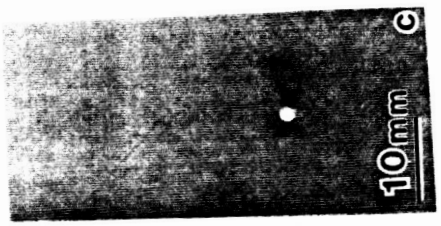

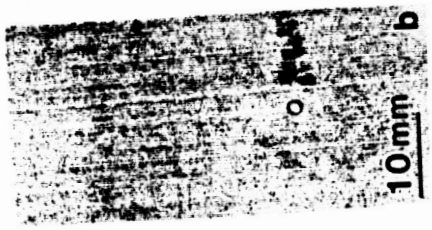

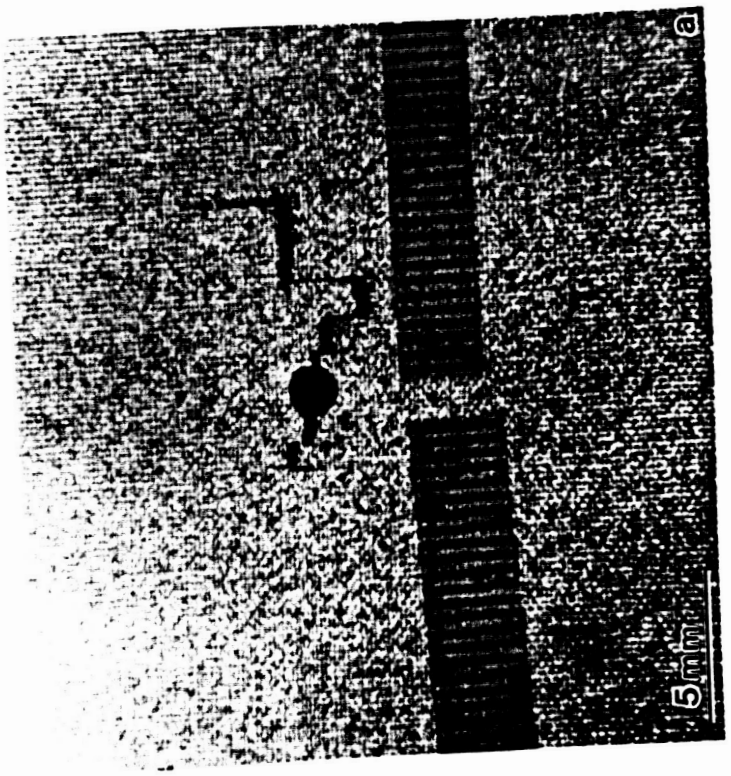

hole compression strength for this particular hole size and material (see Table V for details). This photograph indicates the presence of a large shear crippling zone. However, the C-scan (Fig. 32b) and X-ray (Fig. 32c) both indicate that no resolvable delamination is present within the laminate and also that the visible surface damage is significantly larger than the interior damage. Thus, the NDE is implying that the only damage is buckling of surface 0° fibers.

The X-rays of the PEEK and HST-7 specimens shown in Figs. 12a and 12b, are shown in Figs. 33a and 33b, respectively. The PEEK specien was loaded to 102% of the PEEK average open hole compression strength, and the HST-7 specimen was loaded to 101% of the HST-7 average open hole compression strength (refer to Table V for details). These X-rays further indicate the crack-like appearance of the shear crippling zone. They also indicate the lack of resolvable delamination and significantly larger visible surface than interior damage. The NDE presented in Figs. 32 and 33 is representative of that observed in all specimens examined.

Load Transmission Through the Damage Zone

Two specimens (each containing a 0.16 cm hole) have been selected to demonstrate the reduction in load transmitted once the shear crippling zone has formed. Refer to Fig. 9b to recall the strain gage configuration ($2r$, just above the shear crippling zones) for these specimens. The first specimen is the PEEK specimen shown in Figs. 12a, 27, 28, and 33a. This specimen was loaded until the shear crippling zone formed (shown in Fig. 12a). Figure 34 is a plot of the local stress supported by the material underneath each of the three gages, Control, L1, and L2 gages as a function of the remotely applied compressive stress, S, during the initial loading until the shear crippling zone formed. The L1 gage reads an artificially

Fig. 33 NDE X-rays of damage zones in specimens containing 0.16 cm diameter holes.
a) AS4/PEEK specimen.
b) IM6/HST-7 specimen.

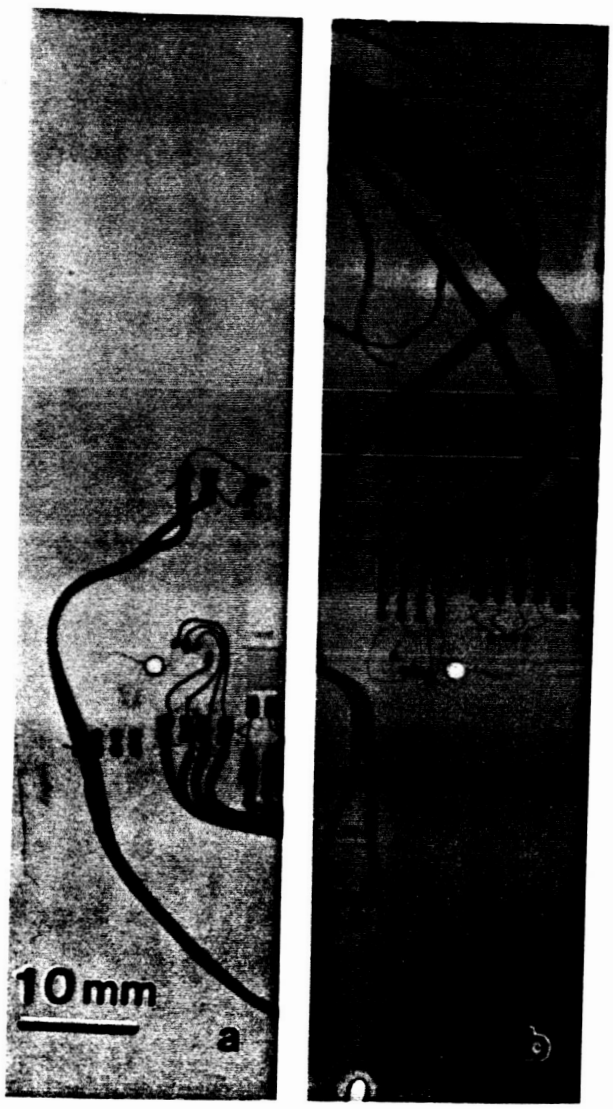

Fig. 34 Local stress-applied stress data for the Control, L1, and L2 strain gages for a PEEK specimen loaded to damage zone formation.

AS4/PEEK

Damage Zone Formation

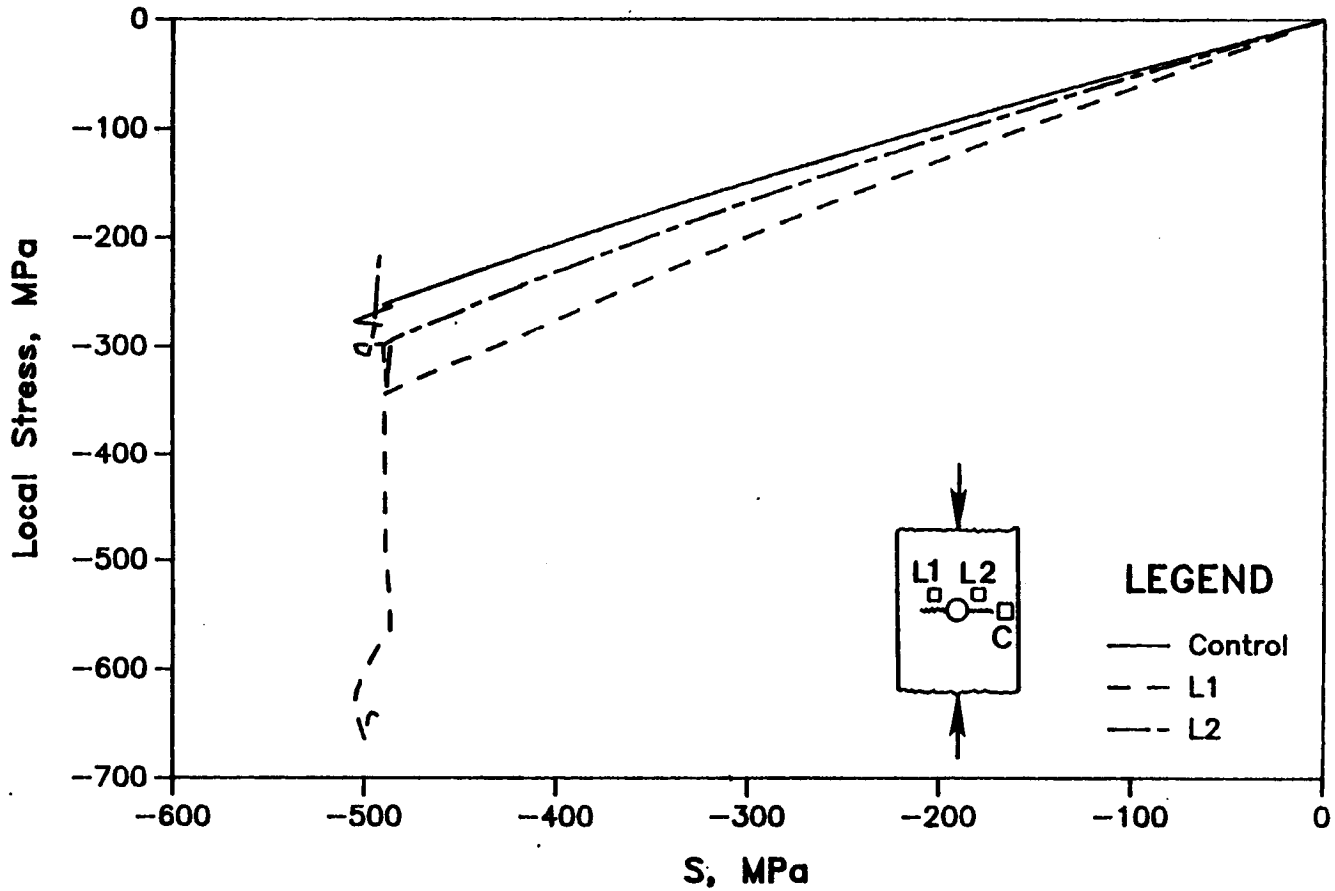

higher stress level because the damage zone grew directly underneath the L1 gage, and thus, the gage recorded artificially high strains. The L2 gage gives a slightly higher local stress that the control gage because it is located at the edge of the strain gradient ($< 2r$) surrounding the hole. Figure 35 shows the reload/unload data for this same specimen after shear crippling and after the L1 gage was moved from its position on top of the damage zone to a new location just above the damage zone. In this case, it is obvious that the local stress supported in the shear crippled zone is lower (by about 10%) than the nominal applied compressive stress measured at the control gage in a remote location (see Fig. 35).

The second specimen presented is the HST-7 specimen shown in Figs. 12b, 12c, and 33b. This specimen was loaded until the shear crippling zone shown in Fig. 12b formed. Figure 36 is a plot showing the strains measured in the control, L1, and L2 gages as a function of time during the initial loading until the shear crippling zone formed. Again, the L1 and L2 gages are reading higher strains than the control gage, and these higher readings are attributed to the L1 and L2 gages located in the strain gradient surrounding the hole. The L2 gage records a sharp reduction in the strain level when the shear crippling zone formed below this gage, as shown in Fig. 12b. The local stress supported by the material underneath each of the control, L1, and L2 gages for this same damage zone formation is plotted as a function of the applied compressive stress in Fig. 37. In this figure, the significant reduction in the local stress level caused by the crush zone formation is again shown in gage L2. At the same time, the control and L1 gages record an increase in the local stress supported in the undamaged material. The reload/unload data for the same specimen is shown in Fig. 38. The L2 gage indicates that the damaged material supports significantly lower (by 50%) local stress levels than the

Fig. 35 Local stress-applied stress data for the Control and L1 strain gages for a PEEK specimen during reload/unload testing.

AS4/PEEK

Reload/Unload Test

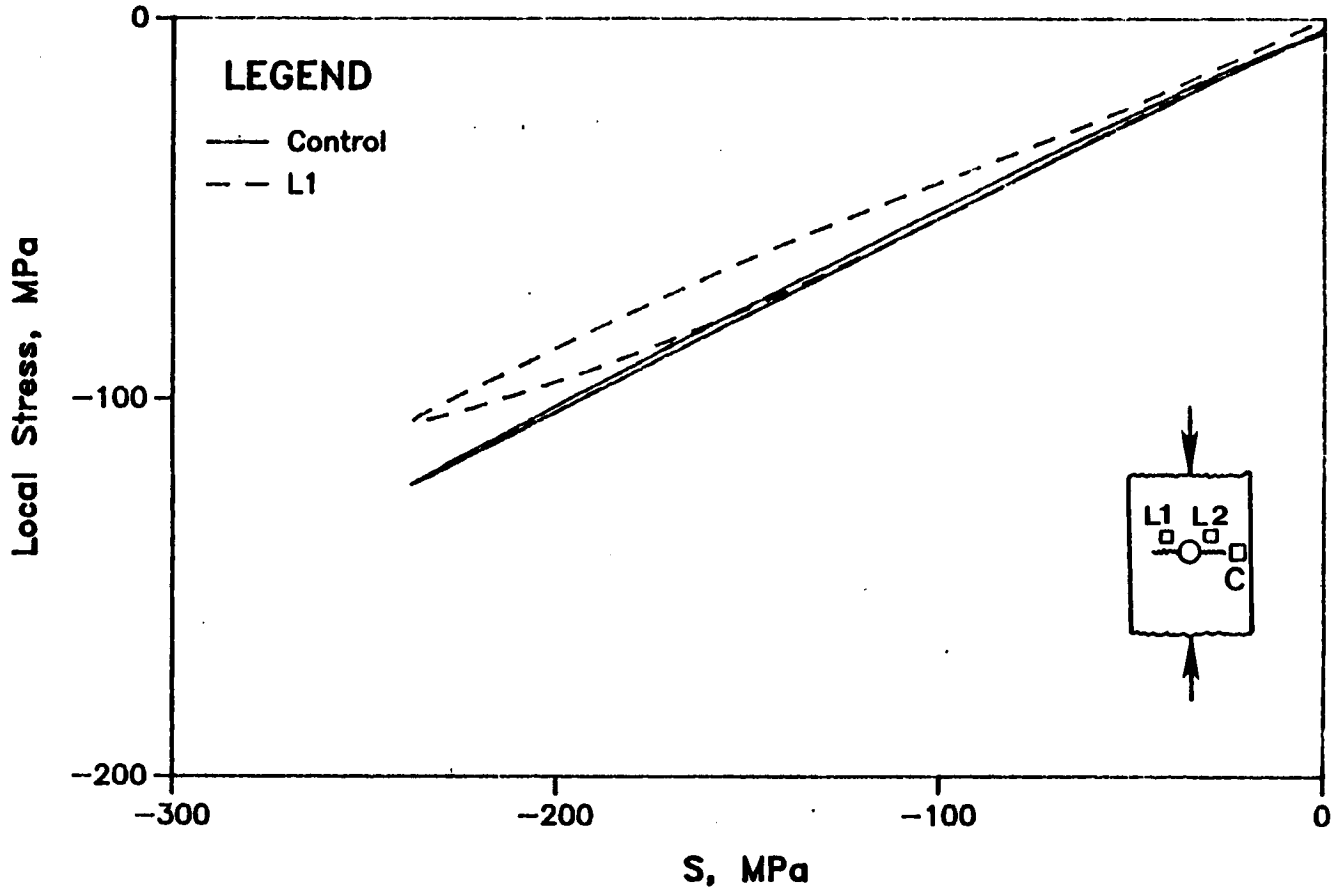

Fig. 36 Strain-time data for Control, L1, and L2 strain gages for an HST-7 specimen loaded to damage zone formation.

IM6/HST-7

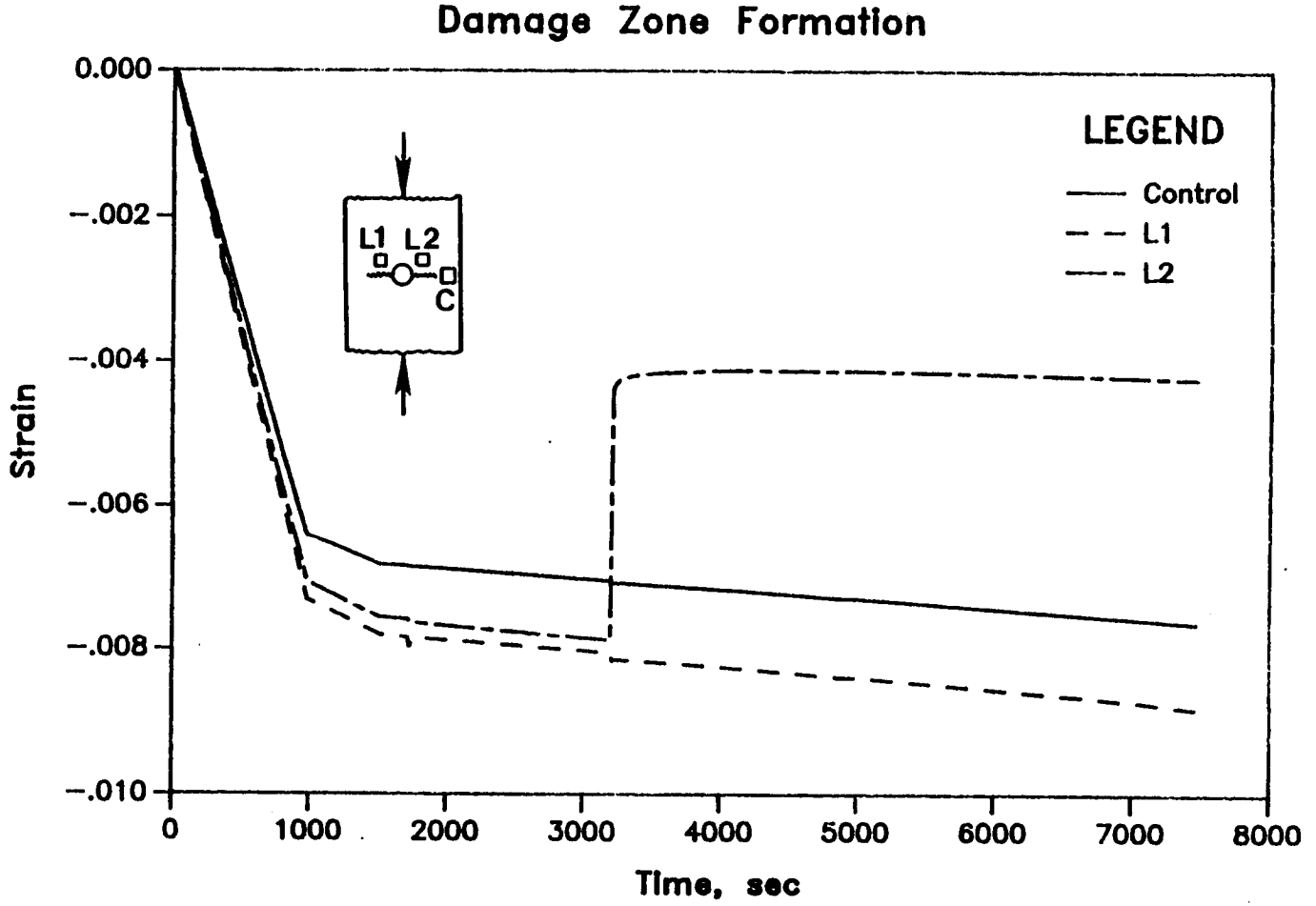
Damage Zone Formation
0.000
-.002
-.004
-.006
-.008
-.010
Strain
0
1000
2000
3000
4000
5000
6000
7000
8000
Time, sec
LEGEND
Control
L1
L2
L1 L2
C

Fig. 37 Local stress-applied stress data for the Control, L1, and L2 strain gages for an HST-7 specimen loaded to damage zone formation.

IM6/HST-7

Damage Zone Formation

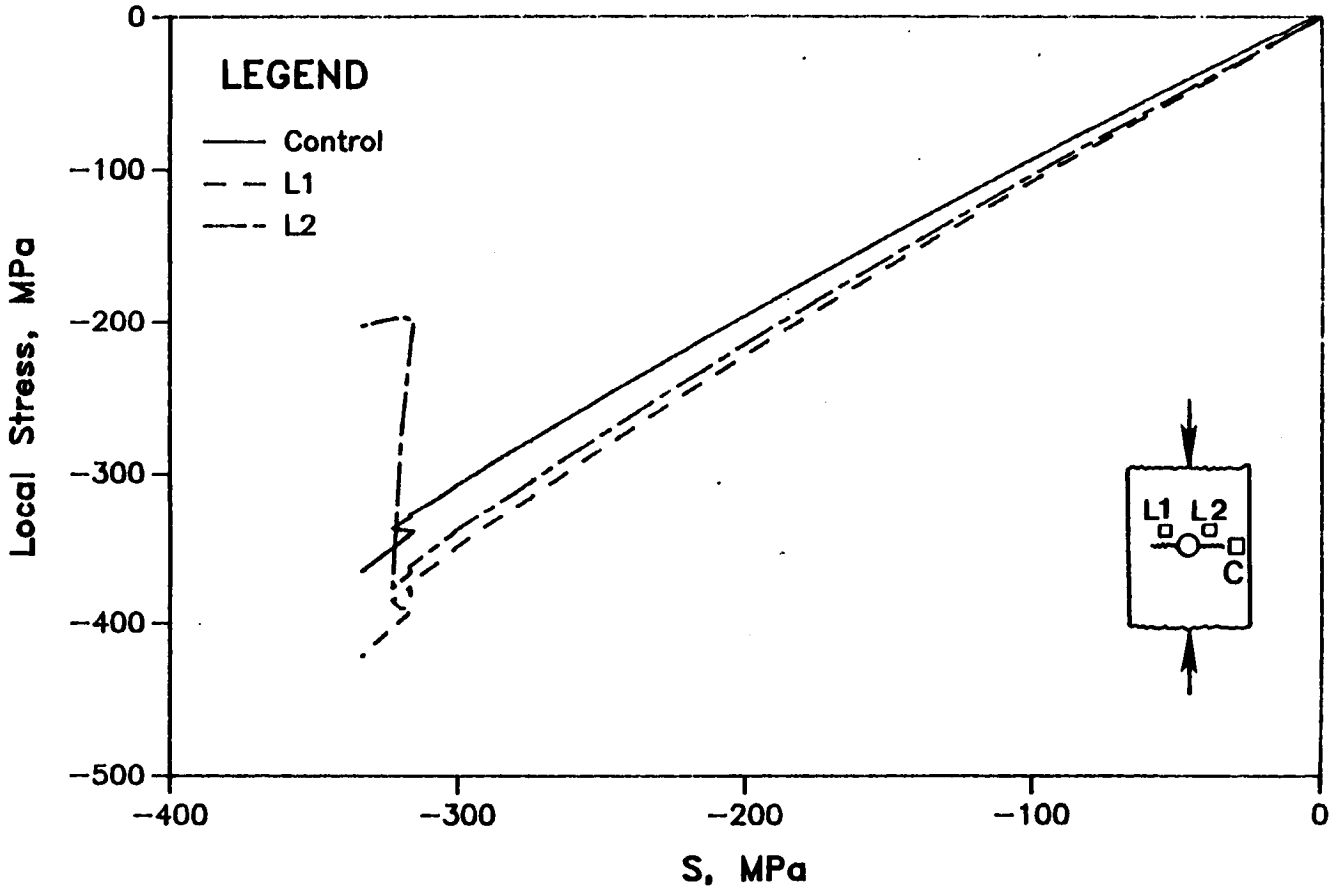

Fig. 38 Local stress-applied stress data for the Control, L1, and L2 strain gages for an HST-7 specimen during reload/unload testing.

IM6/HST-7

Reload/Unload Test

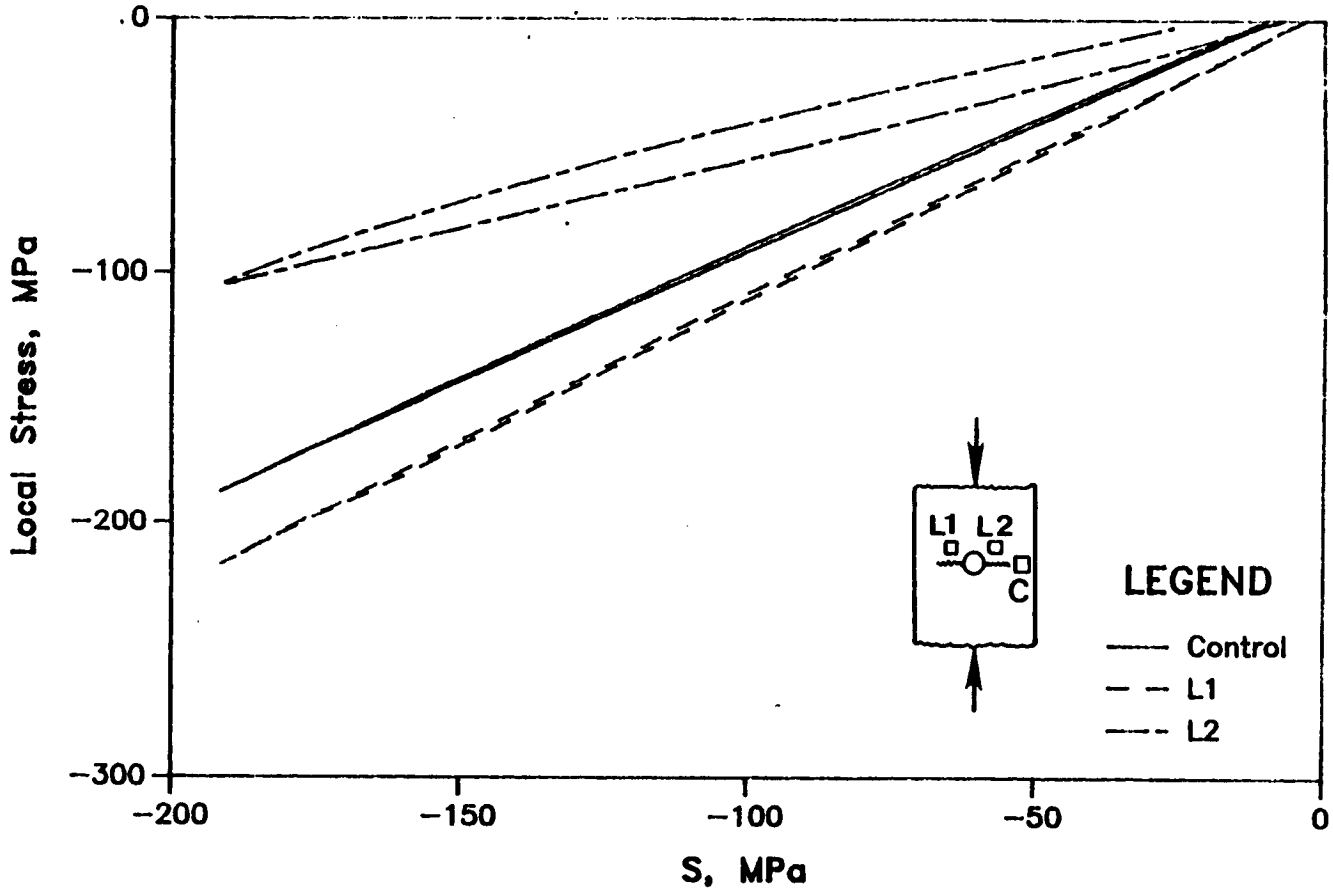

undamaged material for the same applied stress S. The reload-unload data for the same specimen after the damage zone was removed (now slotted) and the gages replaced (see Fig. 12c) is shown in Fig. 39. This data shows that in the absence of the damaged material, the local stress supported at L2 is further reduced to zero.

Sectioning Studies

Three specimens loaded in compression until a shear crippling zone formed were sectioned. Because of the magnitude of work involved in a detailed sectioning investigation, one AS4/PEEK specimen containing a very small shear crippling zone was sectioned to develop systematic sectioning techniques and verify that sectioning provides a viable method for determining the extent of damage through the laminate thickness. In general, the results from this preliminary investigation are not presented in this thesis. However, the most interesting observation in this preliminary investigation was that although the shear crippling zone was small in size, it extended through the thickness of the laminate; every 0° ply (both specimens L and R) was buckled into the hole. The shear crippling zones in the PEEK and HST-7 specimens presented in the previous section of this thesis were sectioned using the systematic techniques developed in the preliminary investigation.

Throughout these sectioning studies, the micrographs are presented with a line scale in its lower left-hand corner and the figure designation in its lower right-hand corner. Because of the variation in size in the shear crippling zone from section to section, micrographs were taken at widely varying magnifications. Thus, the reader is advised to pay careful attention to the line scales on each micrograph. Furthermore, the 0° fibers are always oriented to run from the top to the bottom of each figure.

Fig. 39 Local stress-applied stress data for the Control, L1, and L2 strain gages for the slotted HST-7 specimen during reload/unload testing.

IM6/HST-7

Reload/Unload Test

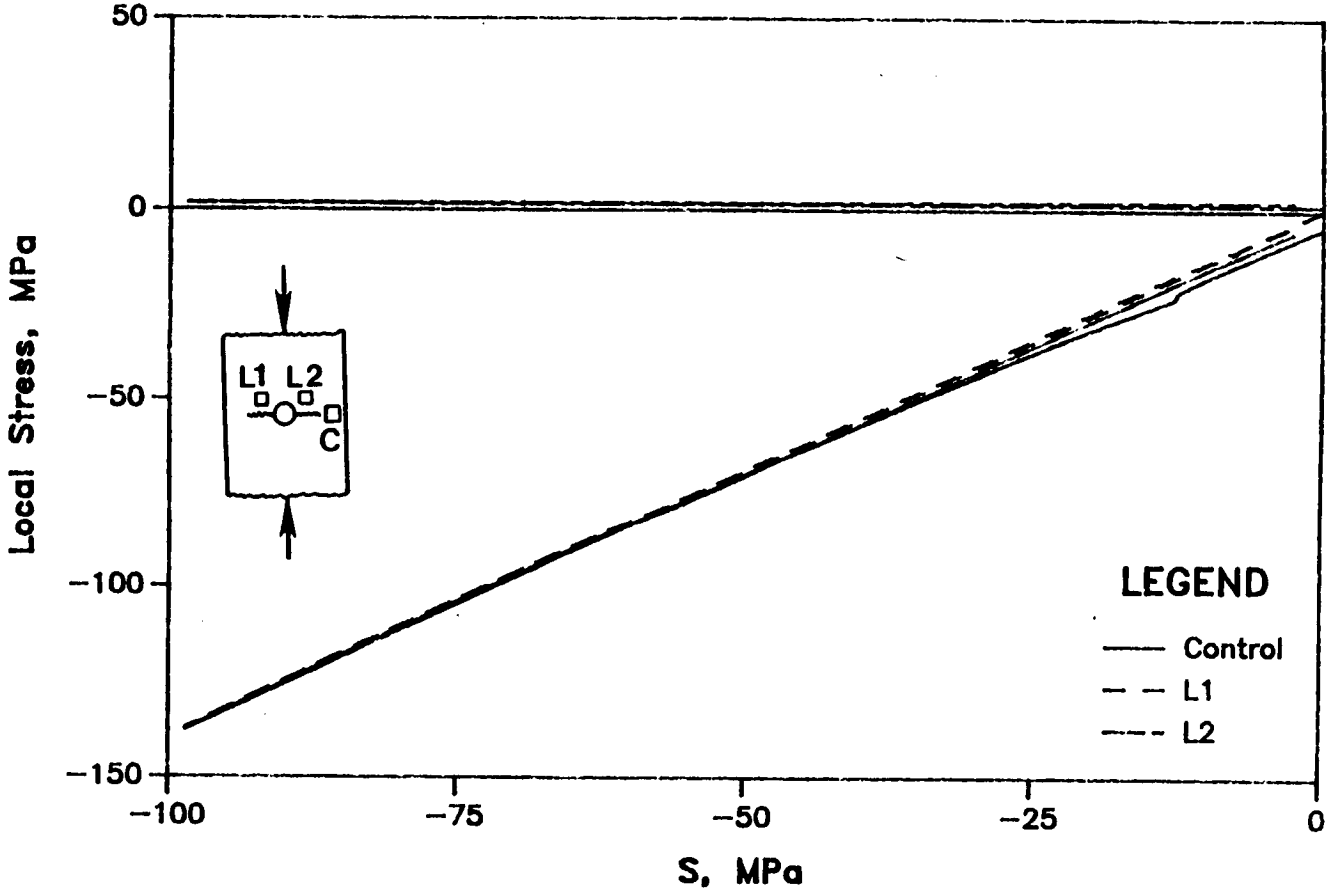

AS4/PEEK, Specimens L and R

The shear crippling zone in the specimen selected for sectioning was shown in Figs. 12a and 33a. Load-displacement data (Figs. 27 and 28) and also measured local stess data (Figs. 24 and 35) has been presented. Table VI summarizes the section depth or amount of material removed from each specimen, for each section examined in the SEM. Refer to Fig. 14 for the specimen configuration for these sectioning studies.

Prior to polishing, the initial examination in the SEM was of the actual damage zone at the edge, or circumference of the hole (Y-Z plane) of both specimens L and R. These micrographs, which are shown in Fig. 40, indicate that the damage extends approximately 16 plies deep (enclosed in boxes) from the visible surface damage. The observed damage occurred on the same face of the specimen on either side of the hole. It only appears to be on opposite faces in Fig. 40 because we are looking in two different directions from the center of the hole. Careful observation shows that the majority of damage is 0° fibers buckled into the hole. The initial examinations of the visible surface damage (X-Y plane), prior to polishing, of both specimens L and R did not show the shear crippling zone because of excess strain gage adhesive and residue from the removal of the gages. However, careful examination into the depth of the hole of specimen L, shows the first group of 0° fibers buckled into the hole (indicated by an arrow on Fig. 41). The hole edte is labeled "HE" for reference in this figure. Because the fibers are covered entirely by resin, one may conclude that this damage is accompanied by very local ply delamination in the resin-rich region at the ply interface. The local ply delamination is helps to accommodate large amounts of shear crippling and fiber microbuckling.

Sectioning Across the Laminate Width - Sectioning across the laminate width

TABLE VI. SECTIONING SPECIFICATION FOR PEEK SPECIMEN.

Specimen L		Specimen R	
Section Number	Section Depth, x_k	Section Number	Section Depth, z_k
1	0.00 mm	1	0.00 mm
2	0.31 mm	2	0.25 mm
3	0.58 mm	3	0.44 mm
4	1.14 mm	4	0.96 mm
5	1.25 mm	5	1.09 mm
6	2.40 mm	6	1.96 mm
7	3.04 mm	7	2.25 mm
8	3.51 mm		
9	3.92 mm		
10	4.64 mm		
11	5.16 mm		

Fig. 40 Initial examination of Y-Z plane showing shear crippling damage extending 16 plies deep from the surface damage.
a) PEEK specimen L.
b) PEEK specimen R.

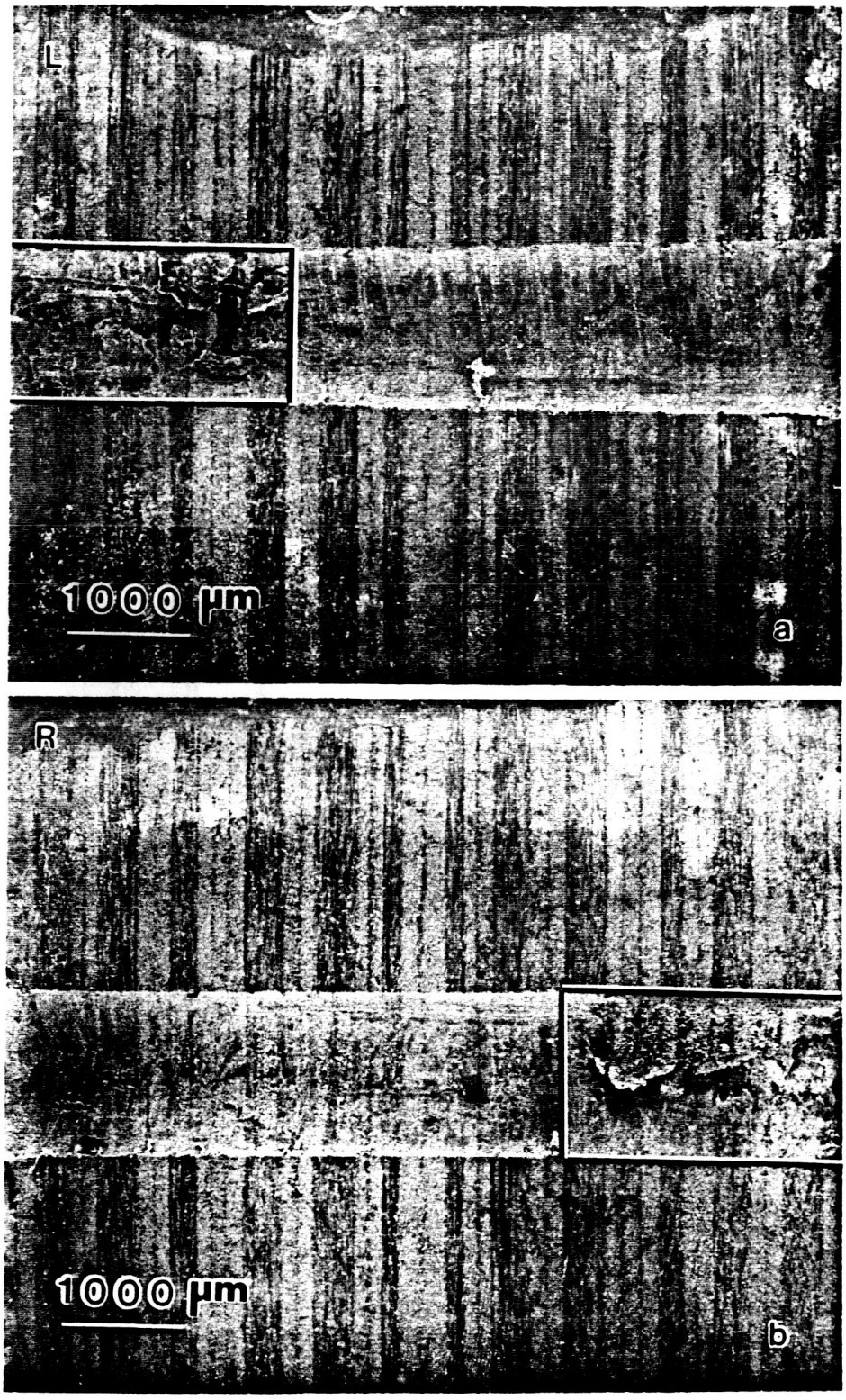

Fig. 41 Initial examination of X-Y plane into the depth of the hole of PEEK specimen L. The arrows on this micrograph show the first group of 0° fibers buckled into the hole.

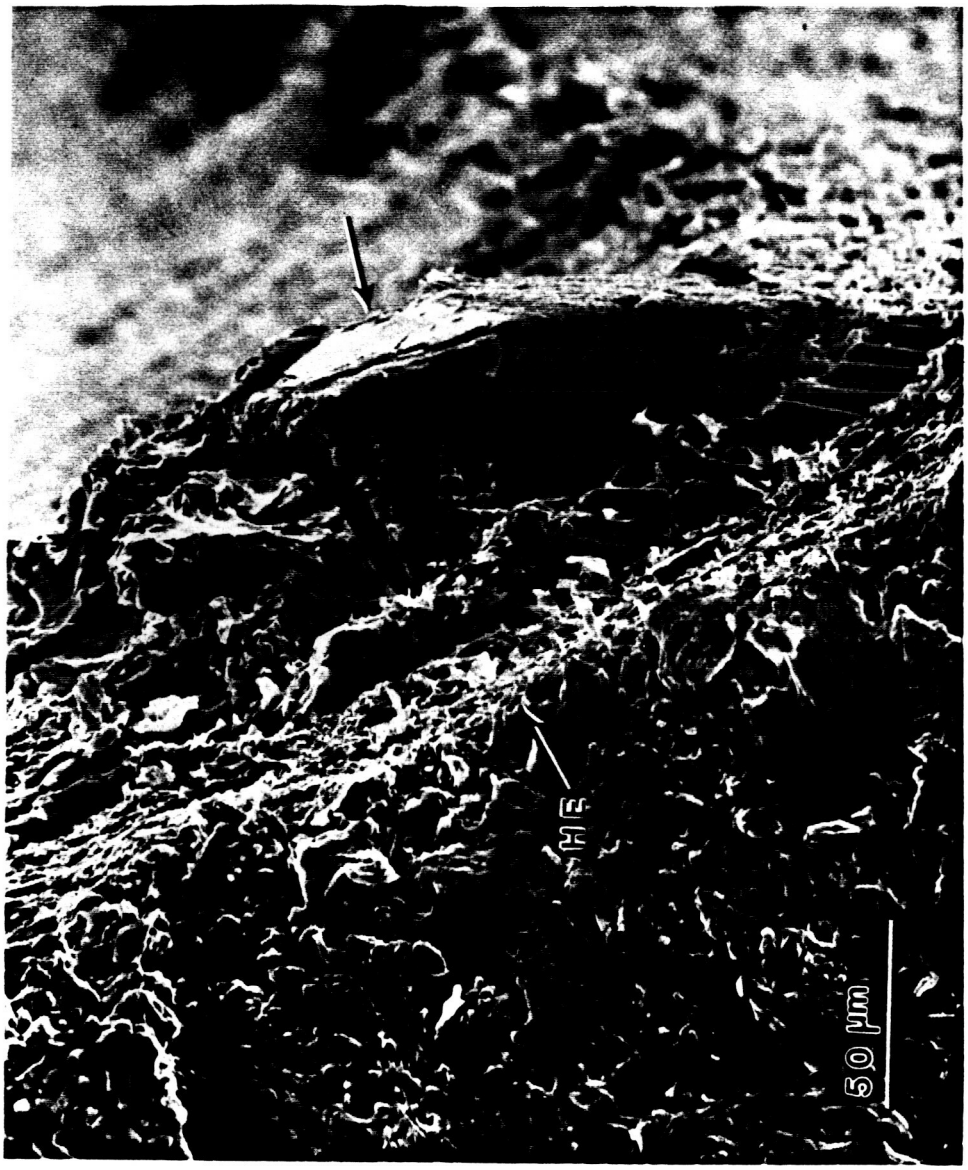

of Specimen L details the interior damage behind the edge of the hole (Y-Z plane). Figure 42 shows section 1, just after mounting and polishing specimen L. At this section, x_k is defined to be 0.00 mm. For consistency, the 0° ply groups have been numbered 1–4 in every figure where appropriate, consecutively counting from the surface damage. This figure shows the shear crippling and fiber microbuckling extending to the fourth group of 0° fibers. The void areas are due to damaged material in the shear crippling zone falling out during the polishing process. The featureless zone along the X axis on the right of the figure is a this layer of strain gage adhesive coating the hole radius. The surface ±45's and the first group of 0's have a slight column buckling shape toward the surface damage. Local delaminations to allow large amounts of fiber microbuckling and/or shear crippling are present at each interface of each group of 0° plies. Local delamination at the -45/0 interface of group 1 and at both interfaces of group 4 are indicated by the arrows on Fig. 42. Other local delaminations are magnified in Fig. 43 for each interface of the second group of 0's and Fig. 44 for the right interface of group 1 (Fig. 44a) and both interfaces of group 3 (Fig. 44b). Additionally, the four different shear crippling zones in 0° ply groups 1–4 (shown in Fig. 42) lie approximately in the X-Z plane at elevations along the Y axis that range over approximately 150 μm.

Figure 45 shows section 2, 0.31 mm from the hole edge. The out of plane (Y-Z) buckling of group 1 0's toward the specimen surface is more pronounced at this section, probably precipitated by shear crippling and/or fiber microbuckling in the X-Y plane. Matrix cracking and deformation is now evident in the ±45 plies connecting groups 1 and 2. The absense of such damage in the first section is probably because the damage in adjacent groups of 0° plies was at nearly the same elevation as measured in the Y direction. Additionally, the shear crippling zones in

Fig. 42 Section 1 (x_k = 0.00 mm) of PEEK specimen L showing shear crippling and/or fiber microbuckling damage in 0° plies. Additionally, the local delamination at the –45/0 interface of group 1 and at both interfaces of group 4 0's are indicated with arrows.

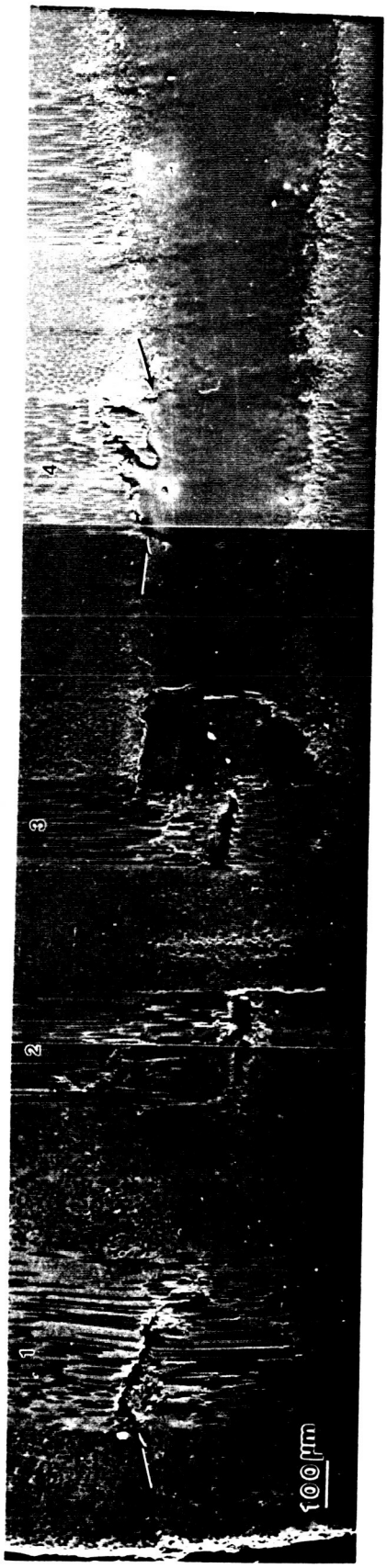

Fig. 43 Details of section 1.
a) Local delamination at the –45/0 interface of second group of 0's.
b) Local delamination at the $0/\pm 45$ interface of second group of 0's.

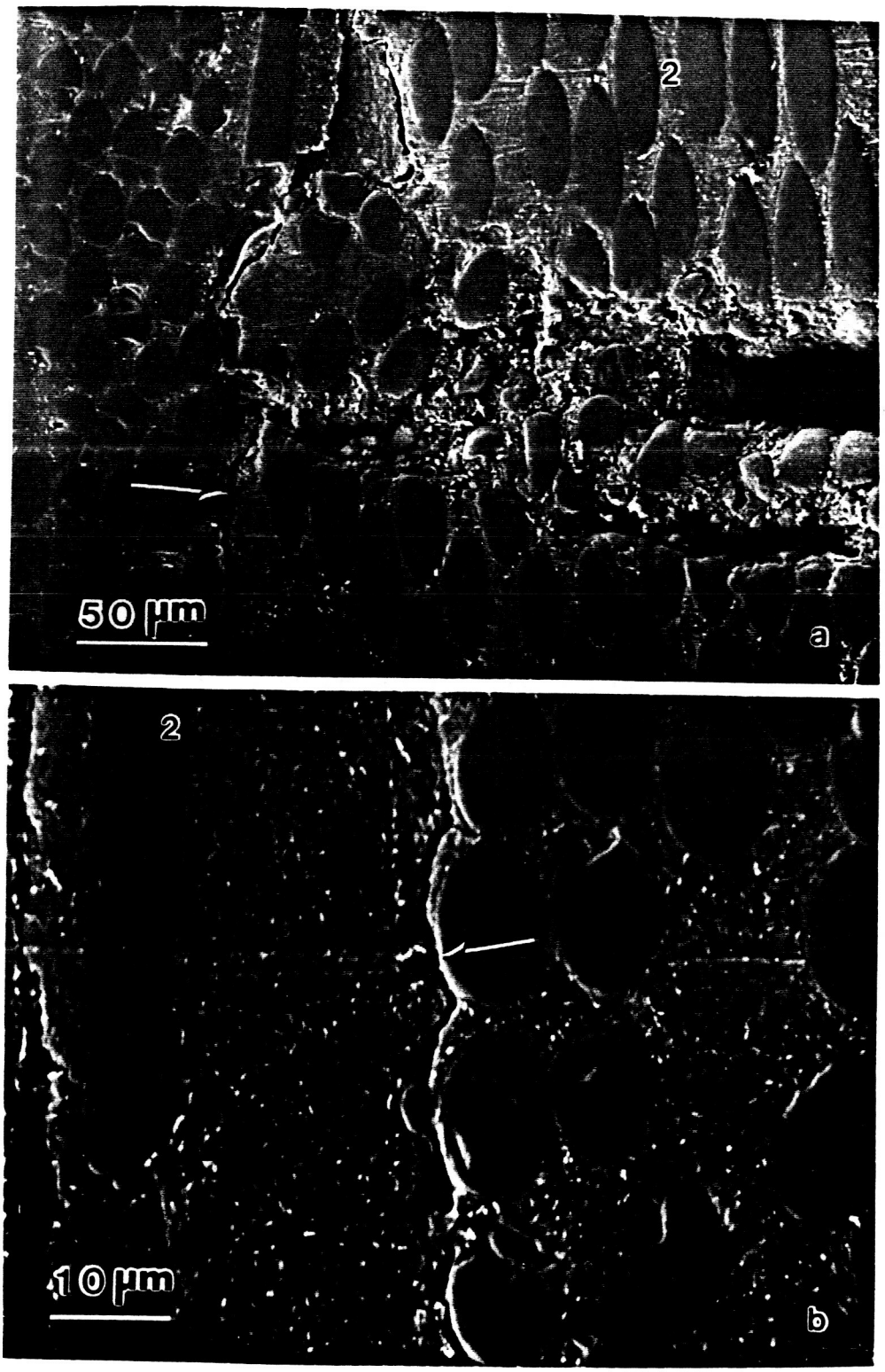

Fig. 44 Details of section 1.
a) Local delamination at the 0/45 interface of first group of 0's.
b) Damage in third group of 0's, including local delamination at each interface. Note that some material has fallen out during the polishing process.

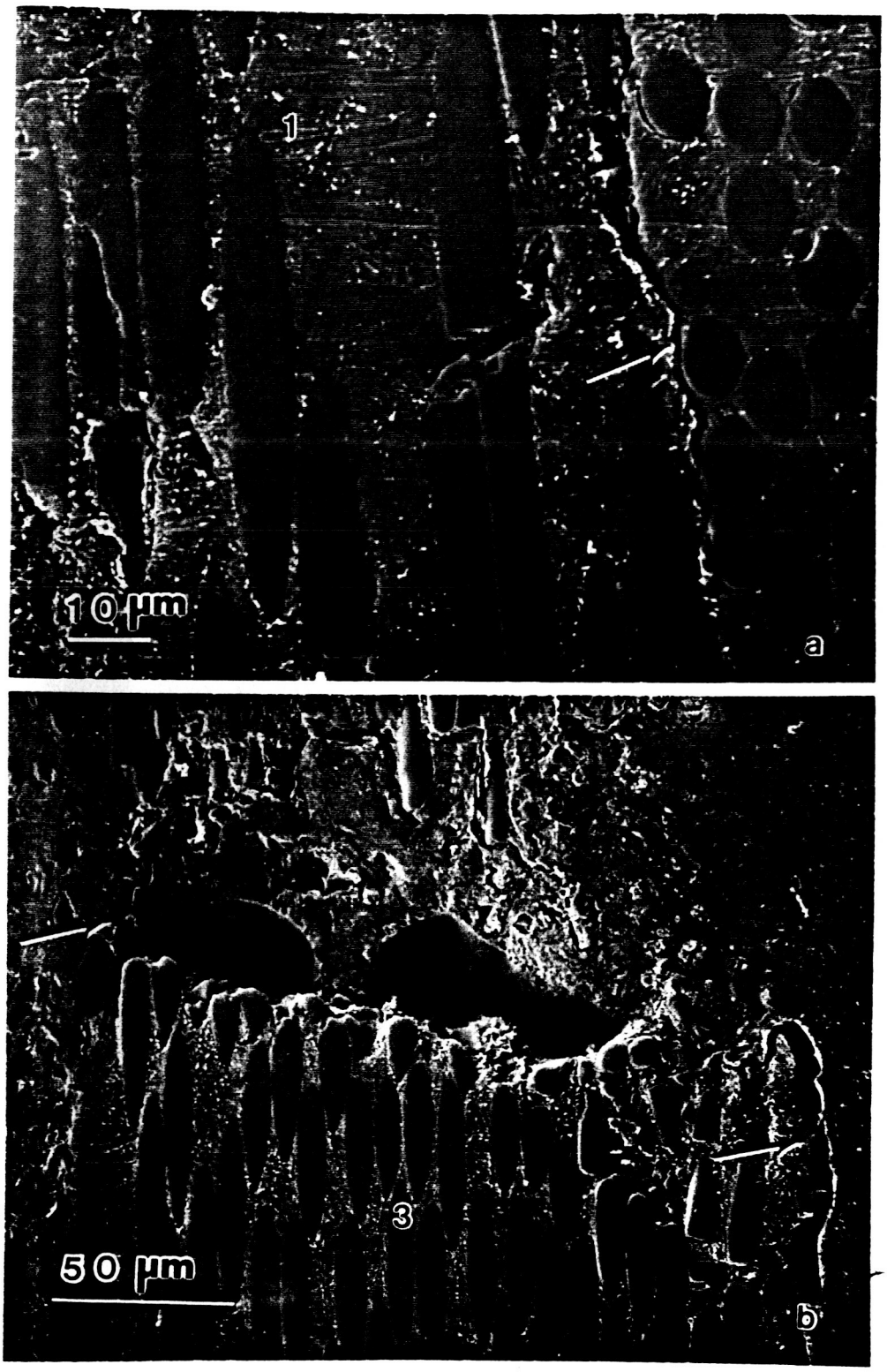

Fig. 45 Section 2 ($x_k = 0.31$ mm) of PEEK specimen L. These micrographs show the out of plane (X-Y) ply microbuckling and matrix cracking and deformation in the ± 45 plies connecting the first and third group of 0's.

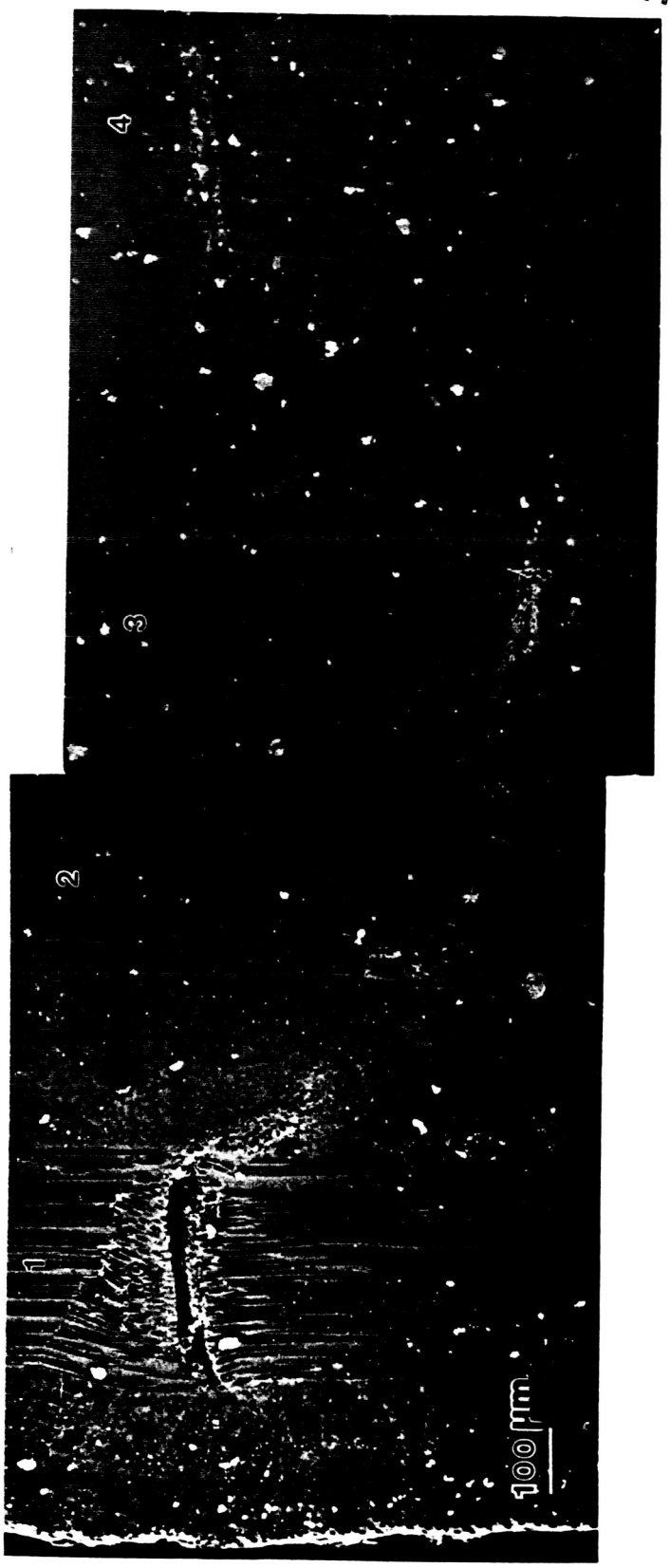

groups 1–4 now measure 500 μm apart along the Y axis, and thus the damage in the Y-Z plane is spreading apart. The spreading of shear crippling damage along the Y axis indicates that the damage in the 0° plies in the X-Y plane must be growing at positive and negative angles measured with respect to the X axis. The size of the local delaminations at each interface of 0° ply groups 1–3 is significantly reduced, and the local delaminations at the ply interfaces of group 4 have disappeared. The local delaminations at the left and right interfaces of the 0° ply groups 1–3 are shown in Figs. 46–48, respectively. Furthermore, the circular fiber ends within the 0° ply in Fig. 48 indicate kinking in the X-Y plane while the kinked fibers in Fig. 45 indicate kinking in the Y-Z plane.

Figure 49 shows the shear crippling damage in section 3 of specimen L, 0.58 mm from the hole edge. In addition to the shear crippling in the four groups of 0° plies, matrix cracks appeared in the 12^{th}, 24^{th}, and 25^{th} plies, all 90° plies (indicated by arrows). Note that some groups of 0° plies contain two individual plies (see stacking sequence given in Table I). Thus, the 12^{th} ply lies in the 6^{th} group, with only the 0° ply groups numbered 1–4. This appearance was the first and only observation of damage in the 90° plies. The shear crippling zone near the surface damage zone is buckled further out of the X-Y plane than in previous sections. The matrix cracking and deformation in the ±45° plies connecting group 1 and group 2 0's is much larger than that seen previously in section 2 and also runs along the ± 45 interface. The out of plane shear crippling (Y-Z plane) can only be accommodated by shear deformation in the adjacent ±45° plies. An uneven stiffness in the first and second group of 0's, resulting from the different sizes of shear crippled zones within these plies, would give a shear stress in the Y direction in the X-Y plane that could coalesce the shear damage introduced by the shear crippling, as seen

Fig. 46 Details of section 2.
a) Local delamination at the –45/0 interface of group 1 0's.
b) Local delamination at the 0/45 interface of group 1 0's.

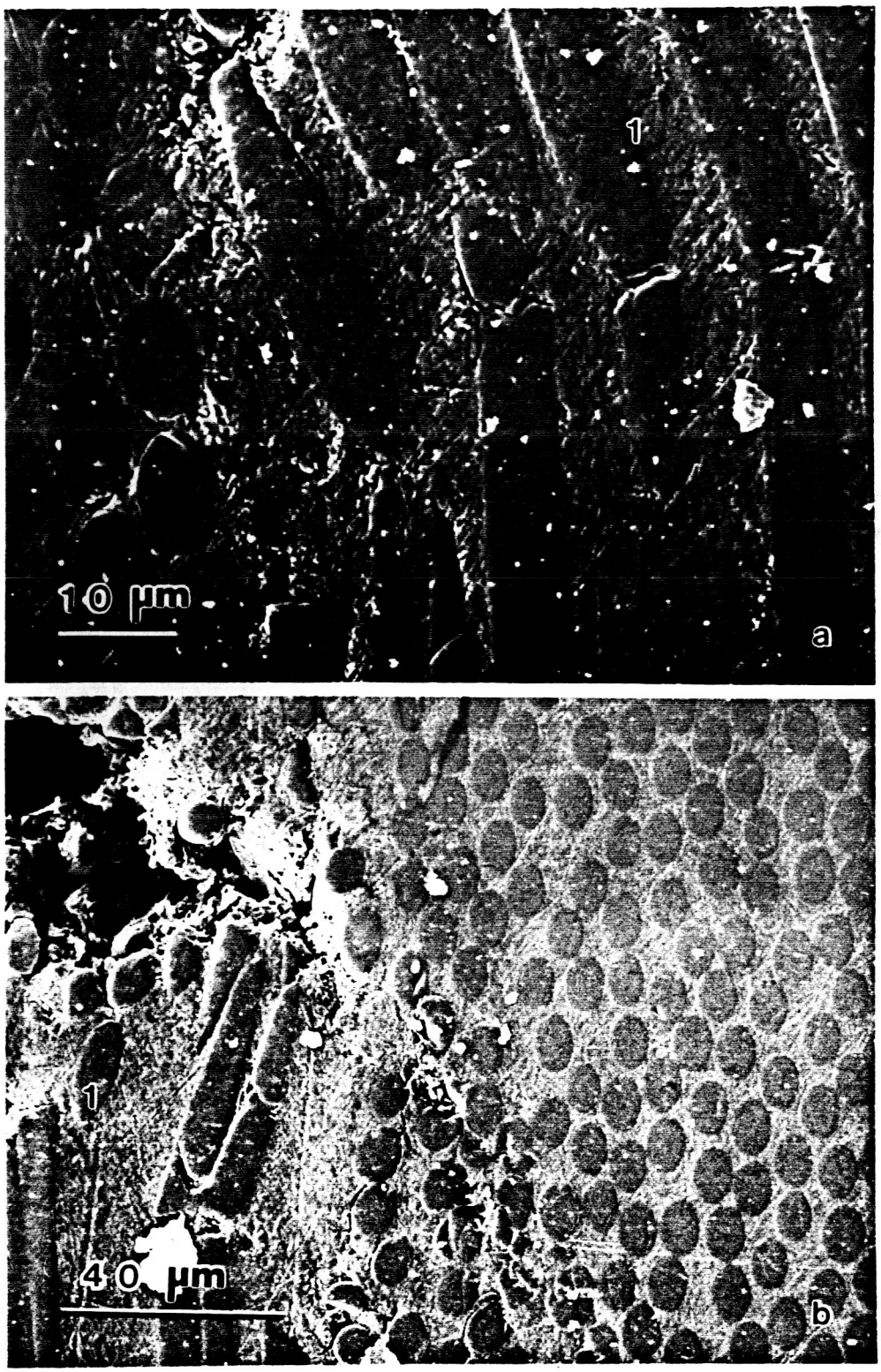

Fig. 47 Details of section 2.
a) Local delamination at the –45/0 interface of group 2 0's.
b) Local delamination at the 0/45 interface of group 2 0's.

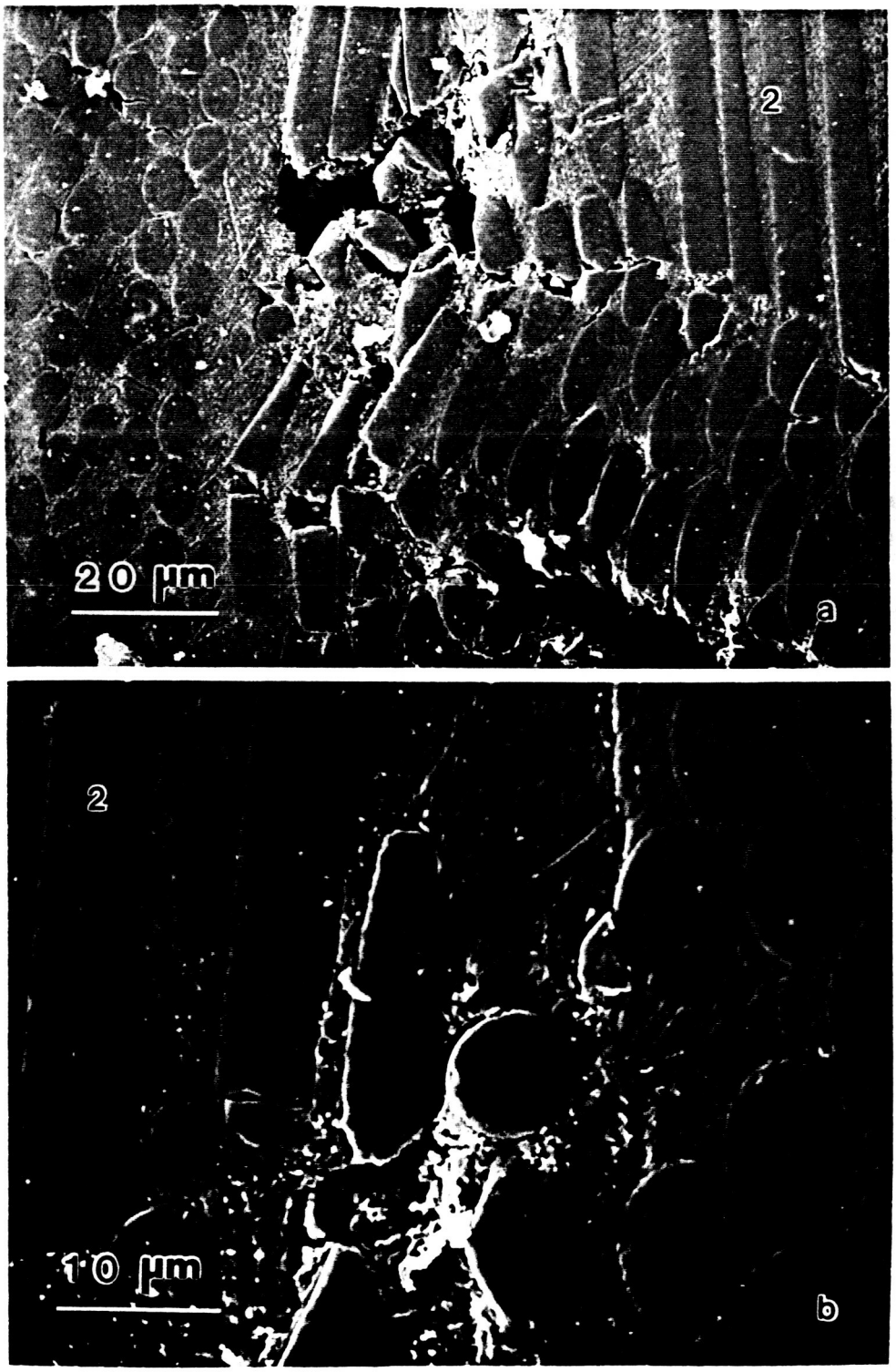

Fig. 48 Details of section 2.
a) Local delamination at the –45/0 interface of group 3 0's.
b) Local delamination at the 0/90 interface of group 3 0's.

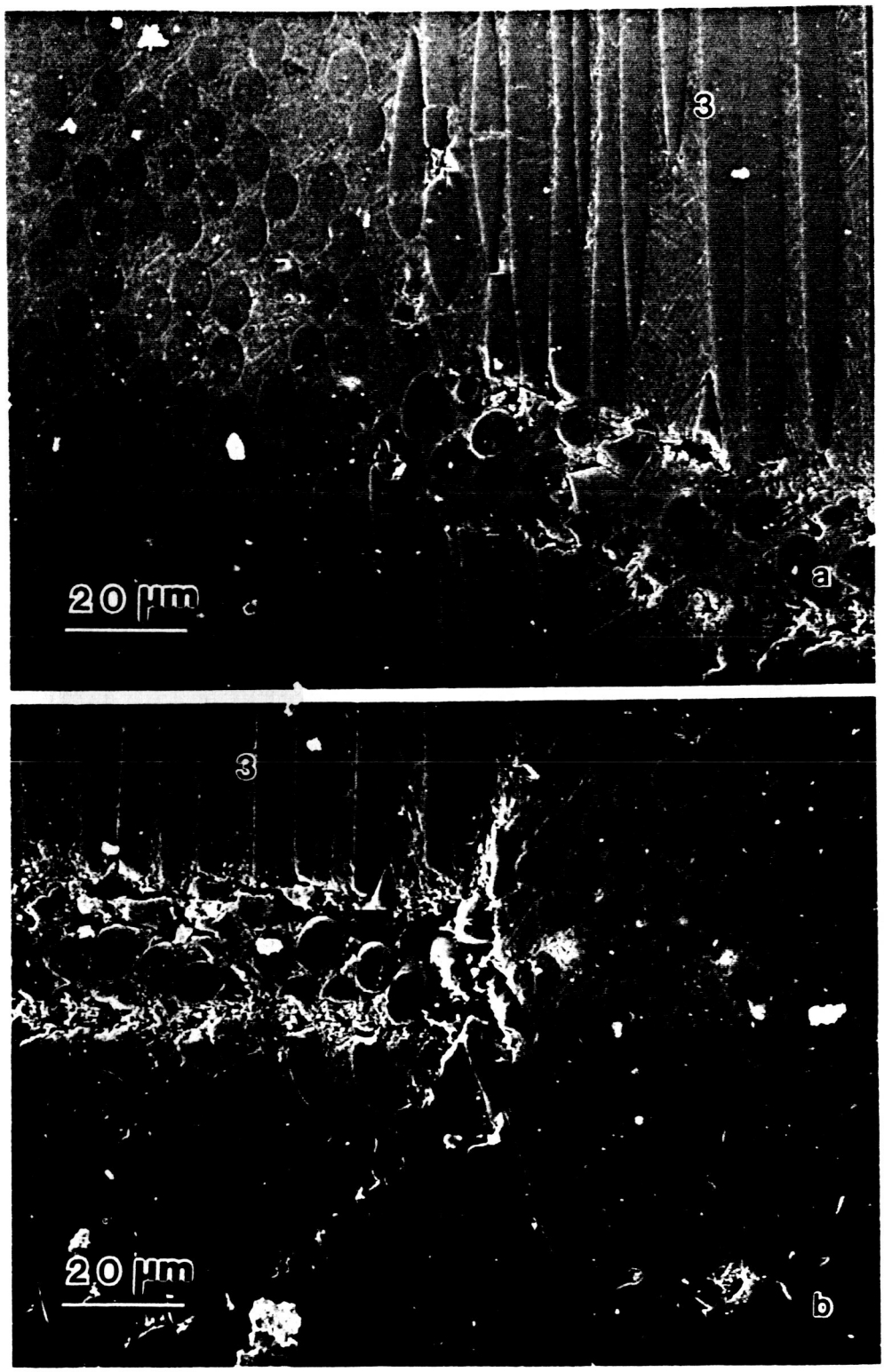

Fig. 49 Section 3 ($x_k = 0.58$ mm) of PEEK specimen L. The out of plane (X-Y) buckling matrix deformation in the ± 45's is very predominant in these micrographs.

in Fig. 49. Furthermore, the radial type matrix cracking is now evident in the $-45°$ ply closest to the specimen surface. The elevation in the Y direction of the shear crippling in the 0° plies now ranges over 650–700 μm, indicating again that the damage planes associated with shear crippled zone grows at various angles to the X axis. The details of this damage are magnified in Fig. 50, enlarging the matrix cracking and deformation in the ± 45's, rotating and kinking within the 0° plies, the 0° fiber damage pertruding into the 45° plies, and the absence of local delaminations at the ply interfaces. It appears in this case that the fiber kinking or microbuckling in the X-Y plane produces a plane (X-Z) of material which can easily shear giving out of plane (Y-Z) shear crippling.

An overview of section 4, made 1.14 mm from the hole edge is shown in Fig. 51. The bright, shiny spots are damaged regions that are charging because of the uneven conductive coating on the damaged material. The shear crippling zones in the 0° plies measure 1150 μm apart along the Y axis in the Y-Z plane. The shear crippling zones in the 0° fibers are spread 1150 μm apart along the Y axis, but the connecting damage in the $\pm 45°$ plies between the first and second group of 0° plies is significantly reduced. However, the matrix cracking and deformation in the near surface $-45°$ ply seen in section 3 is now connected to the shear crippling in the first group of 0's. Furthermore, this damage appears to be initiating a delamination at the ± 45 interface, as indicated by an arrow in Fig. 52. The shear crippling damage in the 0° ply seems to be driving this damage in the $-45°$ ply. The size of the shear crippling zone within each group of 0's was smaller than in the previous section.

Figure 53 shows section 5 at 1.25 mm from the hole edge. The damage in the 0° plies ranges over 1200 μm apart along the Y-direction, and the connectiong

Fig. 50 Details of section 3.
a) Rotating and kinking (X-Y and Y-Z planes) in group 1 0's, including matrix deformation and cracking in the adjacent 45's.
b) Rotating and kinking (X-Y and Y-Z planes) in group 2 0's.

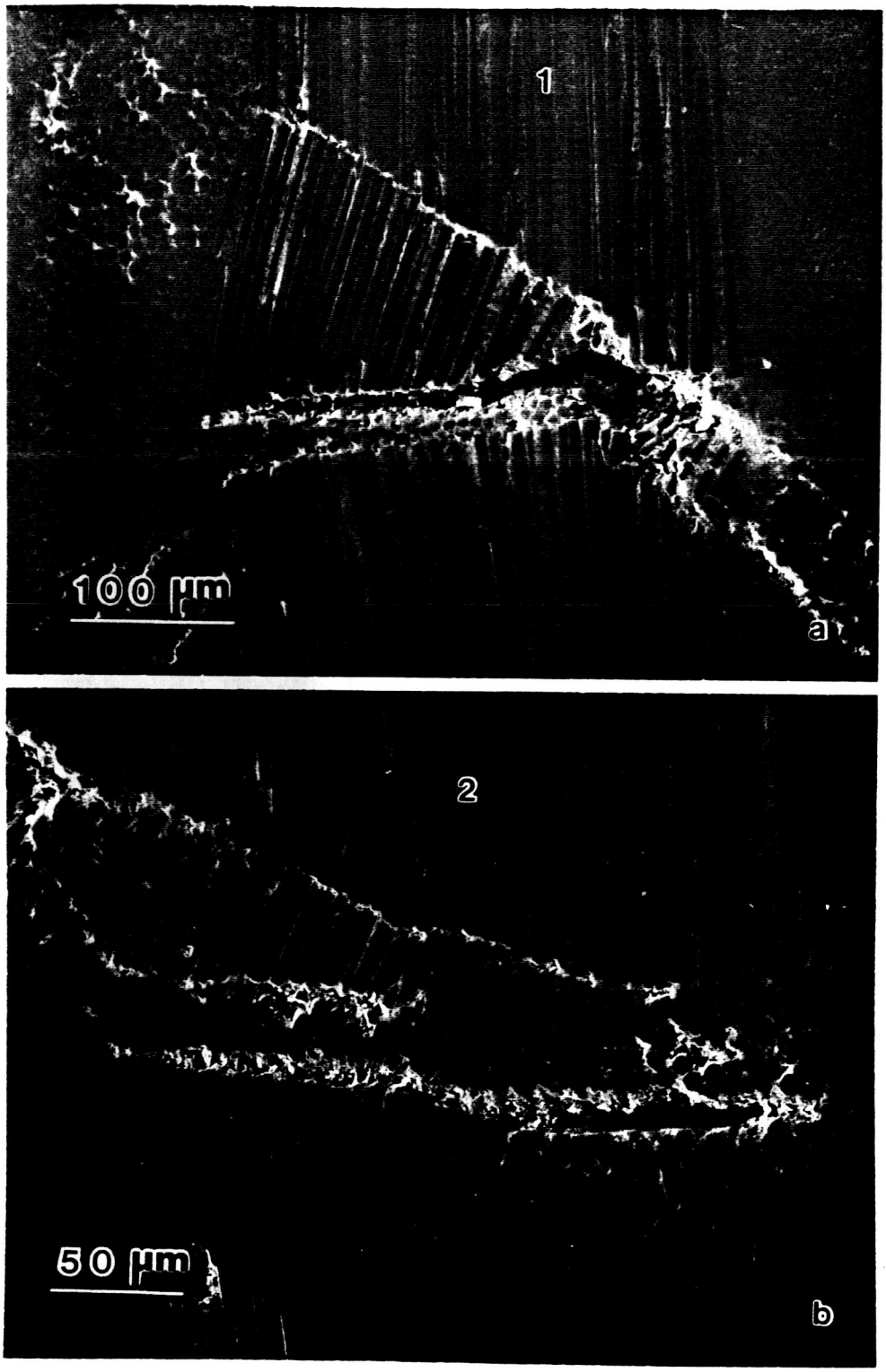

Fig. 51 Shear crippling zone in section 4 ($x_k = 1.14$ mm) of PEEK specimen L.

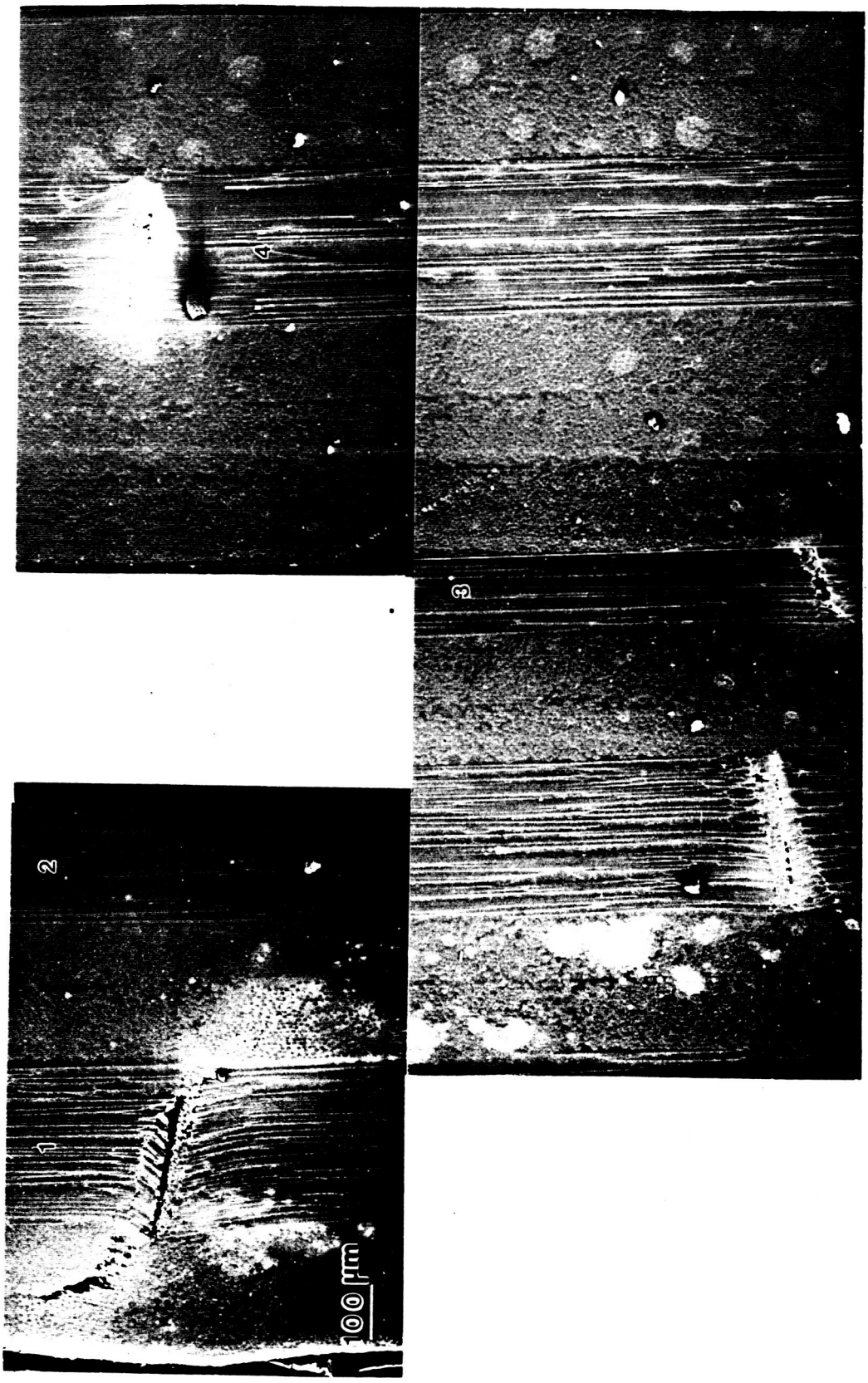

Fig. 52 Details of section 4.
Shear crippling zone in the near surface −45° ply.

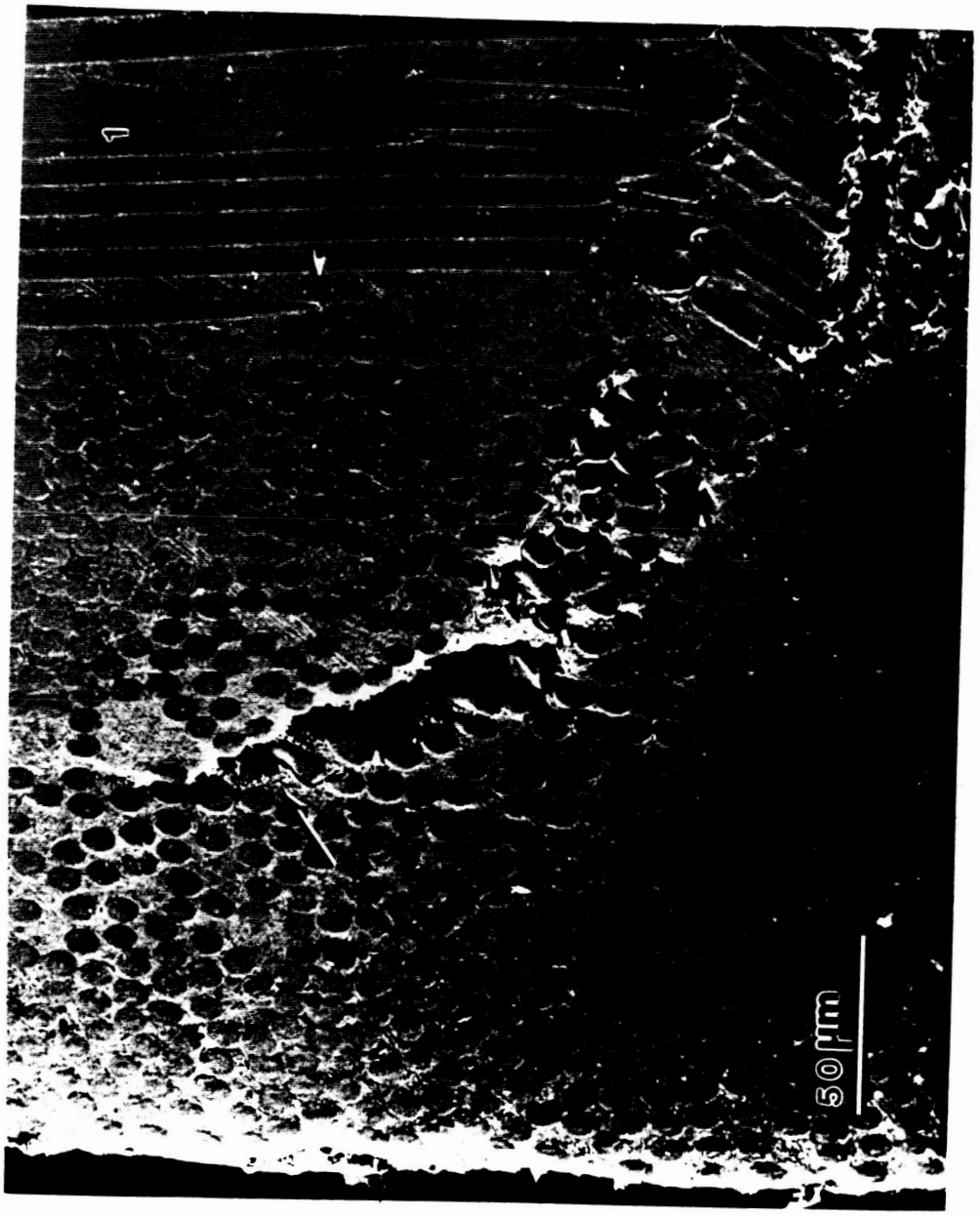

Fig. 53 Shear crippling zone in section 5 ($x_k = 1.25$ mm) of PEEK specimen L.

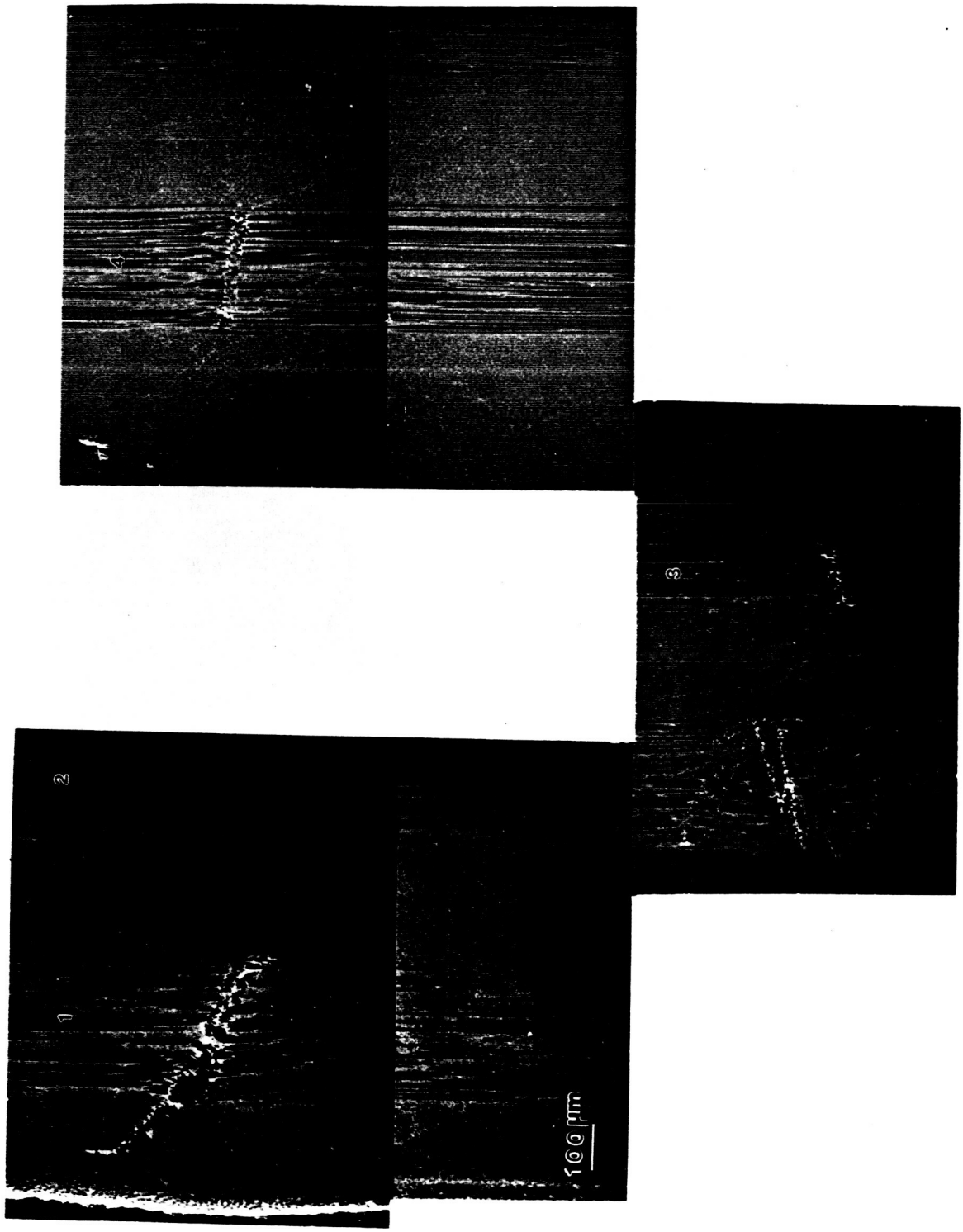

Fig. 54 Details of section 5.
Shear damage within second group of 0° plies.

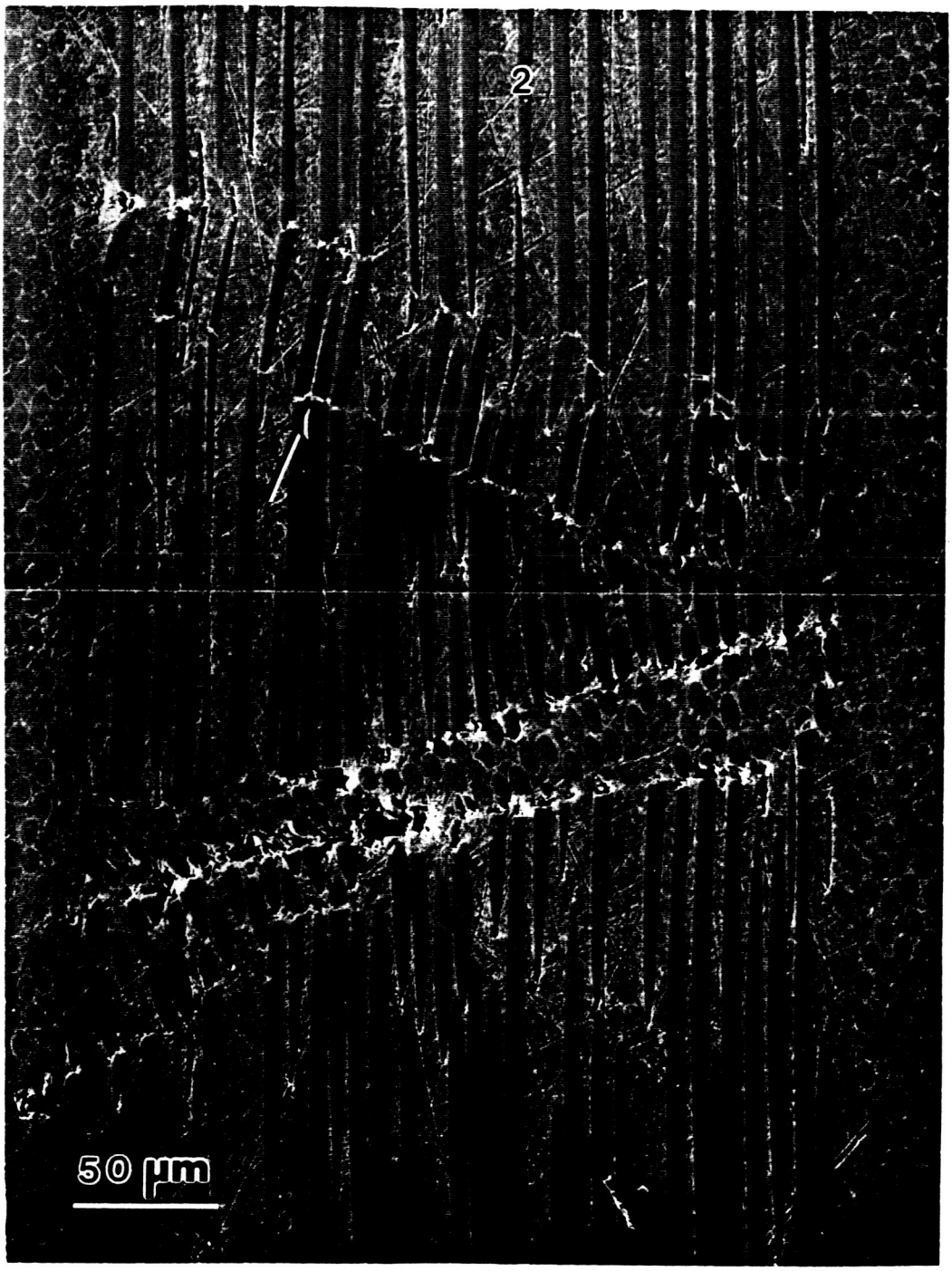

damage in the interior ±45° plies has completely disappeared. The near surface −45° damage is still connected to the shear crippling of the first group of 0° plies. Within the second group of 0° plies, the shear crippling has split into 2 planes, as seen at higher magnification in Fig. 54. The different sizes of the polished fiber ends in this figure further substantiate the rotating and kinking in both the X-Y and Y-Z planes previously described. Furthermore, this micrograph shows that the 0° fibers are generally failed in bending under compression loading (an example is indicated by the arrow on the figure).

By section 6 (2.40 mm form the hole edge) no damage is found in the third and fourth groups of 0° plies, thus only the first and second groups are shown in Fig. 55. Furthermore, the out of plane surface buckling and discontinuity at the −45/0 interface is more pronounced. The damage extending into the −45° ply has turned downward now, but it still appears to be driving a delamination at the ±45 interface (indicated by an arrow). The damage in the first and second 0° plies is now 1250 μm apart in the Y direction. The damage in the first group of 0° plies is enlarged in Fig. 56. This figure highlights the damage previously discussed and shows the bending type breaks in the fibers. The bending away from the straight right-hand interface of the first group of 0° plies (magnified in Fig. 57) indicates fiber buckling toward the surface. It appears that an out of plane (Y-Z) buckle initiated the damage. This buckle leads to breakage at three points (A,B,C) along the fiber length. This local instability propagates through the thickness of the ply as indicated in the schematic drawing included in Fig. 58. The shear strain associated with the propagation of this kink is seen to propagate into the adjacent ±45° ply. However, it should be noted that no in-plane (X-Y) buckling or shear crippling is seen at this larger distance from the hole. Additionally, some fiber/matrix local

debonds are present and one is indicated by an arrow on Fig. 57.

Fig. 59 shows section 7 (x_k = 3.04mm) for the PEEK specimen. The overview of damage shown in Fig. 59a shows the only remaining shear crippling damage in the first group of 0° plies, still extending downward into the −45° ply. Part of the fiber kink band, including additional bending type fiber breaks within the kink band, is magnified in Fig. 59b.

Section 8 (3.51 mm from the hole edge) looked very similar to section 7 under the light microscope, so it was not examined in the SEM. Section 9 (3.92 mm from the hole edge) was examined in the SEM, but no micrographs were taken because the damage was again similar to section 7. At section 10 (x_k = 4.64 mm), the only remaining damage was shear crippling in the first 0° plies, and by section 11 (5.16 mm form the hole edge), no damage was found when examined in the SEM. The micrographs for sections 1–11 clearly illustrate the reduction in shear crippling zone size as the sections examined get farther from the hole edge.

Sectioning Through the Laminate Thickness - The sections examined through the thickness of the PEEK specimen R are summarized in Fig. 60. Section 1, just after the specimen was mounted and slightly polished, is shown in Fig. 61. At this section, z_k is defined to be 0.00 mm. The shear crippling zone extends 4 mm (measured along the X axis) from the edge of the hole at an angle approximately −20° from the X axis. The polishing removed much of ±45° plies, with the first group of 0° plies evident just adjacent to the hole at the left edge of the micrograph. The bifurcation damage zone seen at greater distance from the hole can be readily understood by comparison with Figs. 55 and 56. These regions represent two distinct areas of damage associated with out of plane (Y-Z) kink band formation. Details of the shear crippling zone in the 0° ply are shown in Fig. 62. The fiber

Fig. 55 Shear crippling zone in section 6 (x_k = 2.40 mm) of PEEK specimen L.

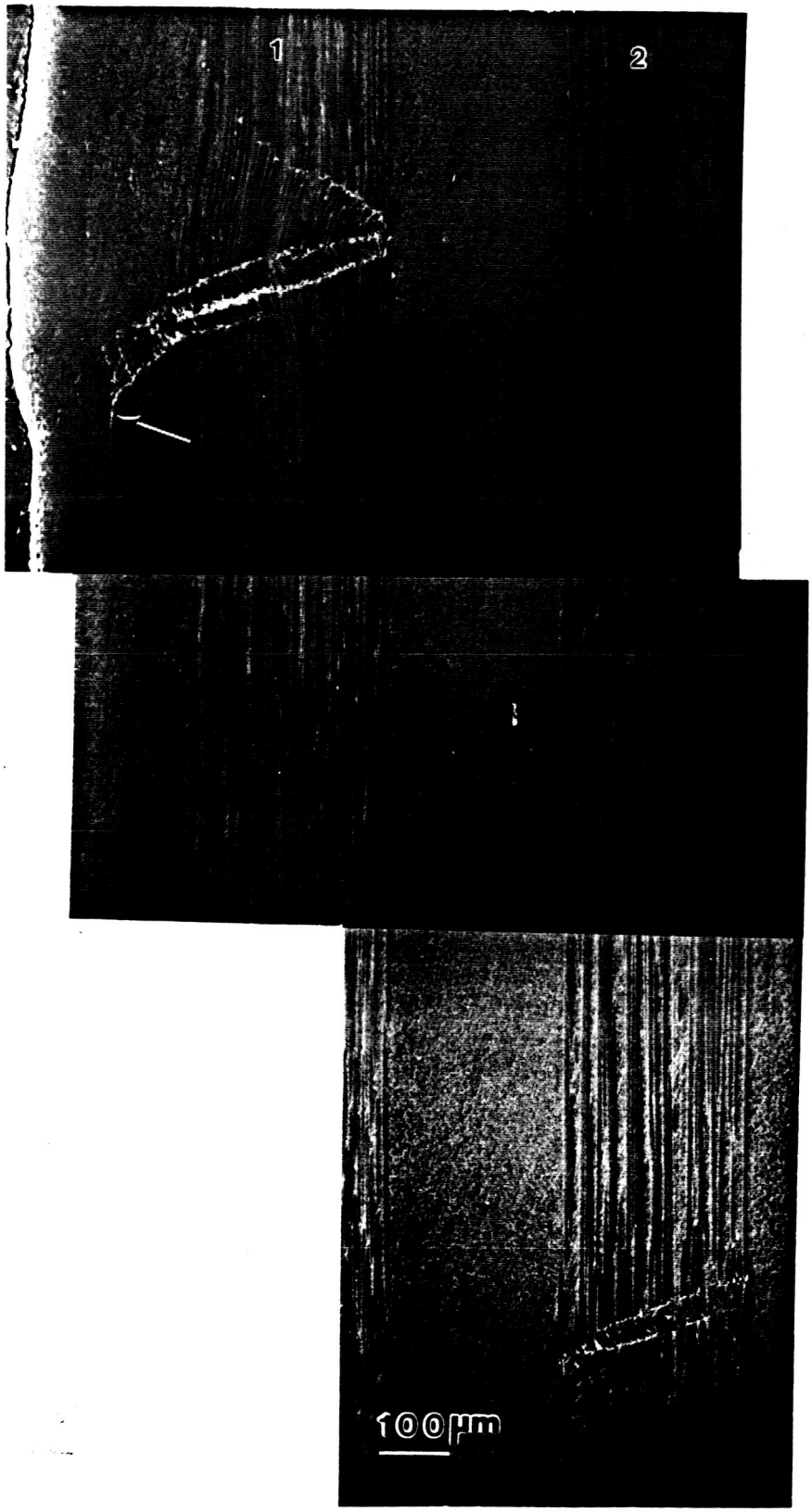

Fig. 56 Details of section 6.
Out of plane (Y-Z) shear crippling in the first group of 0° plies.

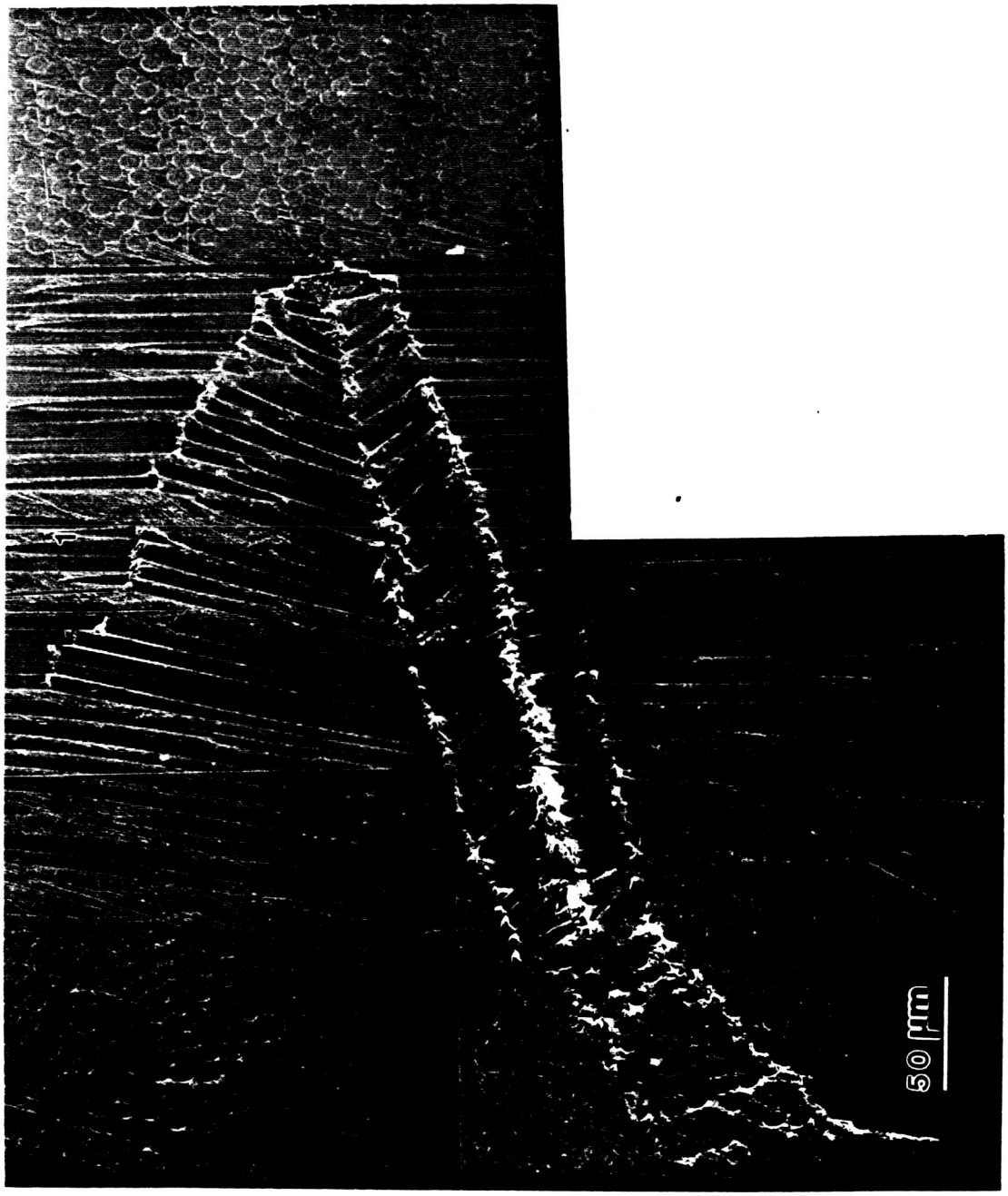

Fig. 57 Details of section 6.
Local out of plane fiber buckle in the first group of 0's.

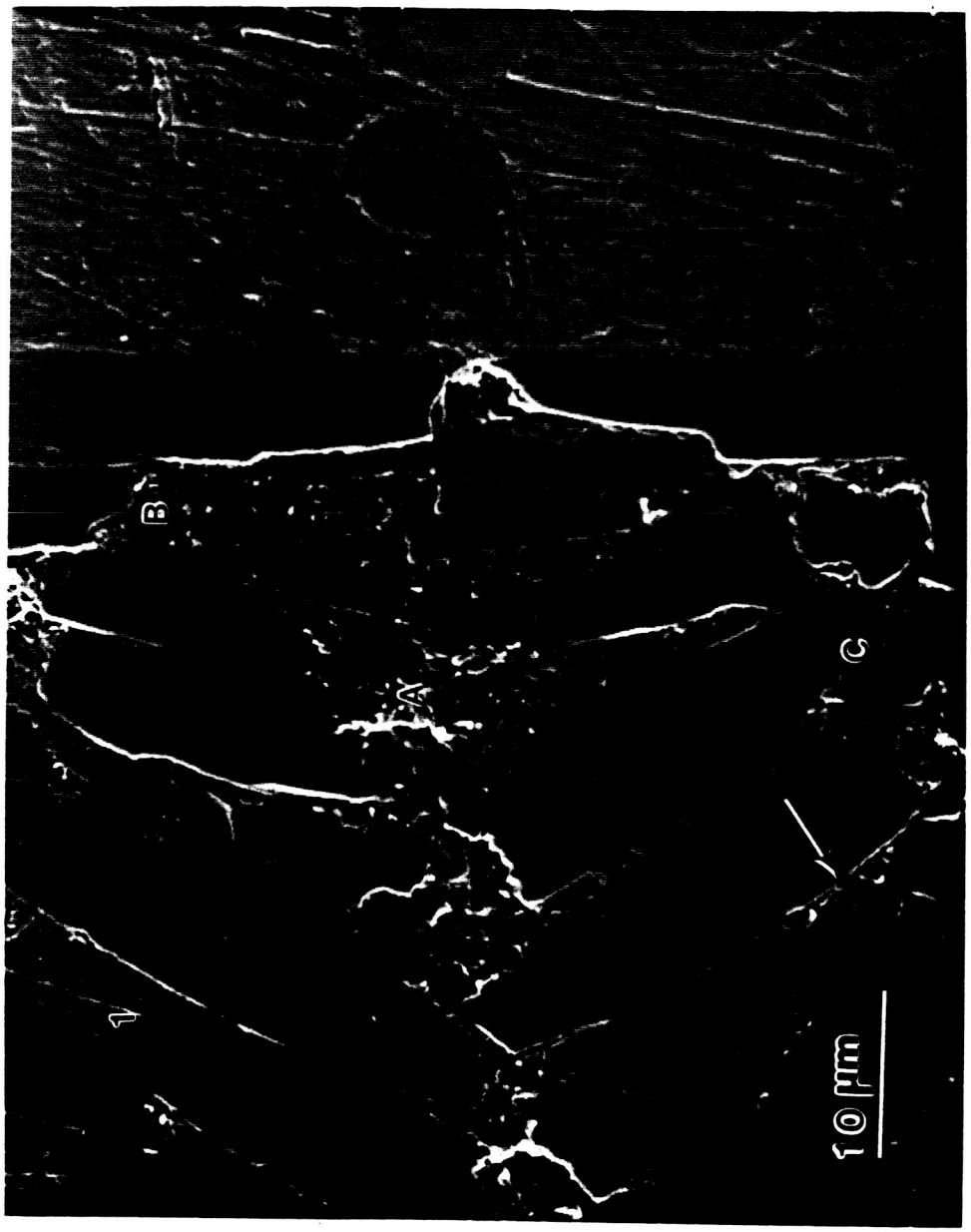

Fig. 58 Schematic drawing of fiber buckle causing local instability (shown in Figs. 56 and 57) through the thickness of the ply.

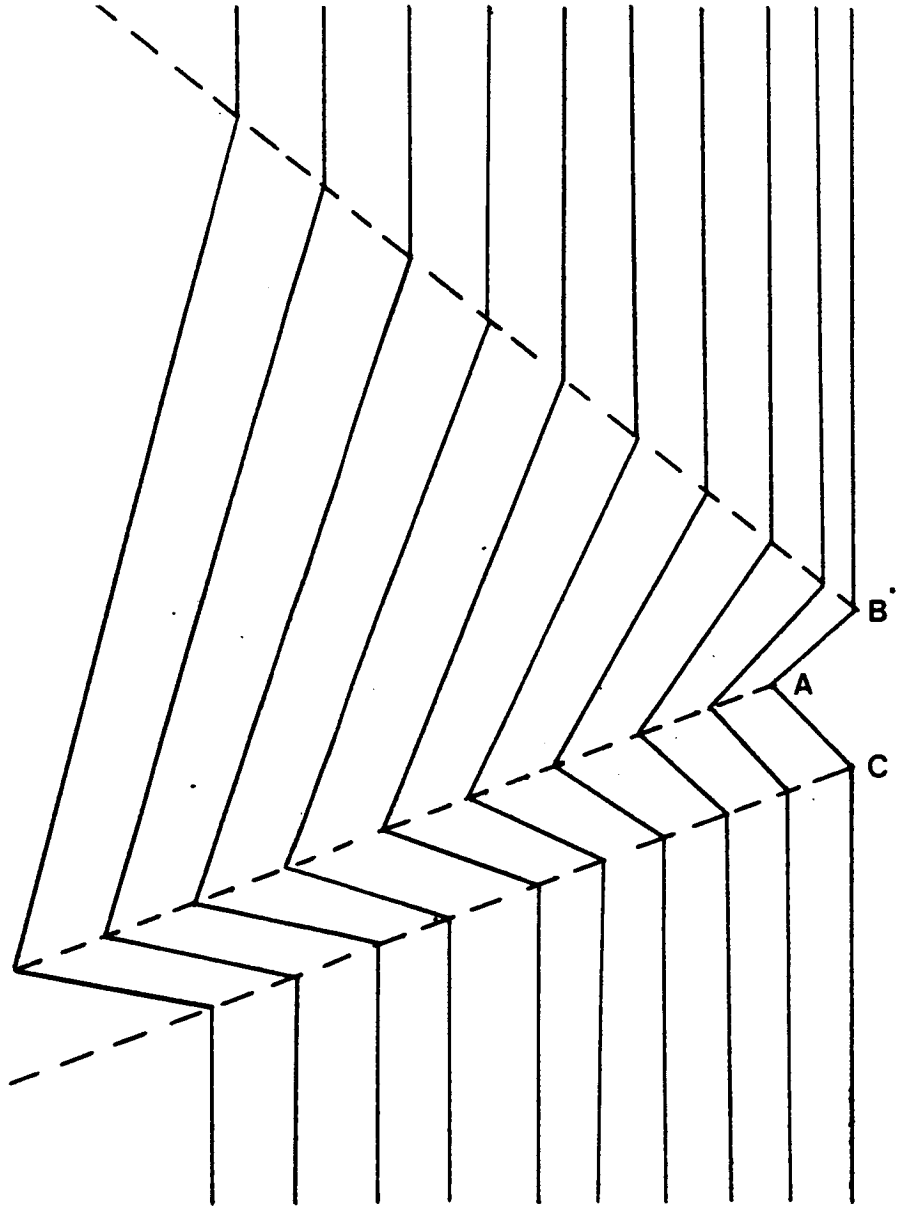
B
A
C

Fig. 59 Section 7 (x_k = 3.04 mm) of PEEK specimen L.
a) Overview of shear crippling damage seen in section 7
b) Bending type fiber breaks within the shear cripling zone.

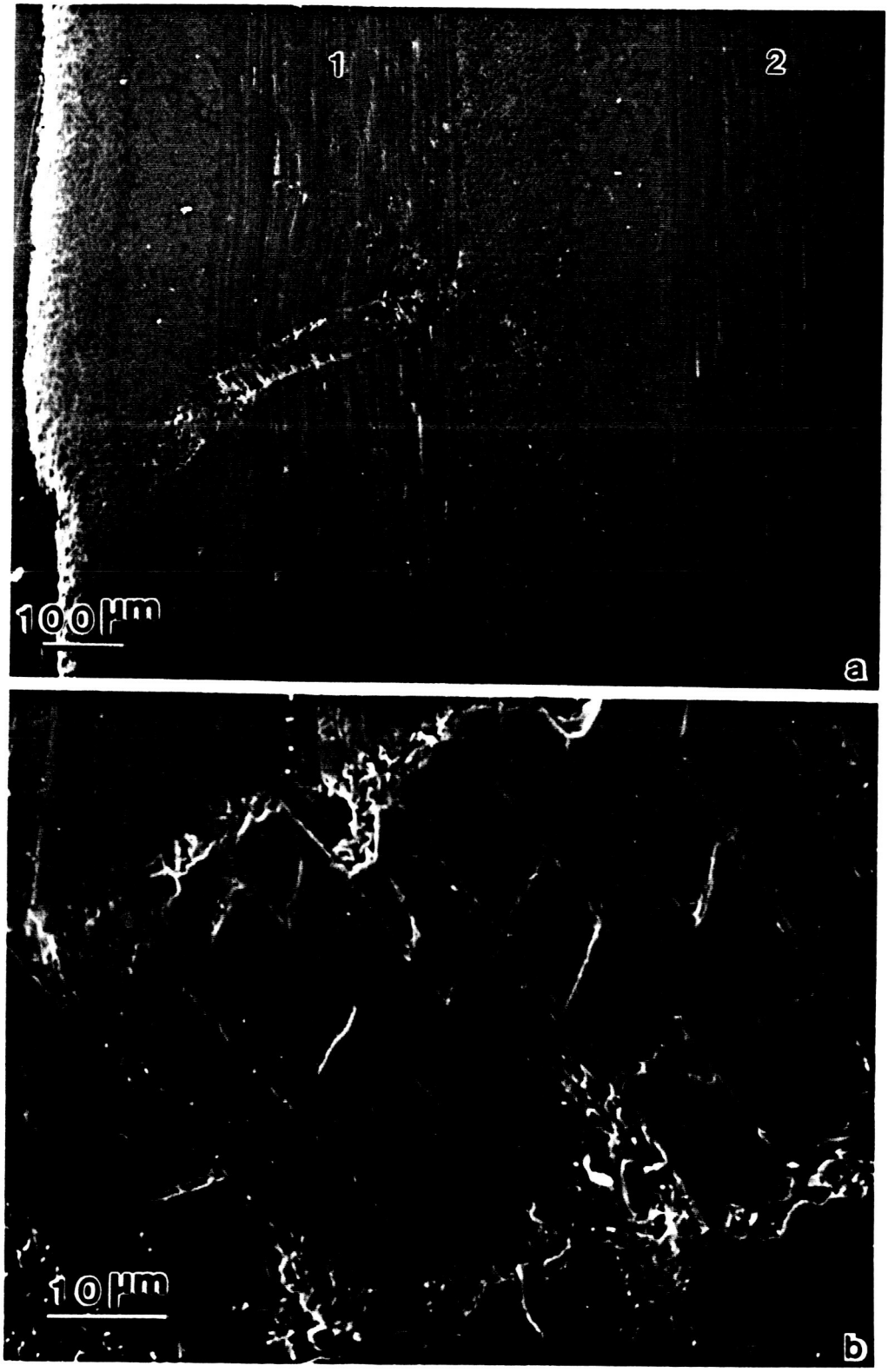

kink band and round 0° fiber ends in Fig. 62a indicate that the fibers are kinking in the X-Y and the Y-Z planes. The height of the shear crippling zone in the ±45° ply is measured to be 300 μm. The fiber kinking in the Y-Z plane in the ±45° ply is magnified in Fig. 62c. This figure also shows the local delaminations required to allow the fibers to rotate and kink.

Figure 63 shows the damage is section 2 (0.25 mm from the specimen surface), which is the first group of 0° plies. The shear crippling zone extends along the X axis approximately 4.25 mm at an average angle of $-20°$ from the X axis. Note that this size is similar to the extent of damage seen in sequential Y-Z sectioning (specimen L). Details of this damage are shown in Fig. 64. Apparently the shear crippling zone initiates with the 0° fibers buckling into the unsupported hole, allowing the kink band to form. The rotating and kinking may actually initiate and drive the formation of additional kink bands branching off of the shear crippling zone, as shown in Fig. 64a. Eventually, the shear crippling zone (within the 0° plies) terminates in the X-Y plane with a reduction of broken fibers as shown in Fig. 64b.

Figure 65 shows section 3, 0.44 mm from the specimen surface. The extent of damage in these ±45° plies is (400 μm), which is an order of magnitude smaller than the damage observed in adjacent 0° plies. Apparently further loading is needed to propagate the damage from the 0° plies into the ±45° plies to a more extensive degree. Local delamination (indicated by an arrow on the figure) and fiber bending breaks are shown in Fig. 65b.

Section 4 (0.96 mm from the specimen surface) was polished to the next ±45° plies. No damage was found at this section, and thus, no micrographs were taken.

Section 5 (1.09 mm from the specimen surface) shows the damage in the third

Fig. 60 Location of sections examined in PEEK specimen *R*.

$$[\underbrace{\pm 45}_{1}/\underbrace{0_2}_{2}/\ \pm\underbrace{45}_{3}/0_2/\ \pm\underbrace{45}_{4}/\underbrace{0}_{5}/90/\ \pm 45/\underbrace{0_2}_{6}/\ \pm 45/\underbrace{0_2}_{7}/\ \pm 45/0/90/\ldots \mp 45]$$

Fig. 61 The shear crippling zone in section 1 ($z_k = 0.00$ mm) of PEEK specimen R, just after mount and polish. Note that some of the 0° ply beneath the ±45° plies is seen near the hole.

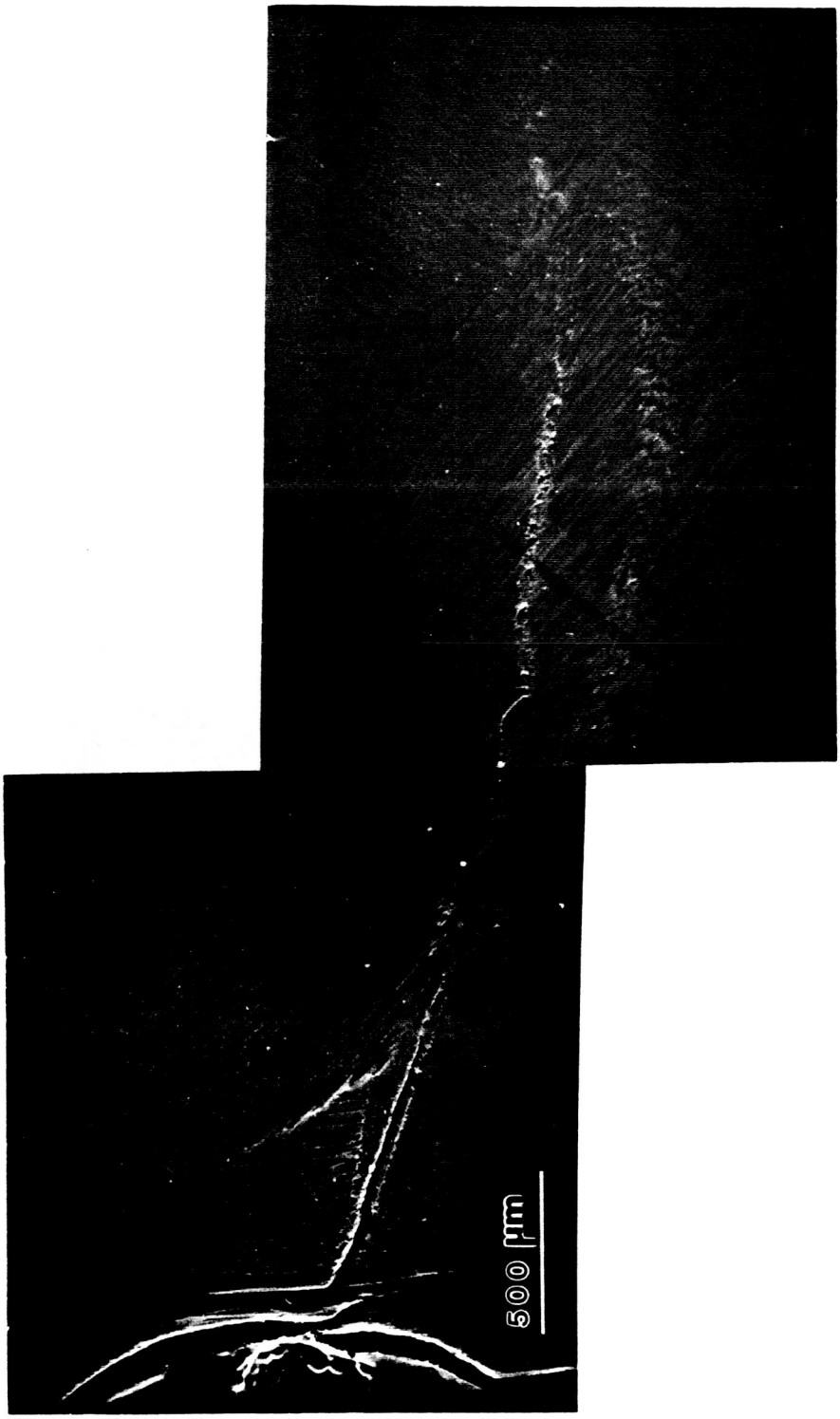

Fig. 62 Details of section 1.
a) Rotating and kinking (in both the X-Y and Y-Z planes) in the 0° ply beneath the ±45° plies.
b) The height of the shear crippling zone in the ±45° plies is 300 μm.
c) Magnification of the fiber kinking in the Y-Z plane.

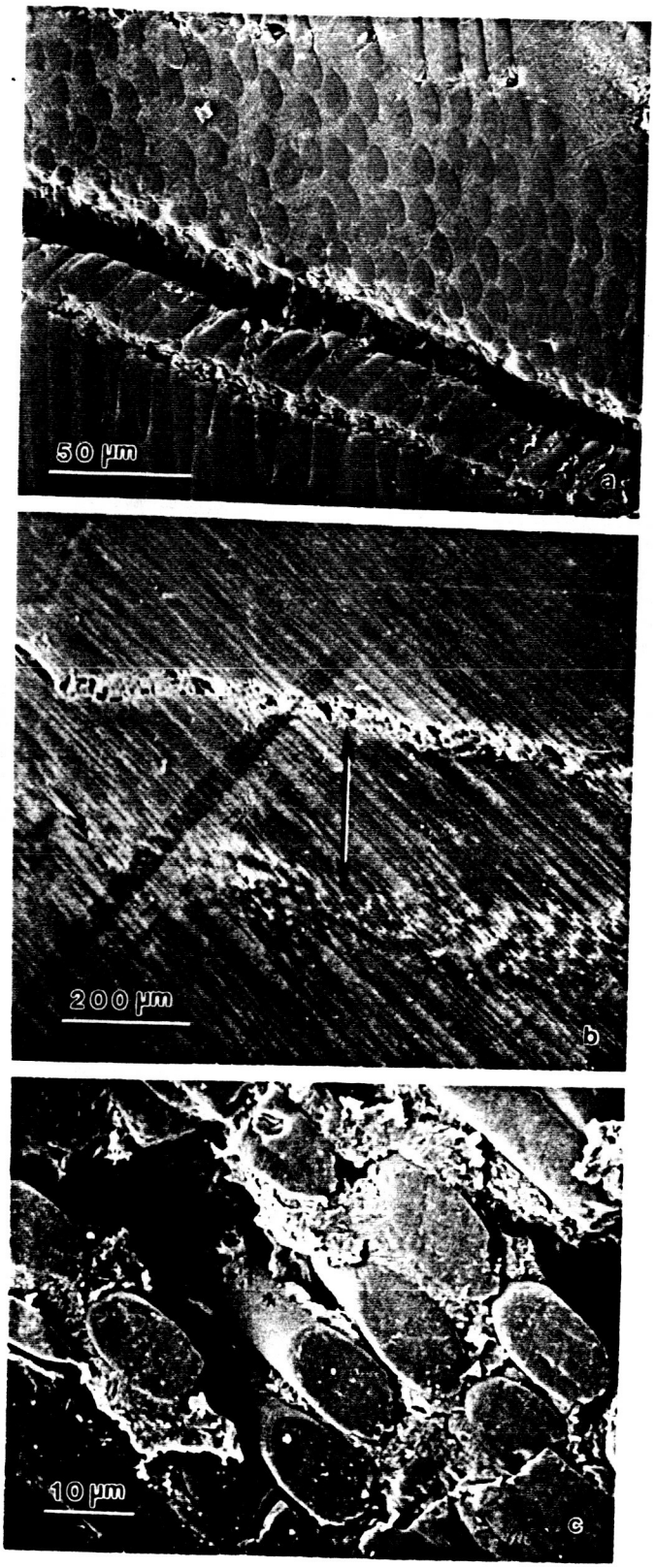

Fig. 63 The shear crippling zone in section 2 ($z_k = 0.25$ mm) of PEEK specimen R is shown in the first group of 0° plies.

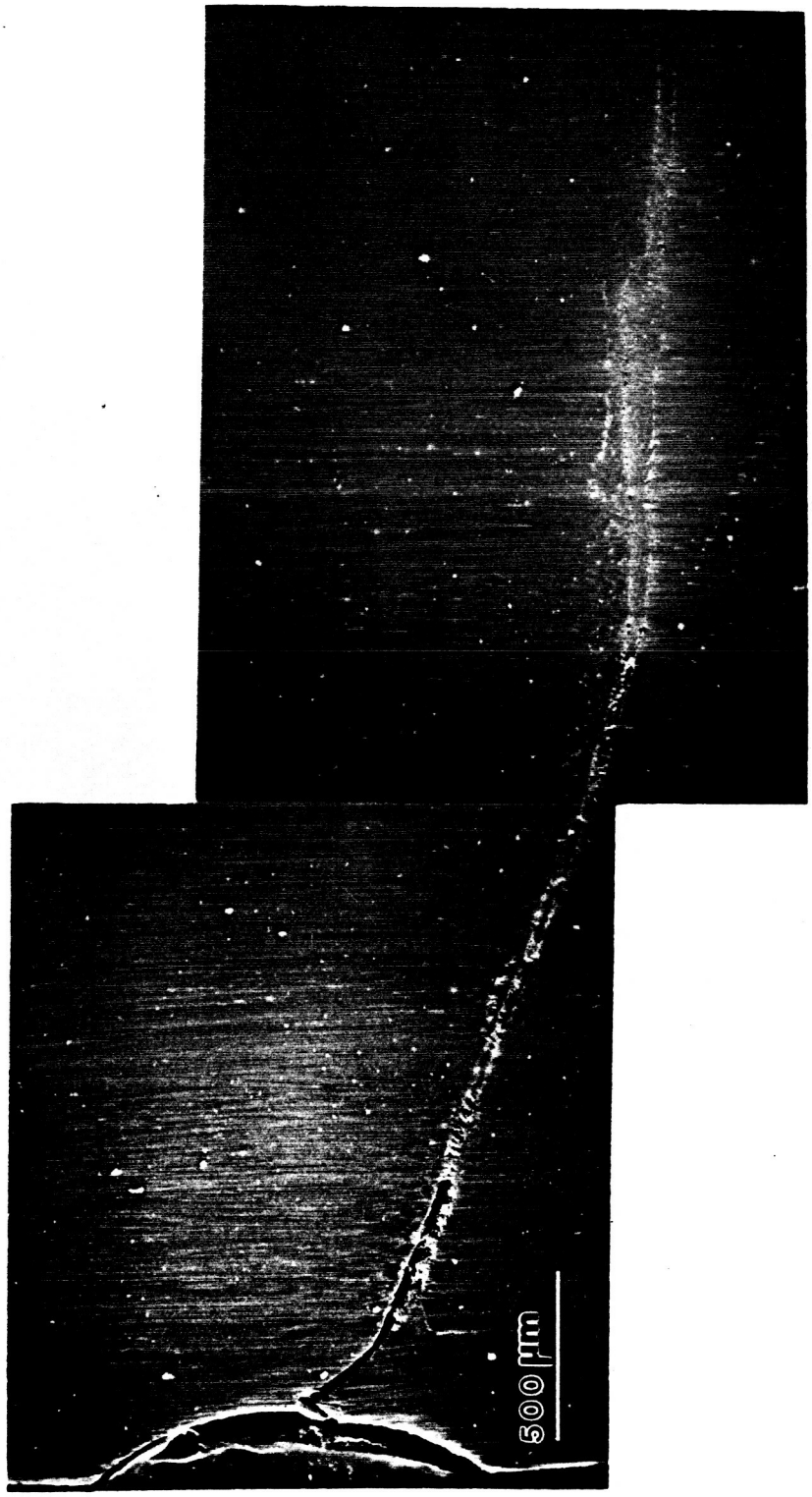

Fig. 64 Details of section 2.
a) Additional kink bands branching off the larger shear crippling zone.
b) Termination of the shear crippling zone in the X-Y plane
with a reduction of broken fibers.

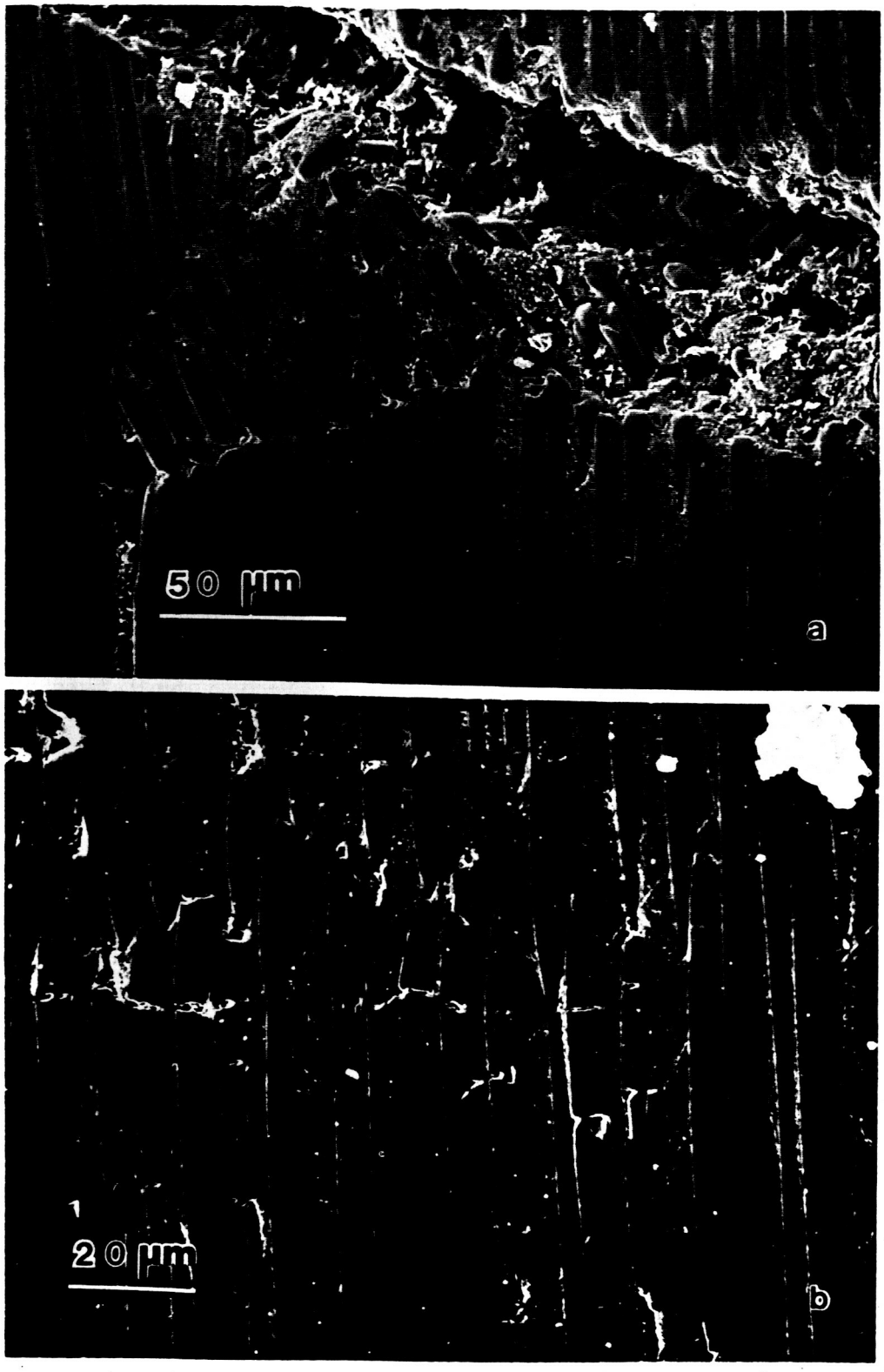

Fig. 65 The shear crippling zone in section 3 (z_k = 0.44 mm) of PEEK specimen *R*.
a) Overview of damage in +45° ply showing damage to be an order of magnitude smaller than that seen in the 0° plies.
b) Local delamination and bending type fiber breaks in the +45° ply.

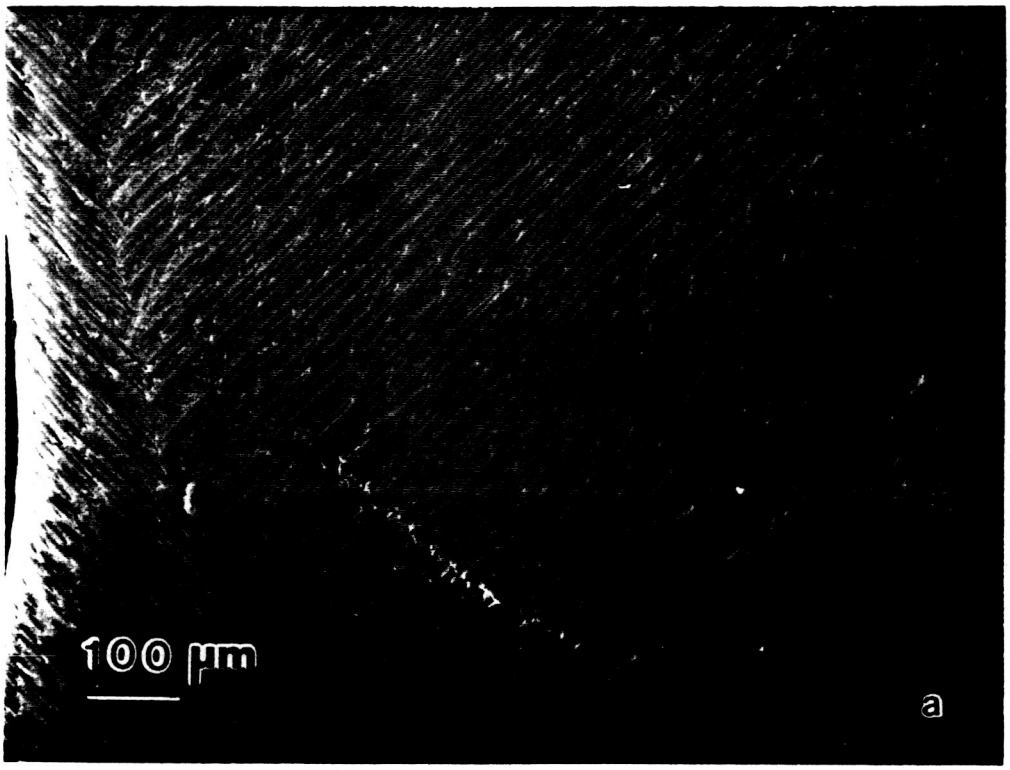

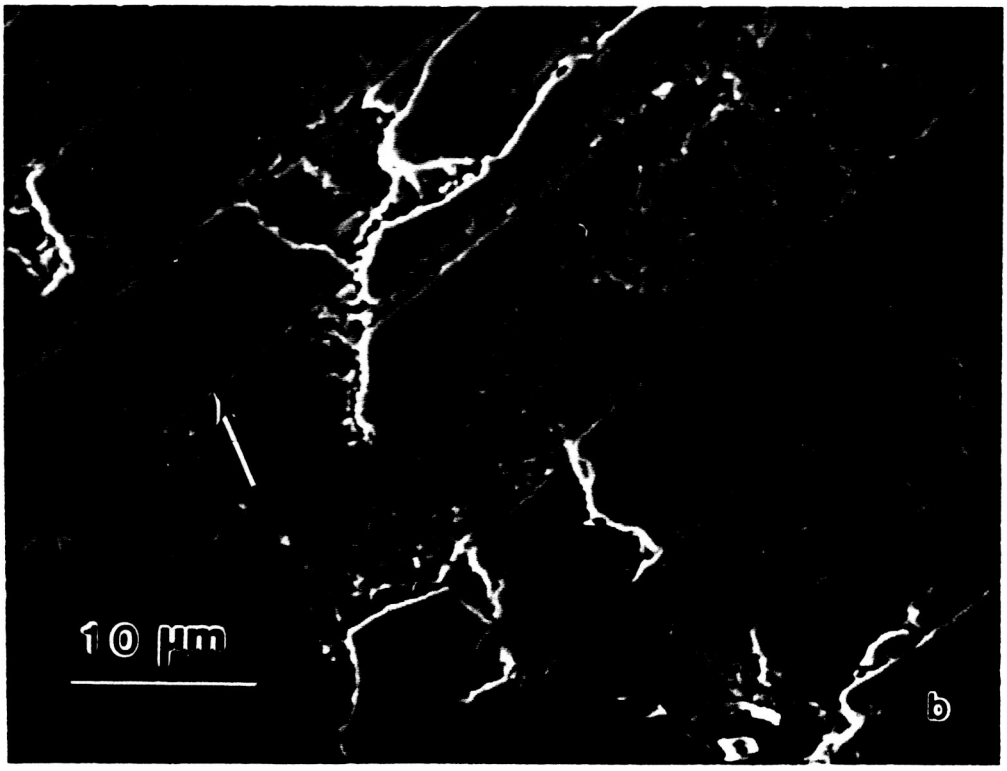

Fig. 66 The shear crippling zone in section 5 ($z_k = 1.09$ mm) of PEEK specimen R.

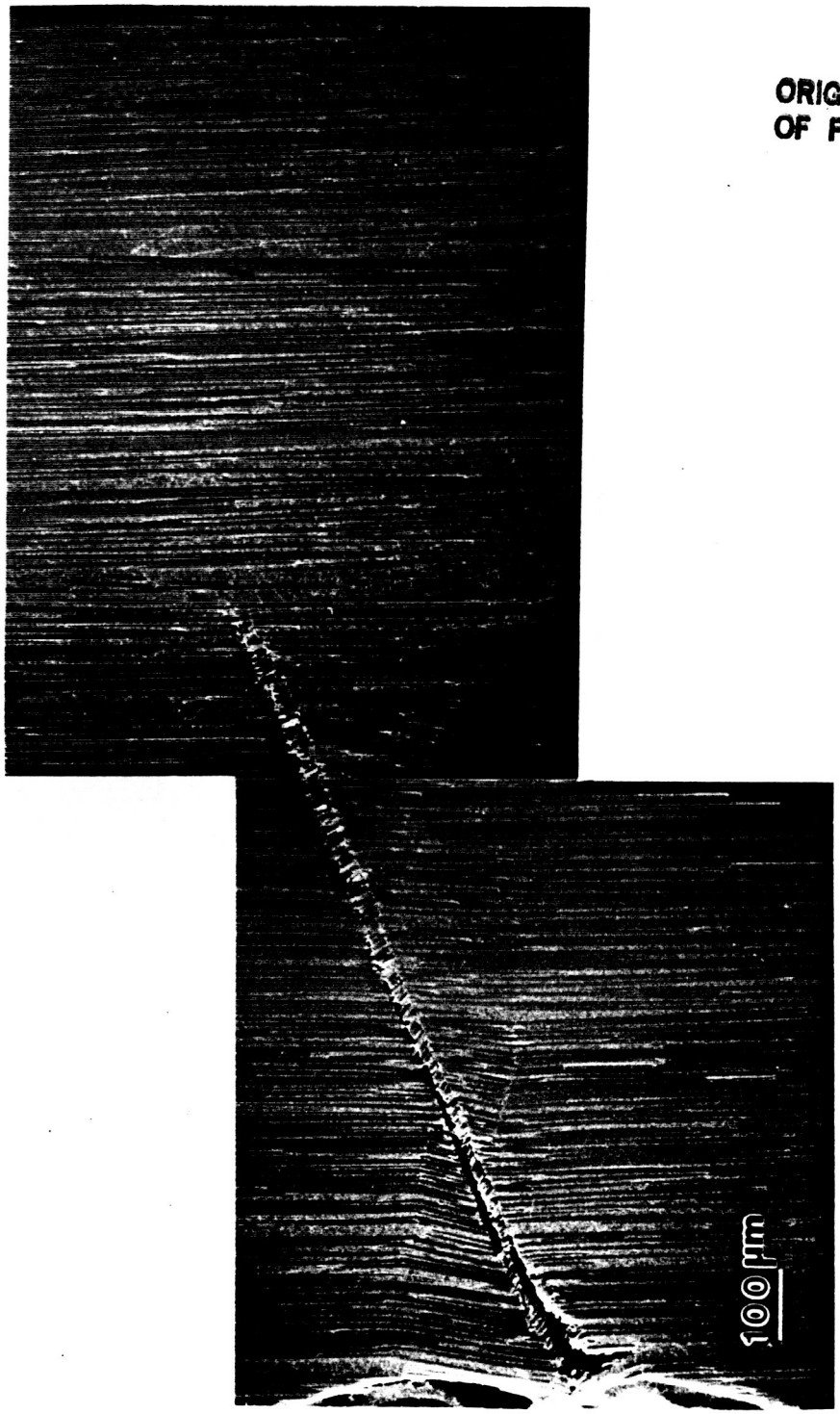

Fig. 67 Details of section 5.
a) Fiber microbuckling in the unsupported hole.
b) Longitudinal splitting within the 0° ply.

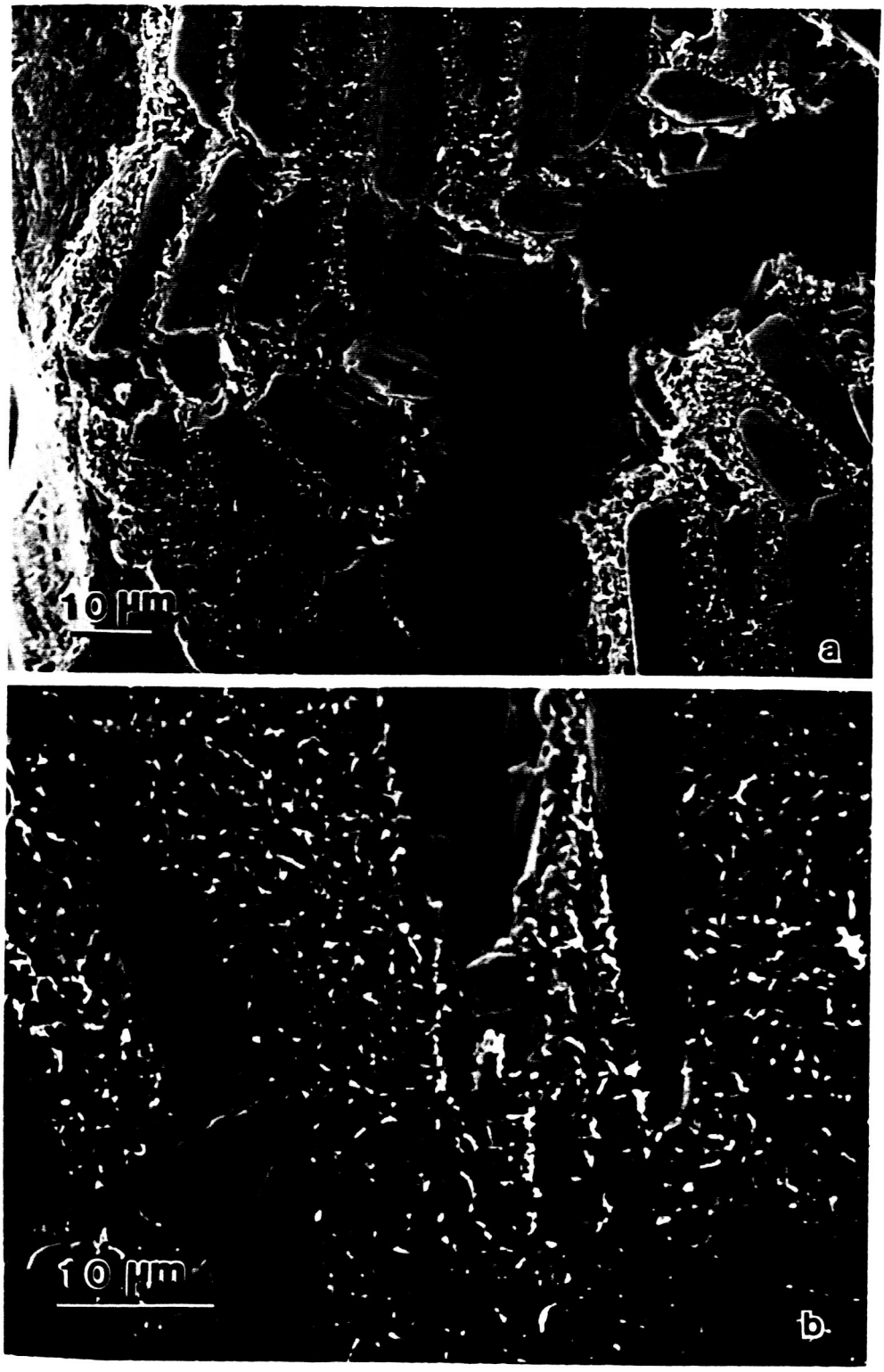

group of 0° plies (see Fig. 66). The shear crippling zone measures 1.1 mm along the X axis at an approximate angle of +30° to the X axis. Again, fiber buckling into the hole (Fig. 67a) appears to initiate the kink band and/or shear crippling zone. Further growth of this zone by in plane fiber microbuckling appears to follow. Lack of surface rigidity allows an accompanying kink band to form at some distance from the initial fiber microbuckling. It is difficult to determine at greater distances from the hole whether the damage is microbuckling or very localized kinking (or shear crippling). In fact, there may not be any distinction for localized kinking. Comparison of section 2 (Fig. 63) with section 5 (Fig. 66) shows the divergent damage pattern previously noted in the Y-Z sections. The clean fracture surfaces of the longitudinal splitting, shown in Fig. 67b, indicate Mode I fracture (no shear deformation). Figure 68 shows the fiber kink bands (indicated by arrows on Fig. 68a) branching from the major shear crippling zone and the deformed matrix (Fig. 68b) connecting them. The termination of the shear crippling zone (reduced fiber breakage and local delaminations) is shown in Fig. 69a along with the bending type break and associated local delaminations in Fig. 69b. The damage observed in section 6, 1.96 mm from the specimen surface, looked very similar to section 5 under the light microscope so this section was not examined in the SEM. No damage was found in section 7 ($z_k = 2.25$ mm), the fifth group of 0° plies, and thus, these section studies were determined to be completed.

IM6/HST-7 Damage Zone

The shear crippling zone in the HST-7 specimen selected for sectioning was shown in Figs. 12b and 33b. Recall that this damage zone was cut from a compression specimen using a precision diamond wire saw, as previously described in Chapter III of this thesis. Additionally, the measured local stress data was

Fig. 68 Details of section 5.
a) Fiber kinking branching from major shear crippling zone.
b) Deformed matrix connecting kink band damage.

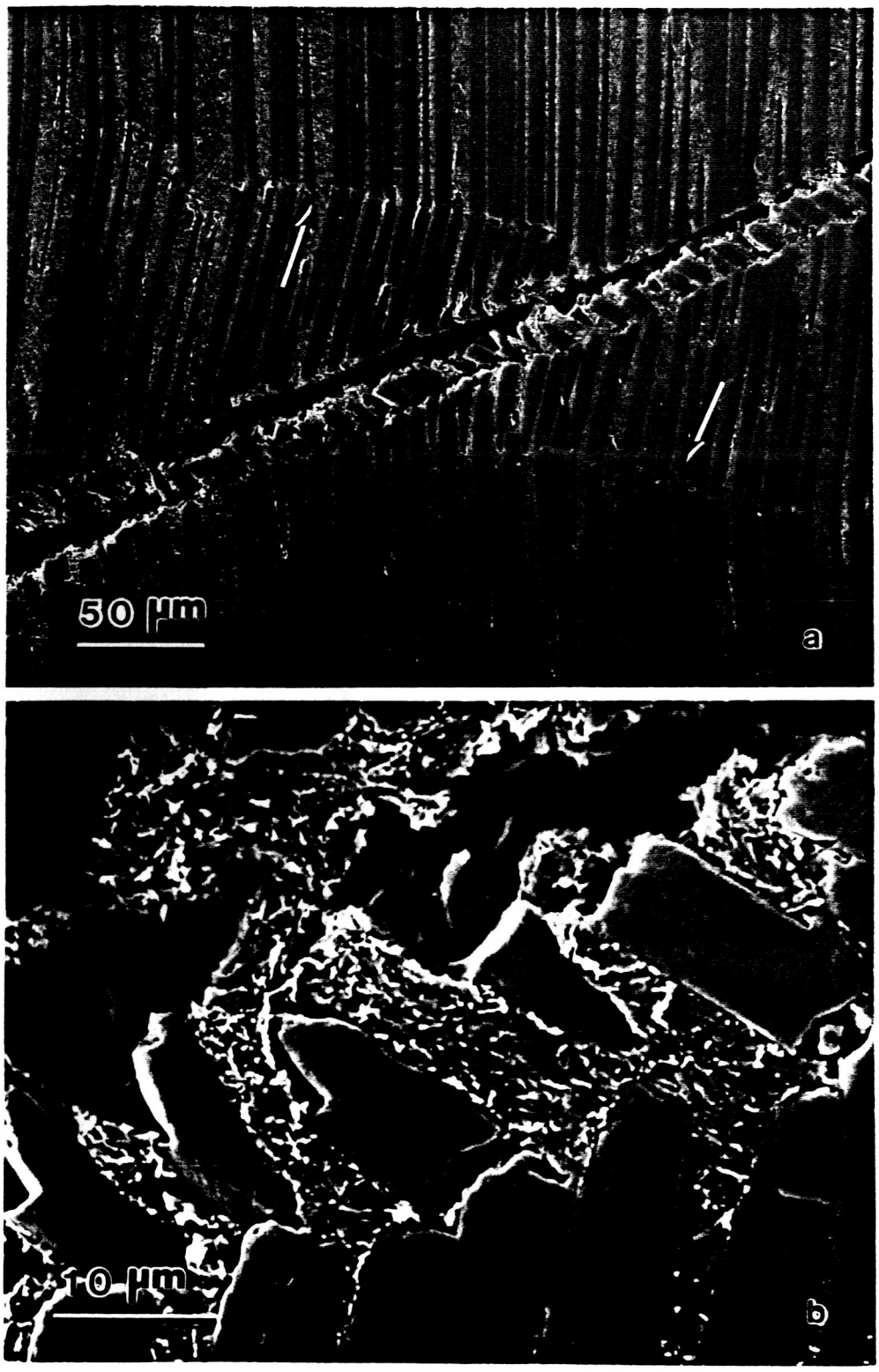

Fig. 69 Details of section 5.
a) Termination of shear crippling zone in X-Y plane.
b) Bending type fiber breaks and local debonds in the shear crippling zone.

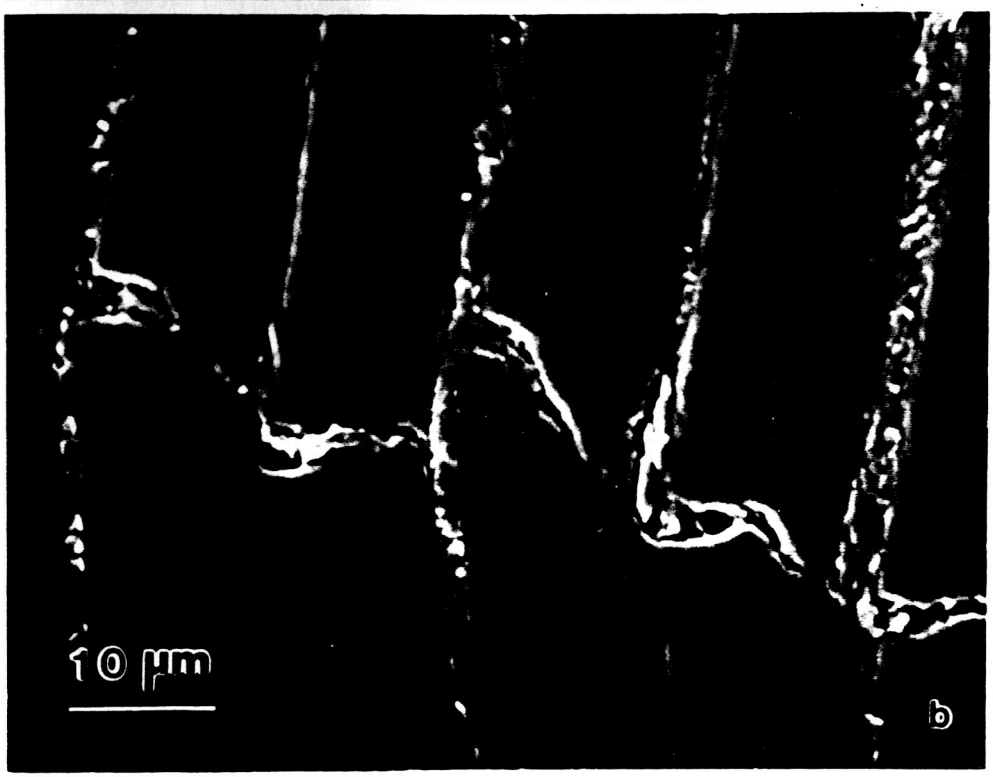

Fig. 70 Shear crippling zone in surface 0° ply in HST-7 specimen.

Fig. 71 Bend type fiber breaks within the shear crippling zone of the sectioned HST-7 specimen.

presented in Figs. 36–39. This damage zone specimen is oriented like specimen R in Fig. 14b, and the shear crippling zone (indicated by arrows) in the surface 0° ply is shown in Fig. 70. The unusual shape of the circumference of the specimen as attributed to the lack of control of the diamond wire saw. In this specimen, the shear crippling zone deviates a maximum of 400 μm from the X axis, along the Y axis. A magnified view of the rotating, kinking, and the bend type breaks in the fibers in the shear crippling zone is shown in Fig. 71. A number of sections through the thickness of this specimen were cut and examined (X-Y plane), but no shear crippling damage was found. The specimen was rotated and the Y-Z plane examined. A very small amount of shear crippling was found in the 16^{th} and 17^{th} 0° plies. Examining the X-Y plane, this damage was located at an angle of +30° above the X axis, and it continued to the top edge of the specimen. No micrographs of this damage are included.

CHAPTER V

DISCUSSION

From the results presented in Figs. 29 and 30, it is obvious that the Dugdale model does not accurately predict the load-damage size relationship of open hole composite specimens loaded in compression. Possible reasons that this model does not describe the observed behavior are as follows:

1. The constitutive relationship used in the Dugdale model is not an accurate description of material response in the crush zone;
2. The crush zone size is measured on the surface of the specimen, but based on the NDE and SEM observations, this size is not an accurate indication of the actual crush zone size through the laminate.

Although a Dugdale type model was chosen for open hole composite laminates loaded in compression because of apparent damage similarities, the sectioning studies have revealed many differences in the damage and its propagation. Tension cracks (plane stress or plane strain conditions) in metals primarily form symmetric through the thickness of the material and then propagate uniformly. Consequently, the visible surface crack is representative of the actual damage through the thickness of the material. Because of the inhomogeneity of composite laminates, the compressive crush zone initiates in the weaker part (includes both the weaker edge of the hole and the weaker surface of the specimen) of the laminate. Once the damage zone has formed, that particular portion of the specimen is further weakened, leading to a reduction in stability (and lowered stiffness) for that part of the laminate. The measured crush zone size is not an accurate measurement of the damage through the thickness of the laminate. Unfortunately, only visible surface damage may be measured during the test. Furthermore, the choice of plane stress ($\alpha = 1$) or plane

strain ($\alpha = 3$) conditions in eq. (13) does not alter the shape of the S-ρ relationship. However, it should be recalled from Figs. 29 and 30 that the observed shape of the S-ρ relationship is much flatter that the predicted relationships, independent of the chosen crush zone stress, σ_{oc}. Thus, the model's inaccuracies cannot be explained by inaccuracies in the crush zone size determination from real-time measurements at the surface. The constitutive relationship assumed must be incorrect.

The Dugdale type analysis used by Newman[29] assumes an elastic-perfectly plastic constitutive relationship for the material, as shown in Fig. 72a. However, the local stress-applied stress data presented in Figs. 34–39 indicate that once the shear crippling zone forms, the load previously carried by the same undamaged material is now significantly reduced. Meanwhile, the local load supported in other remote locations in undamaged material increases. A more realistic constitutive relationship for this trend is shown for comparison in Fig. 72b along with a schematic of the microscopic fracture processes in Fig 72c. This relationship assumes that fiber buckling (steps 1–3 of Fig. 72c) reduces the load bearing capacity of the material in the crush zone, giving load redistribution to material adjacent to this zone. Once the crush zone has grown across the width of the specimen, then the load on the crush zone again increases because there is no longer adjacent material of greater stiffness to which the load can be redistributed. The increased load on the crush zone will lead to steps 4 and 5 in Fig. 72c and the increasing stiffness in the crush zone which allows for the observed increase in loading. This larger load on the crush zone will usually lead to immediate propagation of local delaminations which initiated during the crush zone formation. A catastrophic "broomed" type specimen failure specimen is the result.

It is clear that the constitutive relationship given in Fig. 72a would allow a

Fig. 72 Constitutive relationships.
a) Dugdale type elastic-perfectly plastic model.
b) Suggested model for crush zone in compression loaded composite laminates.
c) A schematic of the microscopic processes within the shear crippling zone.

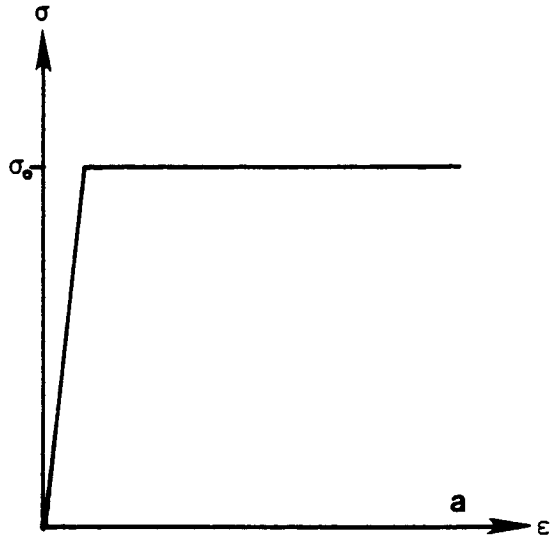
σ
σ_o
a
ε

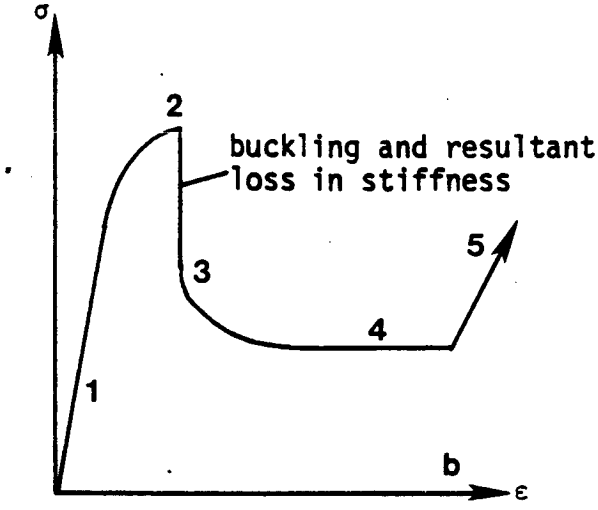
σ
2
buckling and resultant
loss in stiffness
5
3
4
1
b
ε

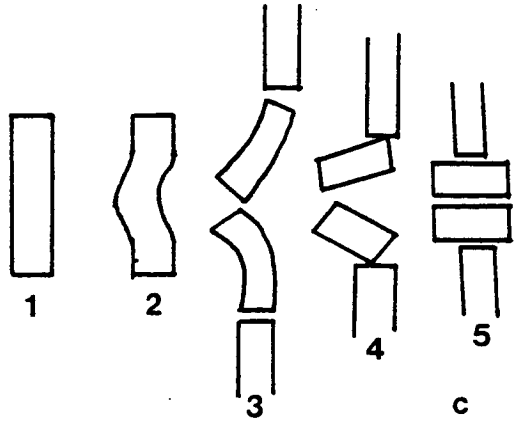
1
2
3
4
5
c

monotonic increase in load with crush zone size, the crush zone being assumed to support a stress of σ_{oc}, where $\sigma_{oc} > \sigma(x-r)$ throughout the width of the specimen, as seen in Fig. 73a. However, the constitutive relationship shown in Fig. 72b would lead to a stress distribution similar to that shown in Fig. 73b, which does not necessarily allow the load (proportional to the integrated area under the σ vs. $x - r$ curve) to monotonically increase with increasing crush zone size. Recently published results by Aronsson and Bäcklund[26,27] physically invoke assumptions more consistent with these observations rather than those implicit in Newman's analysis.

The results of thesis sectioning investigations (Figs. 40–71) show that the majority of the damage in compression loaded, open hole composite laminates is shear crippled or microbuckled 0° fibers. However, in many cases (shown in Figs. 45, 49, 50a, 51, 52, 55, and 56a), the shear crippling damage within the 0° plies produces shear strains and damage in the adjacent off-axis plies. The damage appears to be initiated by fiber microbuckling in a direction where transverse stiffness is minimal, i.e., into the hole (Figs. 40, 41, 61, 63, 66, 67a) or toward the closer unsupported specimen surface (Figs. 45, 49, 50a, 51, 53, 55, and 70). Because of the support of numerous undamaged adjacent plies, the 0° plies near the center of the laminate generally do not microbuckle and/or shear cripple out of the plane (Y-Z plane). However, as observed in the preliminary sectioning investigation, the interior 0° plies may buckle into the unsupported hole edge through the thickness of the laminate. The fiber microbuckling is followed by the formation of a kink band or shear crippling zone. The fiber kinking and rotating was observed in the shear crippling zone in both the X-Y and Y-Z planes in almost every micrograph, supporting the idea of initiation by fiber microbuckling toward an unsupported

Fig. 73 Stress distribution across remaining ligament width.
a) Dugdale type analysis.
b) Crush zone in compression loaded composite laminates.

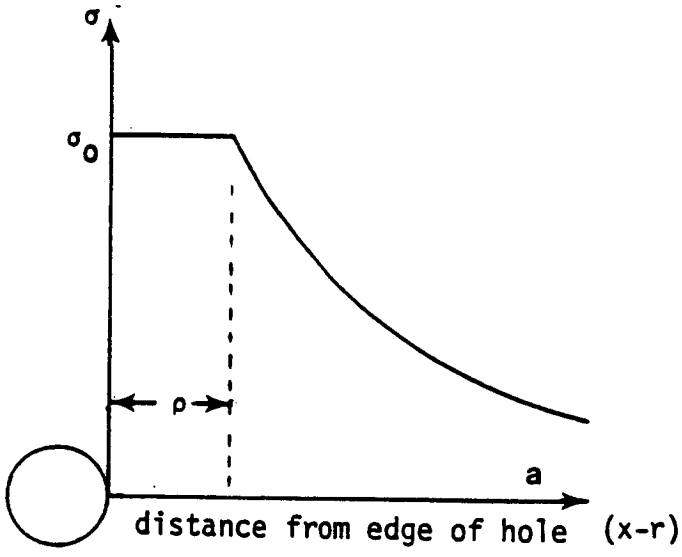
σ
σ0
ρ
a
distance from edge of hole (x-r)

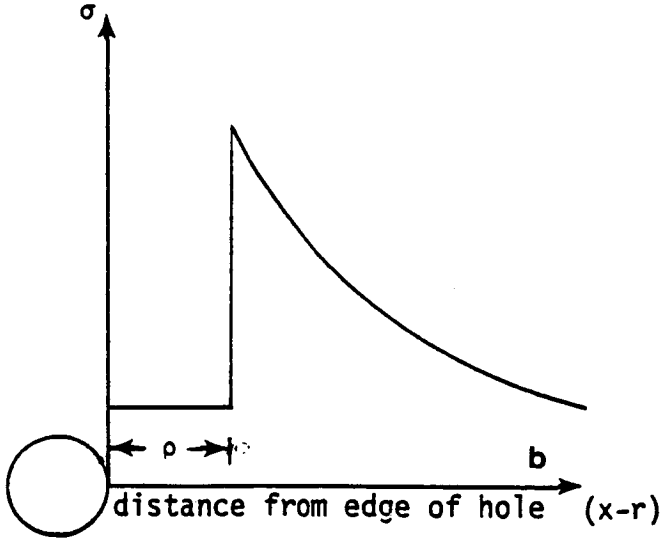
σ
ρ
b
distance from edge of hole (x-r)

surface. The damage zone in the HST-7 specimen (Fig. 70) containing 0° fibers in the surface plies consisted primarily of fiber microbuckling of unsupported surface fibers.

To clarify, the various types of damage observed in these compression failures prior to final failure are summarized. The types of damage are noted schematically in Fig. 74 and include (1) symmetric microbuckling, shown in Fig. 74a, (2) asymetric microbuckling, shown in Fig. 74b, and shear crippling, shown in Fig. 74c. It is not apparent that these three distinct types of damage involve completely different mechanisms. In fact, it may be that the same mechanism can give these three results when the transverse support conditions are varied. The term microbuckle is used to refer to a kinked fiber where fiber alignment in the kinked direction is retained, as shown in Figs 74a and 74b. Shear crippling refers to kinking where an offset in fiber alignment is observed.

In plane (X-Y) damage was typically characterized by a relatively local, symmetric microbuckle into the hole which subsequently propagated away from the hole at an angle of about 20° from the horizontal axis. This in-plane microbuckling appears to make the composite more susceptible to subsequent out of plane shear crippling, as previously seen in Figs. 42–57, possibly by providing a plane on which shear deformation can occur more easily.

As noted earlier, very local deformation and/or delamination must accompany the fiber microbuckling or shear crippling to accommodate the large interlaminar rotations and displacements that occur locally. However, according to the NDE (Figs. 32 and 33) these microscopic local delaminations apparently do not propagate (to become macroscopic delaminations) until final compressive failure when large scale brooming and/or delamination occurs. Furthermore, in the Y-Z sections of

Fig. 74 Fiber damage observed prior to final failure in these compression tests.
a) Symmetric microbuckling.
b) Asymmetric microbuckling.
c) Shear cripplilng.

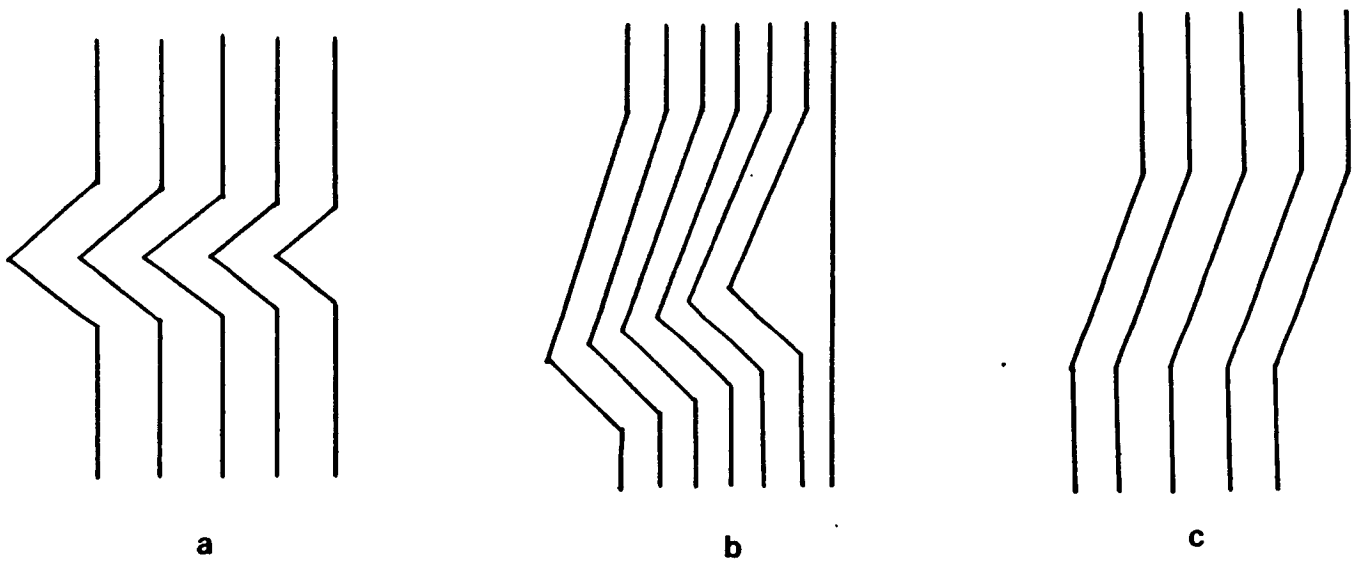
a
b
c

the PEEK system, the observation that the local ply delaminations were smaller in size and eventually disappeared with increasing distance from the hole may be understood with reference to Fig. 72c. As the sections examined get farther from the hole into the composite, the rotation and the shear deformation required to accommodate this in plane microbuckling decreases, step 3 in Fig. 72c. Step 3 represents the region adjacent to the hole and step 1 represents the region far from the hole. If the resin is sufficiently ductile, it is possible that no local delamination occurs until steps 4 and 5 (Fig. 72c) are observed, probably after the crush zone has propagated across the width of the specimen. Figures 49–53 shows an example of considerable deformation and even fiber rotation in the adjacent off-axis ply where the resin is capable of such shear deformation. Delamination is postponed if not avoided altogether, even on the local scale. The rotating and kinking within the shear crippling zone was also shown to initiate longitudinal splitting within the 0° plies (Figs. 63, 64, 66, and 67), additional branches of shear crippling from the major shear crippling zone (Figs. 63, 665, and 68a), and ply delaminations between adjacent plies where the 0° shear crippling zone extended into these plies (Figs. 49, 51, 52, and 54).

Superposition of the damage observed at each section through the shear crippling zone yields a three-dimensional schematic of the damage, as shown in Fig. 75. Although the shear crippling zones within the 0° plies form planes, the angle of these planes with respect to the X axis and the resin ductility governs the amount of connecting damage in the adjacent plies.

Once the crush zone has propagated across the specimen, the load on the crush zone and the adjacent off-angle plies increases dramatically, giving either a delamination induced brooming failure or coalescence of damage in adjacent groups

Fig. 75 Three-dimensional schematic drawing of the shear crippling zone.

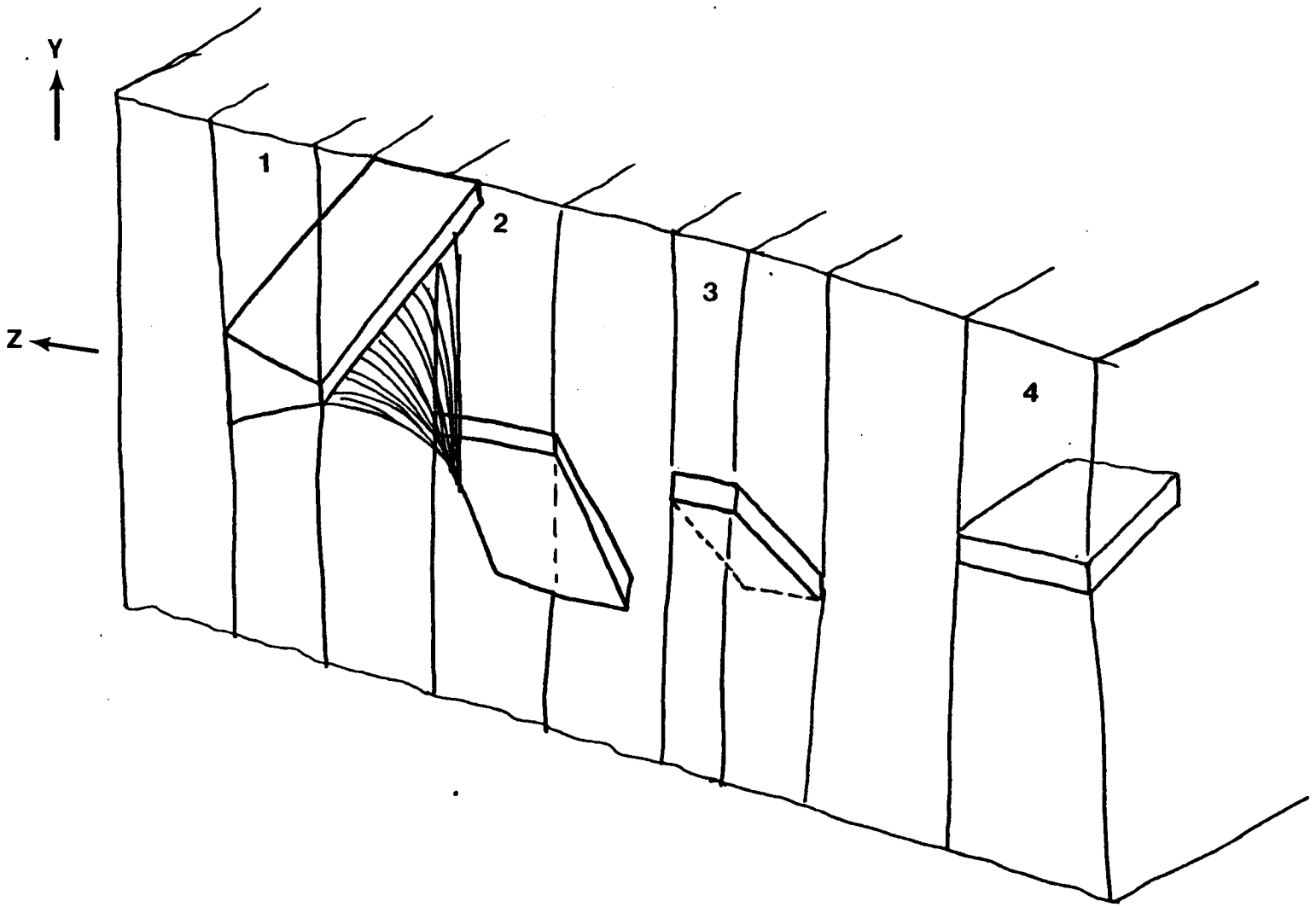
Y
Z
1
2
3
4

of 0° plies through the off-angle plies, as seen in Fig. .

If a more brittle resin is used, the resin will give much more support to the fibers to resist microbuckling. However, even a small amount of local buckling cannot be accommodated with resin deformation, and thus, delamination occurs immediately. Furthermore, the resistance to propagation of such local delaminations is small, allowing a brooming type failure to occur with little damage (crush) zone formation. Thus, compressive failure may be thought of as initiation controlled in composites made of brittle resins and propagation controlled in composites made of ductile resins.

In a composite with a hole, a brittle resin will give a full notch sensitivity as failure is controlled by initiation at the hole where the stress concentration is maximum. For an open hole composite made from a more ductile resin, propagation of the damage away from the hole prior to catastrophic failure may allow final failure to be precipitated at a distance from the hole where the effect of the stress concentration is reduced somewhat, giving a lower notch sensitivity. The results of Starnes et al[9] are consistent with this hypothesis.

CHAPTER VI

CONCLUSIONS AND RECOMMENDATIONS

Conclusions

The following conclusions may be drawn from this work.

1. Growth of a stable crush zone resulting from microbuckling of 0° fibers precedes compressive failure in tough matrix composite laminates with holes.
2. The assumption of an elastic-perfectly plastic constitutive relationship for material in the crush zone does not accurately predict the load-crush zone size relationship. Such a relationship also indicates a greater amount of stable crush zone growth than is observed in practice.
3. Experimental measurements indicate a more realistic model would include a reduction in the load supported by the crush zone compared to the adjacent region where fiber microbuckling has not yet occurred.
4. The crush or damage zone is initiated by fiber microbuckling toward an unsupported surface, either into the hole or toward the closer specimen surface in plies near a free surface.
5. In and out of plane fiber microbuckling appears to preceed shear crippling damage in the systems used in this study.
6. Local delaminations accompany the fiber microbuckling and shear crippling to accommodate the large interlaminar shear strains that occur locally.
7. Local delaminations apparently do not propagate (to become macroscopic delaminations) until final compressive failure when large scale brooming and/or delamination occurs.

Recommendations for Future Work

Based on the conclusions from this work, the following recommendations for future work are suggested.

1. Conduct similar compression tests but replace the center holes with edge notches (semi-circular or elliptical) to observe the nucleation of compression failure in the notch root.
2. Apply geometric moiré to provide a more accurate description of the strain field at the hole, both before and after the shear crippling zone is present. This technique may also be applied to the edge notch specimen previously mentioned.
3. Conduct in-situ four-point bend tests in the SEM to further verify fiber microbuckling as the initiation of fiber kinking and thus, the shear crippling zones.
4. Conduct compact tension-like tests (use compression loading) in the SEM to observe the failure process on the specimen surface adjacent to the notch as well as in the notch itself.

SELECTED REFERENCES

[1] Dow, N.F. and Gruntfest, I.J., "Determination of Most Needed Potentially Possible Improvements in Materials for Ballistic and Space Vehicles," General Electric, TIS 60SD389, June 1960.

[2] Rosen, B.W., "Mechanics of Composite Strengthening," Fiber Composite Materials, American Society for Metals Seminar, 1965, pp. 58–65.

[3] Hayashi,T., "Compressive Strength of Unidirectionally Fiber Reinforced Composite Materials," 7^{th} *International Reinforced Plastics Conference*, British Plastics Federation, Brighton, vol. 11, pp. 1970.

[4] Greszcuk, L.B., "Unknown," *AIAA Journal*, vol. 13, 1967, pp. 1131–1138.

[5] Ewins, P.D. and Ham, A.C., "Unknown," *AIAA/ASME/SAE* 15^{th} *Structures, Structural Dynamics, and Materials Conference*, Las Vegas, Nevada, 1974.

[6] Ewins, P.D. and Potter, R.T., "Some Observations on the Nature of Fiber Reinforced Plastics and the Implications for Structural Design," *Philosophical Transactions of the Royal Society of London*, vol. A294, 1980, pp. 507–517.

[7] Byers,B.A., "Behavior of Damaged Graphite/Epoxy Laminates Under Compression Loading," NASA Langley Research Center, NASA Contractor Report 159293, August 1980.

[8] Rhodes, M.D., Mikulas, M.M., and M^{c}Gowan, P.E., "Effects of Orthotropy and Width on the Compression Strengths of Graphite/Epoxy Panels with Holes," *AIAA Journal*, vol. 22, September 1984, pp. 1283–1292.

[9] Starnes, J.H. and Williams, J.G., "Failure Characteristics of Graphite/Epoxy Structural Components Loaded in Compression," in *Mechanics of Composite Materials—Recent Advances*. Z. Hashin and C.T. Herakovich, ED. Pergamon Press, 1982, pp. 283–306.

[10] Starnes, J.H., Rhodes, M.D., and Williams, J.G., "Effect of Impact Damage and Holes on the Compressive Strength of a Graphite/Epoxy Laminate," *ASTM STP 696*, 1979, pp. 145–171.

[11] Williams J.G., "Effect of Impact Damage and Open Holes on the Compression Strength of Tough Resin/High Strain Fiber Laminates," NASA Langley Research Center, NASA Technical Memorandum 85756, February 1984.

[12] Mikulas, M.M., "Failure Prediction Techniques for Compression Loaded Composite Laminates with Holes," NASA Langley Research Center, NASA CP 2142, 1982.

[13] Hahn, H.T. and Williams, J.G., "Compression Failure Mechanisms in Unidirectional Composites," NASA Langley Research Center, NASA Technical Memorandum 85834, August 1984.

[14] Waas, A. and Babcock, C., "Observation of the Initiation and Progression of Damage in Compressively Loaded Composite Plates Containing a Cutout," NASA Langley Research Center, NASA Progress Report for Grant #NSG1483, November 1986.

[15] Potter, R.T. and Purslow, D., "The Environmental Degradation of Notched CFRP in Compression," *Composites*, July 1983, pp. 206–225.

[16] Malik, B., Palazotto, A., and Whitney, J., "Notch Strength of GR/PEEK Composite Material at Elevated Temperatures," 26^{th} *Structures, Structural Dynamics, and Materials Conference*, Orlando, Florida, April 1985.

[17] Waddoups, M.E., Eisenmann, J.R., and Kaminski, B.E., "Macroscopic Fracture Mechanics of Advanced Composite Materials," *J. Composite Materials*, vol. 5, October 1971, pp. 446–454.

[18] Kanninen, M.F., Rybicke, E.F., and Brinson, H.F., "A Critical Look at Current Applications of Fracture Mechanics to the Failure of Fiber Reinforced Composites," *Composites*, January 1977, pp. 17–22.

[19] Mar, J.W. and Lin, K.Y., "Fracture Mechanics Correlation for Tensile Failure of Filamentary Composites with Holes," *J. Aircraft*, vol. 14, No. 7, July 1977, pp. 703–704.

[20] Caprino, G., Halpin, J.C., and Nicolais, L., "Fracture Mechanics in Composite Materials," *Composites*, October 1979, pp. 223–227.

[21] Pipes, R.B., Wetherhold, R.C., and Gillespie, J.W., "Macroscopic Fracture of Fibrous Composites," *Materials Science and Engineering*, vol. 45, 1980, pp. 247–253.

[22] Bathias, C., Esnault, R., and Pellas, J., "Application of Fracture Mechanics to Graphite Fiber Reinforced Composites," *Composites*, July 1981, pp. 195–200.

[23] Whitney, J.M. and Nuismer, R.J., "Stress Fracture Criteria for Laminated Composites Containing Stress Concentrations," *J. Composite Materials*, vol. 8, July 1974, pp. 253–265.

[24] Nuismer, R.J. and Whitney, J.M., "Uniaxial Failure of Composite Laminates Containing Stress Concentrations," *Fracture Mechanics of Composites—ASTM STP 593*, 1975, pp. 117–142

[25] Nuismer, R.J. and Labor, J.D., "Applications of the Average Stress Criterion: Part II—Compression," *J. Composite Materials*, vol. 13, January 1979, pp. 49–60.

[26] Aronsson, C.G. and Bäcklund, J., "Tensile Fracture of Laminates with Cracks," *J. Composite Materials*, vol. 20, May 1986, pp. 287–307.

[27] Aronsson, C.G. and Bäcklund, J., "Tensile Fracture of Laminates with Holes," *J. Composite Materials*, vol. 20, May 1986, pp. 259–286.

[28] Barenblatt, G.I., "The Mathematical Theory of Equilibrium Cracks in Brittle Fracture," *Advance in Applied Mechanics*, vol. 7, 1960, pp. 55–129.

[29] Newman, J.C., Jr., "A Nonlinear Fracture Mechanics Approach to the Growth of Small Cracks," *Behavior of Short Cracks on Airframe Components, AGARD Conference Proceedings*, France, 1982.

[30] Broek, D., *Elementary Engineering Fracture Mechanics*, 3rd Edition, Martinus Nijhoff Publishers, Boston, MA, 1982, pp. 91–96.

[31] Bradley, W.L., Micromechanics of Fatigue and Fracture of Alloys, graduate course at Texas A&M University, College Station, Texas, 1986.

[32] Hartness, J.T., "Polyether Matrix Composites," *SAMPE Quarterly*, January 1983, pp. 33–36.

[33] Celanese Corp., "Material Properties, CELION 12000 Carbon Fibers," trade name material description, 1983.

[34] Moulton, R., private communications, June 1987.

[35] Hexcel Corp., "F155 Resin Systems for Advanced Composites," trade name material description, March 1985.

[36] American Cyanamid Co., Engineering Materials Department, "CYCOM HST-7 Tough Advanced Composites, a 350° Cure High Toughness Epoxy Laminating Material," trade name material description, 1986.

[37] Johnston, N., private communications, April 1987.

[38] Chan, W., private communications, June 1987.

[39] Knoish, H.J. and Whitney, J.M., "Approximate Stresses in an Orthotropic Plate Containing a Circular Hole," *J. Composite Materials*, vol. 9, April 1975, pp. 157–166.

[40] Bogetti, T.A., Gillespie, J.W., Jr., and Pipes, R.B., "Evaluation of the IITRI Compression Test Method for Stiffness and Strength Determinination," Center for Composite Materials, University of Delaware, CCM-87-09, March 1987.

[41] Keary, P.E., Ilcewicz, L.B., Shaar, C., and Trostle, J., "Interlaminar Fracture Toughness of Composites Using Slender Double Cantilever Beam Specimens," *J. Composite Materials*, vol. 19, March 1985, pp. 154–175.

[42] Hibbs, M.F., "Microscopic Delamination Processes and Resulting Crack Tip Strain Fields of Graphite/Epoxy Composites," Department of Mechanical Engineering, Texas A&M University, Ph.D. Dissertation, December 1987.

[43] Masters, J.E., "Correlation of Impact and Delamination Resistance in Interleafed Laminates," 6th *International Conference in Composite Materials combined with the* 2nd *European Conference on Composite Materials*, ICCM & ECCM, Imperial College of Science and Technology, London, United Kingdom, July 1987, vol. 3, pp. 96–107.

APPENDIX A

PROGRAM FOR DUGDALE TYPE ANALYSIS

```
10     ! DUGDALE MODEL applied to composites in compression loading.
20     !
30     OPTION BASE 1
31   !  PLOTTER IS 13,"GRAPHICS"
32     PLOTTER IS 7,5,"9872A"
33     PENUP
34     SCALE 0,.50,0,100000
36     AXES .01,10000,0,0
40   !  PRINTER IS 0
50     IMAGE 3X,"SMAX,",2X,"ALPHA",2X,"HOLE RADIUS,",2X,"HALF WIDTH,",2X,"CRACK L
ENGTH,",3X,"RHO,",5X,"SIG0,"
60     !
70     IMAGE 4X,"PSI",15X,"IN",11X,"IN",12X,"IN",10X,"IN",6X,"PSI"
80     !
90     IMAGE 6D,6X,D,6X,D.DDDD,9X,D.DD,9X,D.DDDD,5X,D.DDDD,4X,6D
100    !
110  ! PRINT USING 50
120  ! PRINT USING 70
130    INPUT "Sig0, Alpha, R, W, C, Symmetric (Y or N)",Sig0,Alpha,R,W,C,N$
140    FOR Sig0=10000 TO 100000 STEP 10000
145    PENUP
150    FOR Rho=.001 TO .50 STEP .001
160    GRAPHICS
170    RAD
180    !
190    D=Rho+C
200    !
210    B1=C
220    B2=D
230    Lambda=R/D
240    !
250    F1=.707+.765*Lambda+.282*Lambda^2+.74*Lambda^3+.872*Lambda^4
260    !
270    F2=1+.358*Lambda+1.425*Lambda^2-1.578*Lambda^3+2.156*Lambda^4
280    !
290    IF N$="Y" THEN GOTO 350
300    !
310    Fn=F1
320    !
330    GOTO 50
340    !
350    Fn=F2
360    !
370    Fhs=Fn*SQR(1-Lambda)
380    !
390    Fws=SQR(1/COS(PI*R/2/W)/COS(PI*D/2/W))
400    !
410    A1=-.02*Lambda^2+.558*Lambda^4
420    !
430    A2=.221*Lambda^2+.046*Lambda^4
440    !
450    Gamma1=B1/D
460    !
```

```
470   Gamma2=B2/D
480   !
490   Con1=1+A1/(1-Lambda)+3*A2/2/(1-Lambda)^2
500   !
510   Con2=A1/(1-Lambda)+(4-Gamma2)*A2/2/(1-Lambda)^2
520   !
530   Con22=A1/(1-Lambda)+(4-Gamma1)*A2/2/(1-Lambda)^2
540   !
550   G=Con1*(ASN(Gamma2)-ASN(Gamma1))+Con2*SQR(1-Gamma2^2)-Con22*SQR(1-Gamma1^2
)
560   !
570   Fhsig=G/(ASN(Gamma2)-ASN(Gamma1))
580   !
590   Con3=PI*D/2/W
600   !
610   Bk1=SIN(PI*B1/2/W)/SIN(Con3)
620   !
630   Bk2=SIN(PI*B2/2/W)/SIN(Con3)
640   !
650   Con4=SQR(1/COS(Con3))
660   !
670   Fwsig=(ASN(Bk2)-ASN(Bk1))/(ASN(Gamma2)-ASN(Gamma1))*Con4
680   !
690   Smax=Sig0*Alpha*Fhsig*Fwsig*(1-2/PI*ASN(C/D))/Fhs/Fws
700   !
710 ! PRINT LIN(1)
720   !
721   PLOT Rho,Smax
730 ! PRINT USING 90;Smax,Alpha,R,W,C,Rho,Sig0
740   NEXT Rho
741   NEXT Sig0
750   GOTO 130
760   END
```